UNIVERSIDADE FEDERAL DE MINAS GERAIS
PROGRAMA DE PÓS-GRADUAÇÃO EM FÍSICA

GILBERTO RODRIGUES DA SILVA JUNIOR

Interplay of crystalline strain and electronic properties in topological insulators and semiconductor thin films grown by Molecular Beam Epitaxy

BELO HORIZONTE

2022

Gilberto Rodrigues da Silva Junior

Interplay of crystalline strain and electronic properties in topological insulators and semiconductor thin films grown by Molecular Beam Epitaxy

Thesis submitted to Universidade Federal de Minas Gerais as a partial requirement for obtaining the Ph.D. degree in Physics.

Adviser: Ângelo Malachias de Souza

Belo Horizonte
2022

Dados Internacionais de Catalogação na Publicação (CIP)

S586i Silva Junior, Gilberto Rodrigues da.
Interplay of crystalline strain and electronic properties in topological insulators and semiconductor thin films grown by Molecular Beam Epitaxy / Gilberto Rodrigues da Silva Junior. – 2022.
161f., enc. : il.

Orientador: Ângelo Malachias de Souza.
Tese (doutorado) – Universidade Federal de Minas Gerais, Departamento de Física.
Bibliografia: f. 146-161.

1. Raios X - Difração. 2. Epitaxia por feixe molecular. 3. Semicondutores. I. Título. II. Souza, Ângelo Malachias de. III. Universidade Federal de Minas Gerais, Departamento de Física.

CDU – 530.145 (043)

Ficha catalográfica elaborada por Romário Martins Ribeiro – CRB6 3595
Biblioteca Professor Manoel Lopes de Siqueira – Departamento de Física - UFMG

UNIVERSIDADE FEDERAL DE MINAS GERAIS
INSTITUTO DE CIÊNCIAS EXATAS
PROGRAMA DE PÓS-GRADUAÇÃO EM FÍSICA

FOLHA DE APROVAÇÃO

A presente tese, intitulada **"Interplay of crystalline strain and electronic properties in topological insulators and semiconductor thin films grown by Molecular Beam Epitaxy"**, de autoria de **GILBERTO RODRIGUES DA SILVA JUNIOR** submetida à Comissão Examinadora, abaixo-assinada, foi aprovada para obtenção do grau de **DOUTOR EM CIÊNCIAS**, em vinte e nove de abril de 2022.

Belo Horizonte, 29 de abril de 2022.

Prof. Ângelo Malachas de Souza
Orientador do estudante
Departamento de Física/UFMG

Prof. Myriano Henriques de Oliveira Junior
Departamento de Física/UFMG

Prof. Ricardo Wagner Nunes
Departamento de Física/UFMG

Profa. Beatriz Diaz Moreno
Canadian Light Source

Prof. Matheus Josué de Souza Matos
Departamento de Física/UFOP

Documento assinado eletronicamente por **Angelo Malachias de Souza**, **Membro de comissão**, em 02/05/2022, às 10:28, conforme horário oficial de Brasília, com fundamento no art. 5º do Decreto nº 10.543, de 13 de novembro de 2020.

Documento assinado eletronicamente por **Myriano Henriques de Oliveira Junior**, **Professor do Magistério Superior**, em 02/05/2022, às 12:17, conforme horário oficial de Brasília, com fundamento no art. 5º do Decreto nº 10.543, de 13 de novembro de 2020.

Documento assinado eletronicamente por **Matheus Josué de Souza Matos**, **Usuário Externo**, em 02/05/2022, às 13:10, conforme horário oficial de Brasília, com fundamento no art. 5º do Decreto nº 10.543, de 13 de novembro de 2020.

Documento assinado eletronicamente por **Beatriz Leonila Diaz Moreno**, **Usuária Externa**, em 19/05/2022, às 14:28, conforme horário oficial de Brasília, com fundamento no art. 5º do Decreto nº 10.543, de 13 de novembro de 2020.

Documento assinado eletronicamente por **Ricardo Wagner Nunes**, **Professor do Magistério Superior**, em 20/05/2022, às 08:59, conforme horário oficial de Brasília, com fundamento no art. 5º do Decreto nº 10.543, de 13 de novembro de 2020.

A autenticidade deste documento pode ser conferida no site https://sei.ufmg.br/sei/controlador_externo.php?acao=documento_conferir&id_orgao_acesso_externo=0, informando o código verificador **1421886** e o código CRC **063D67D5**.

Referência: Processo nº 23072.225023/2022-09 SEI nº 1421886

“Apenas que...

busquem conhecimento”

ET Bilu

Agradecimentos

Primeiramente quero agradecer aos meus pais, Kele e Gilberto, por ter me dado o apoio necessário para chegar até essa fase da minha vida e por me permitir dedicação exclusiva aos estudos, sem eles essa etapa não seria concluída. A minha irmã, Yasmim, pelo apoio e ajuda nas revisões do texto.

A Karine Paiva Pacheco Leles, minha amiga, companheira e esposa que esteve e estará sempre ao meu lado e se tornou uma pessoa essencial para minha vida, sem ela nada disso faria sentido.

Um agradecimento especial ao professor Dr. Ângelo Malachias que sempre me orientou em todos os momentos que precisei, contribuindo de diversas formas para minha formação acadêmica. Uma pessoa que tem minha admiração não só pelo grande cientista que é, mas também por toda simplicidade e amizade demonstrada ao longo desses anos de doutorado. Um eterno muito obrigado pela confiança e paciência durante a realização deste trabalho.

A todos aqueles que de alguma forma contribuíram para realização deste trabalho, com destaque para o Dr. Eduardo Abramof e Dr. Paulo Rappl pela ajuda e boa receptividade durante a minha estadia no INPE para o crescimento das amostras e para o professores Dr. Rogério Paniago e Dr. Gustavo Sáfar por toda a contribuição e conhecimento compartilhado durante a minha estadia no laboratório.

Também gostaria de agradecer ao Paulo Victor Sciammarella pela ajuda nas medidas de Raman, Lucas Marçal pela ajuda nas medidas de raios-X no LNLS, Thais Chagas pela ajuda nas medidas de STM/STS. Também quero deixar um agradecimento para o Erik Fissicaro que assim como eu é um dos sobreviventes do departamento de física da UFV. Obrigado pelas revisões e discussões sobre isolantes topológicos.

Finalmente agradeço as agencias de pesquisa CAPES e CNPq pela ajuda financeira.

Abstract

In this thesis, we studied three different types of samples, all obtained by the molecular beam epitaxy technique (MBE). In the first set of samples, epitaxial layers of Silicon-Germanium (SiGe) after the Germanium condensation process were studied. Our results show that, starting from a low concentration $Si_{0.92}Ge_{0.08}$ layer grown on top of a crystalline Si (001) on SOI substrates, we can reach desirable Ge concentration with a non-monotonic interplay on in-plane and out-of-plane strain. The Ge concentration and SiGe layer thickness was evaluated by a combination of secondary ion mass spectroscopy (SIMS) and synchotron X-ray measurements (diffraction and reflectivity).

In the second set of samples, we have studied the first stages of the heteroepitaxial growth of layered bismuth telluride (Bi_2Te_3) topological insulator on top of highly oriented pyrolitic graphite (HOPG). Samples were investigated by atomic force microscopy (AFM), synchrotron x-ray diffraction (XRD), and micro-Raman spectroscopy. AFM images show hexagonal/triangular flat islands with exposed HOPG areas for the low coverage regime. The existence of pseudomorphic strain at the initial Bi_2Te_3 layers was retrieved by both XRD and Raman spectroscopy.

Finally, in the third set of samples, we studied the morphological and electronic properties of Bi_2Te_3 layers doped with Europium (Eu) atoms. Bi_2Te_3 layers were deposited on a Barium fluoride (BaF_2) substrate and characterized by atomic force microscopy (AFM) and scanning tunneling microscopy/spectroscopy (STM/STS) techniques. Our results indicate regions along the sample surface in which the signature of the topological surface states disappears as well as the existence of a second crystalline phase.

Keywords: Synchrotron x-ray diffraction. Atomic force microscopy. Scanning tunneling microscopy/spectroscopy. Ge condensation. Bismuth telluride. Topological insulators.

Resumo

Nesta tese, estudamos três tipos diferentes de amostras, todas obtidas pela técnica de epitaxia de feixe molecular (MBE). No primeiro conjunto de amostras, foram estudadas camadas epitaxiais de Silício-Germânio (SiGe) após o processo de condensação de Germânio. Nossos resultados mostram que, a partir de uma camada de $Si_{0.92}Ge_{0.08}$ com baixa concentração de Ge, depositada sobre um Si cristalino (001) em substratos SOI (Silicon on Insulator), é possivel obter uma concentração desejável de Ge com uma relação não monotônica entre os strains no plano e fora do plano. A concentração de Ge e a espessura das camadas de SiGe foram determinadas através da técnica de espectroscopia de massa de íons secundários (SIMS) e medidas de raios X síncrotron (difração e refletividade).

No segundo conjunto de amostras, estudamos os estágios iniciais do crescimento heteroepitaxial do isolante topológico telureto de bismuto (Bi_2Te_3) sobre o grafite HOPG. As amostras foram analisadas por microscopia de força atômica (AFM), difração de raios X síncrotron (DRX) e espectroscopia micro-Raman. As imagens de AFM mostram ilhas planas hexagonais/triangulares com áreas do substrate de HOPG expostas para o regime de baixa cobertura. A existência de uma deformação pseudomórfica nas camadas iniciais de Bi_2Te_3 foi observada por XRD e corroborada por espectroscopia Raman.

Finalmente, no terceiro conjunto de amostras, estudamos as propriedades morfológicas e eletrônicas de camadas de Bi_2Te_3 dopadas com átomos de Európio (Eu). As camadas de Bi_2Te_3 foram depositadas em um substrato de fluoreto de bário (BaF_2) e caracterizadas pelas técnicas de microscopia de força atômica (AFM) e microscopia/espectroscopia de tunelamento (STM/STS). Nossos resultados indicam regiões ao longo da superfície da amostra em que a assinatura dos estados topológicos da superfície desaparece, bem como a existência de uma segunda fase cristalina.

Palavras-chave: Difração de raios-x sincrotron. Microscopia de força atômica. Microscopia/espectroscopia de tunelamento. Condensação de Ge. Telureto de bismuto. Isolantes topológicos.

Contents

1. INTRODUCTION **12**

2. THEORETICAL BACKGROUND **16**

2.1. EPITAXIAL GROWTH **16**

2.1.1. HETEROEPITAXY 18

2.1.2. VAN DER WAALS EPITAXY 21

2.1.3. BASICS OF ELASTICITY THEORY 23

2.1.3.1 Coherent energy 26

2.2. INTRODUCTION TO TOPOLOGICAL INSULATOR MATERIALS **28**

2.2.1. BASIC CONCEPTS OF TOPOLOGY 28

2.2.2. TOPOLOGICAL PHASES OF MATTER 31

2.2.3. TOPOLOGICAL INSULATORS 33

2.2.3.1 Magnetic impurities 41

3. MATERIALS **45**

3.1. SILICON-GERMANIUM ALLOY **45**

3.1.1. PROPERTIES OF SIGE ALLOY 46

3.1.2. SIGE HETEROEPITAXY 48

3.2. BISMUTH TELLURIDE **50**

3.2.1. THE BI_XTE_Y COMPOUND 50

3.2.2. THE BI_2TE_3 PHASE 52

3.2.2.1. Crystalline structure 52

3.2.2.2. Electronic structure 55

3.2.2.3. Vibration properties 59

4. EXPERIMENTAL TECHNIQUES **61**

4.1. MOLECULAR BEAM EPITAXY (MBE) **61**

4.2. X-ray diffraction (XRD) **65**
4.2.1. Bragg's Law and diffraction condition in reciprocal space 65
4.2.2. Measurement setup 70
4.2.2.1 2θ-ω Scans 72
4.2.2.2 Grazing Incidence Diffraction (GID) 74
4.3. X-ray reflectivity (XRR) **76**
4.3.1. Measurement setup 81
4.4. Atomic Force Microscopy (AFM) **82**
4.5. Scanning Tunneling Microscopy (STM) **85**
4.5.1. Measurement setup 88
4.5.2. Scanning Tunneling Spectroscopy (STS) 90

5. STRUCTURAL PROPERTIES OF SIGE LAYERS AFTER GE-CONDENSATION TECHNIQUE **94**

5.1. Introduction **94**
5.2. Methods **96**
5.3. Results **97**
5.3.1. Ultra-low Energy Secondary Ion Mass spectroscopy 97
5.3.2. X-ray diffraction 99
5.3.3. X-ray reflectivity 103
5.4. Discussion **104**
5.5. Conclusions **108**

6. STRUCTURAL AND ELECTRONIC PROPERTIES OF BI_2TE_3 GROWN ON HOPG GRAPHITE **109**

6.1. Introduction **109**
6.2. Methods **110**
6.2.1. Sample growth 110
6.2.2. Structural characterization 111
6.2.3. Band structure simulation 112
6.3. Results **112**
6.4. Discussion **120**

6.5. CONCLUSIONS **128**

7. LOCAL ELECTRONIC RESPONSE OF BI_2TE_3 TOPOLOGICAL INSULATOR UPON MAGNETIC DOPING **130**

7.1. INTRODUCTION **130**

7.2. METHODS **130**

7.3. RESULTS **132**

7.3.1. MORPHOLOGICAL CHARACTERIZATION 132

7.3.2. RAMAN CHARACTERIZATION 134

7.3.3. ELECTRONIC CHARACTERIZATION 136

7.4. DISCUSSION **139**

7.4. CONCLUSION **142**

8. GENERAL CONCLUSIONS **144**

REFERENCES **146**

1. Introduction

The development and improvement of devices based on crystalline semiconductor materials is extremely important for the technological stage in which modern society is inserted. A good example of this is the frequent use of micro and optoelectronic devices in the most diverse daily activities. The simple fact of changing the TV channels through the remote control or watch a streaming service on mobile is only possible due to the existence of these types of devices.

The current progress of electronics began with the development of the first transistor, a three-terminal device that made it possible to switch the electric current inside a semiconductor [1]. This device associated with the miniaturization process replaced the triode valves, which presented major limitations for electronics, as they were large and fragile [1]. Since then, the miniaturization of electronic devices has allowed increasingly powerful computers with more memory capacity to be built, which in turn allows increasingly complex circuits to be designed and executed at a lower cost. As an example, the MOSFET device (Metal Oxide-Semiconductor Field Effect Transitor), the main component of the electronics industry today, has been systematically reducing its dimensions since the 70's with what came to be called Moore's Law.

All this development, however, does not come without cost. Many researches are realized in order to ensure that the so-called Moore's Law grew at the same rate as the device dimension decreased [2]. Based on this, the search for materials and suitable growth techniques that allows the development of devices with reduced cost and high efficiency has become essential for our society. In this scenario, Silicon (Si) and Silicon oxide (SiO_2) are very important for the industry. Due to the large availability of Si and the advantageous properties of its associated oxide, they remained for long time the heart of most of semiconductor devices. However, over the years, the emergence of molecular beam epitaxy made it possible to combine several other materials with silicon to produce better, smaller and faster devices [3-5]. With devices approaching the nanoscale, electrical transport

properties within silicon appear as a limiting factor and researchers evaluate other semiconductors as possible substitute. Germanium (Ge) is one of the material candidates since it offers faster electrical transport over Si (2 times higher electron mobility and 4 times hole mobility) and is extensively investigated for more than a decade [6].

Another alternative is to explore the so-called strain engineering, since it can be used to modify various materials properties such as electronic band structure [7-9], electronic transport [10], optoelectronic properties [11], phonon structure [12], and kinetics and thermodynamics of atom motion and structure [13]. These characteristics motivate studies of Silicon-Germanium alloy. Since it represents the possibility of including the properties of Ge in the already stable technology of silicon-based devices, in addition to allowing the development of high-quality substrates for the growth of strained Silicon.

Another class of materials that are attracting the attention of the scientific community are topological insulators materials (TI). This class of materials presents unique electronic properties, being insulators in their bulk and conductors at the surface. These topological surface states are backscattering protected and have spin polarization. As a consequence, an extensive research focused on TIs is currently being done, in order to better understand their electronic behavior. This will enable its use in novel devices, especially in spintronics and quantum computation [14-16].

The possibility of studying surface states in alloys emerged from the experimental evidence that binary alloys of the Bi_xSb_{1-x}, with $0.07 < x < 0.22$, presented characteristics of three-dimensional topological insulators [17]. In these materials, as a consequence of a strong spin-orbit interaction, an inversion between the valence and conduction bands occurs at certain points in the Brillouin zone [18]. This feature allows the existence of gapless surface states protected by time-reversal symmetry. In 2009, surface conductive states were detected in stoichiometric compounds of the V-VI group of the periodic table, as, for example, in bismuth selenide (Bi_2Se_3), in bismuth telluride (Bi_2Te_3) and antimony telluride (Sb_2Te_3), which were named second generation topological insulators [19].

The manufacture of devices based on Bi_2Se_3, Bi_2Te_3 and Sb_2Te_3 has posed a great challenge for researchers. These materials feature a crystal structure that is highly sensitive to growth conditions. The introduction of defects in the crystal lattice potentiates the bulk carrier density and, consequently, makes it difficult to detect the surface conductive states. In this sense, the synthesis of materials with high quality and nanometric dimensions is an interesting alternative since the large surface-to-volume ratio allows the use of these nanomaterials as platforms to study the topological states, reducing the contribution of bulk charge carries [20, 21]. In addition, a study of topological insulators doped with magnetic atoms can provide a better understanding of the robustness of surface states as well as to providing a platform for the study of the so-called Quantum Anomalous Hall Effect [22-24].

This thesis was divided as follows: Chapter 2 presents the theoretical background necessary to understand the results obtained in this work. A definition of heteroepitaxy and van der Waals epitaxy as well as fundamental concepts of strain and coherent energy is presented. This chapter also reviews the main concepts found in the study of topological insulators materials. In chapter 3, a review is made on the main properties of the silicon germanium alloy and the bismuth telluride, materials studied throughout this work. In chapter 4 the main experimental techniques used in the growth and characterization of the samples are presented. Focusing on Molecular Beam Epitaxy (MBE), X-ray diffraction (XRD) and reflectivity (XRR) techniques as well as atomic force microscopy (AFM) and Scanning Tunneling microscopy (STM) techniques. Finally, in chapters 5, 6 and 7 the main results obtained in this work are presented, followed by the general conclusions in chapter 8 and the main references that were the basis for this work.

With respect to chapter 5, the main results obtained in the analysis of SiGe layers grown by MBE under the action of the germanium condensation technique are presented. The Ge condensation process is known as a crucial tool to induce well-defined strain on Si or SiGe layers with potential use in semiconductor devices. The structural properties of SiGe layers as a function of oxidation time is evaluated by a combination of ultra low energy secondary ion mass spectroscopy (ULE-SIMS) and synchrotron X-ray measurements (diffraction and reflectivity).

Chapters 6 and 7 are dedicated to the study of Bi_2Te_3 topological insulator. In chapter 5, a systematic study of Bi_2Te_3 nanostructures grown on HOPG graphite (Highly Ordered Pyrolytic Graphite) is carried out. Characterized by having an inert surface, ideal for growth via van der Waals epitaxy, the choice of graphite with substrate is interesting due to the little approach found in the literature on these heterostructures, especially with regard to exploration by X-ray diffraction techniques. Furthermore, the integration of topological insulators with graphite made it possible to explore interesting phenomena in condensed matter, such as, for example, the study of Dirac fermions. In Chapter 6 we studied Europium-doped Bi_2Te_3 thin films grown on a barium fluoride (BaF_2) substrate. From the epitaxy point of view, BaF_2 is the most suitable substrate for the growth of Bi_2Te_3 layers due to the similarity in the lattice parameter. However, the influence of magnetic atoms on the Bi_2Te_3 lattice is still an open question. Based on this, this chapter presents the main results of a systematic study of the electronic properties of Bi_2Te_3 films under different Europium concentrations, mainly by the Scanning Tunneling Spectrocopy (STS) technique.

2. Theoretical background

2.1. Epitaxial growth

The term epitaxy, initially introduced by Royer in 1928 [25], is of Greek origin epitaxis, a term formed by the junction of the elements Epi, which means “on”, and Taxis, which means “arrangement” and, therefore, refers to the growth of atomic layers on a single crystal surface known as substrate. In this process, atoms or molecules are deposited on a substrate so that the grown layer has the same crystallographic orientation as the substrate.

Epitaxial growth is an example of a dynamic phase transition, that is, a stable phase grows from a metastable phase (solid, liquid or gas) [26]. A schematic illustration of the first step during crystallization process is shown in figure 2.1, in which phase B represents the metastable state and phase A the stable state. Each of these panels shows a different stage of the epitaxial growth process, that is, they refer to different growth times. Inittialy, there is a mass transport of the constituent species from the bulk of the metastable phase towards the substrate. In panel(a), the material (B), referring to the film to be grown, comes into contact with the substrate geometric interface. The substrate (A), in addition to being the matrix in which the film will attach, serves as a support for its growth.

Mass transport is an extremely complex phenomenon, as it is influenced by several factors such as temperature and concentration gradients [26]. It mainly involves two processes: incident atomic/molecular flow and diffusion. The atoms coming from the incident flux suffer the action of a series of kinetic effects when reaching the substrate surface: adsorption, desorption and diffusion [25,26] explained in the next three paragraphs.

Adsorption is a process in which the incident atom interacts with the substrate surface, forming bonds with the surface atoms. This step can be divided into chemical and physical adsorption. In physical adsorption, atoms undergo weak interactions of an electromagnetic nature through van der Waals forces. In the chemical adsorption condition, the atoms are effectively incorporated to the substrate surface due to covalent or ionic bonds.

Desorption process represents the opposite mechanism of that explained in the previous paragraph, where the atom leaves the crystallization front. This process depends on conditions such as substrate temperature and insufficient surface contact time for the formation of chemical bonds and must be taken into account in order to understand the overall deposition rate.

Finally, diffusion is a surface migration process, which involves a lateral mass transport that enables the formation of the epitaxial layer due to the search for the minimization of surface energy. It is important to emphasize that there is a competition between diffusion and desorption, as both are thermally activated processes. Simultaneously, the nucleation process occurs, associated with the formation of successive monolayers as coverage increases [26].

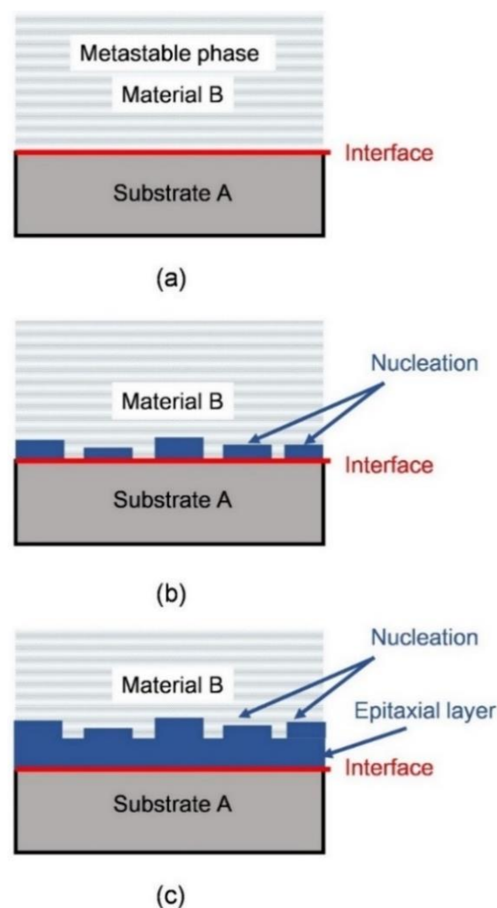

Figure 2.1: Different steps during the process of forming an epitaxial layer. (a) Before growth begins. The substrate in crystalline form is prepared to receive the atoms/molecules that will impinge on it, (b) beginning of the nucleation process, nucleations always precede the appearance of epitaxial structures such as layers or islands. (c) Representation of an epitaxial layer at its final (grown) condition. The figure is adapted from Ref. [26].

The growth process begins with nucleation, as shown in Panel (b). The nucleation results from the spontaneous formation of small clusters of atoms/molecules with some critical size. Such size is determined by the balance between the vapor pressure of the constituent material and the environmental pressure [26]. Morever, the entire nucleation process is directly linked to the chemical and physical properties of the chosen substrate [26]. From this process, these nuclei grow occupying the entire surface of the substrate, leading to the formation of the epitaxial layer, as shown in Panel (c). All epitaxial layers, or other structures such as islands, appear as products of the nucleation process that always precedes them.

2.1.1. Heteroepitaxy

The success in an epitaxial growth is directly related to the existence of a similarity between the chemical and physical structures of the materials that constitutes layers and the substrate. Therefore, the most direct way to guarantee this similarity is the deposition of atoms on a substrate of the same material, a process known as homoepitaxy. However, the process of deposition of atoms on a substrate of different chemical composition and even crystalline structure, known as heteroepitaxy, is of extreme technological importance.

In heteroepitaxial growth, the layer and the substrate may not have the same lattice parameter. This difference, if sufficiently restricted (< 5 %), is accommodated through strains in the epitaxial layer in an attempt of the deposited material to adapt to the crystal lattice of the substrate. Therefore, as a consequence of the strain, the deformation of the unit cell occurs so that in-plane lattice parameters ($a_{||}$) are matched at the film-substrate interface, forming a so-called pseudomorphic (coherent) layer, as represented schematically in figure 2.2 for a cubic structure for simplicity. The lattice parameter perpendicular to the growth plane ($a_{\perp}$) will also be strained as the unit cell volume is partially preserved. It can be larger (Fig. 2.2(a)) or smaller (Fig. 2.2(b)) compared to its original bulk crystal value (a_L).

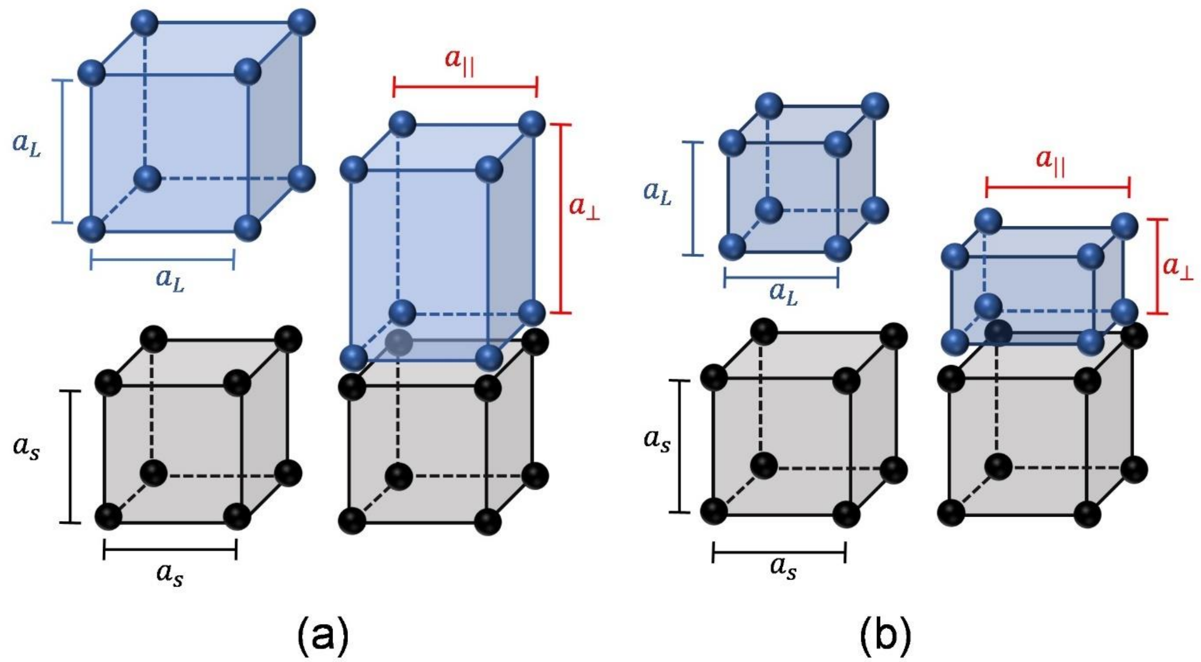

Figure 2.2: Lattice parameter accommodation process during epitaxial growth. In (a) the deformation of the unit cell is represented when $a_L > a_S$ in this case the layer is subjected to a compressive in-plane strain. In (b) is represented the case where $a_L < a_S$ in this case the layer is subjected to a tensile in-plane strain. The blue cube represents the deposit layer materials whereas the gray cube represents the substrate material.

This deformation of the unit cell causes an accumulation of elastic energy in the system that increases with increasing layer thickness. Therefore, the pseudomorphic growth ($a_{||} = a_S$) occurs up to a certain threshold of thickness, called critical thickness [26-28]. For larger coverage values the layer starts to relax dissipating the accumulated elastic energy and returning its lattice parameter to bulk values, independently from the substrate lattice parameter. Figure 2.3 illustrates a relaxed epitaxial layer over a crystalline substrate. In this case, both the in-plane and out-of-plane lattice maintain their bulk values, that is, $a_{||} = a_\perp = a_L$.

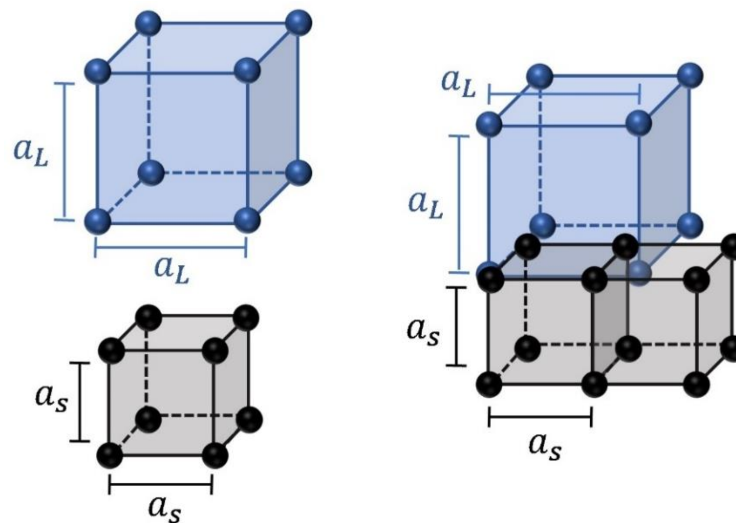

Figure 2.3: Schematic representation of the fully relaxed epitaxial layer unit cell over the substrate lattice.

This transition from the fully strained state to the fully relaxed state must be understood in order to obtain an epitaxial layer with low defect density. When growth occurs coherently, the crystalline arrangement of the substrate is reproduced by the layer, resulting in an interfacial region in perfect crystallographic registry, as shown in figure 2.4(a). However, when the critical thickness is reached and the layer is at the onset of plastic relaxation the formation of linear defects at the interface is observed, and the regular arrangement of atoms is locally interrupted, leaving dangling bonds at the interface as can be seen in figure 2.4(b). These defects arise in order to accommodate materials that exhibit a large lattice mismatch and are called misfit dislocations [26]. The presence of such defects at the layer/substrate interface can cause disorientation of the crystalline domains (crystallites) of the layer that can compromise epitaxial growth, that is, the layer can become polycrystalline (with a strong texture or reduced mosaicity).

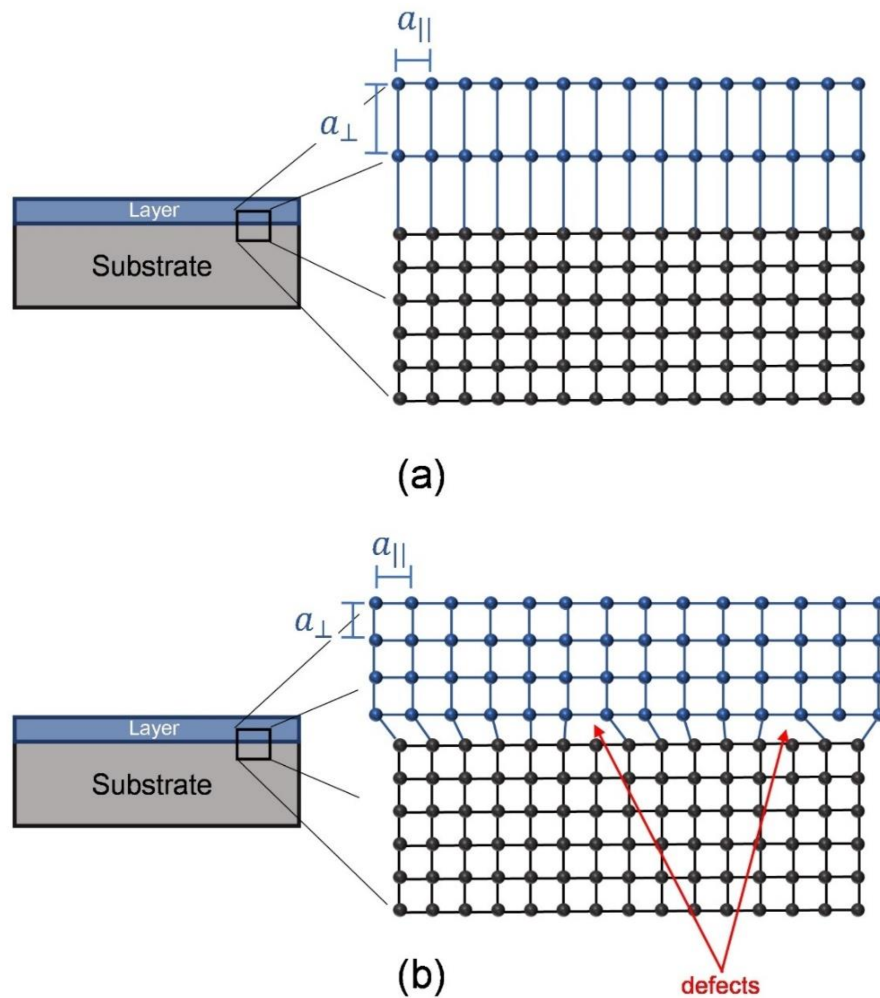

Figure 2.4: Different characteristics of the layer/substrate interface. (a) Fully strained layer resulting in a perfect crystallographic registry with a defect-free interface. (b) State of total relaxation of the layer where defects are introduced at the interface.

2.1.2. Van der Waals epitaxy

As previously mentioned, the growth of an epitaxial layer/film can be classified into two categories: homoepitaxy and heteroepitaxy. In more conventional epitaxial growth processes, the layer is chemically bonded to the substrate, and the structural differences between the materials involved determine the crystalline quality of the material grown. In this sense the choice of substrate is of fundamental importance in heteroepitaxial growth. A priori, the substrate must have a crystalline structure similar to that of the material to be grown, and the lattice parameters of both must not differ by more than approximately 5%. Such restriction limits the number of heterostructures that can be developed since the

lattice mismatch between the materials leads, in the growth of the samples, to properties considered undesirable, such as: high interfacial strain, high density of defects and formation of secondary phases due to segregation.

In this context, the anisotropic character at the a-b plane which is observed in materials such as graphene, boron nitride (hBN) and the chalcogenides of the V-VI group (Bi_2Te_3, Bi_2Se_3 and Sb_2Te_3) allows exploring a new aspect of epitaxial growth. The crystal structure os these materials result from the stacking of two-dimensional atomically-thin layers where the interlayer bond is quite strong, of the covalent type, but the connection between the layers is weak, predominantly consisting of van der Waals interactions. Heteroepitaxy in these systems can therefore be reffered as van der Waals epitaxy. In this type of epitaxy, schematically represented in figure 2.5, the mismatch condition between the crystalline structures is relaxed precisely because the film/substrate interface is not formed by chemical bonds, but by van der Waals interactions. Even if one of the materials involved is not a layered material, it is still possible to obtain epitaxy with the condition that the material surface does not have dangling bonds, therefore it is possible combine a variety of crystal structures.

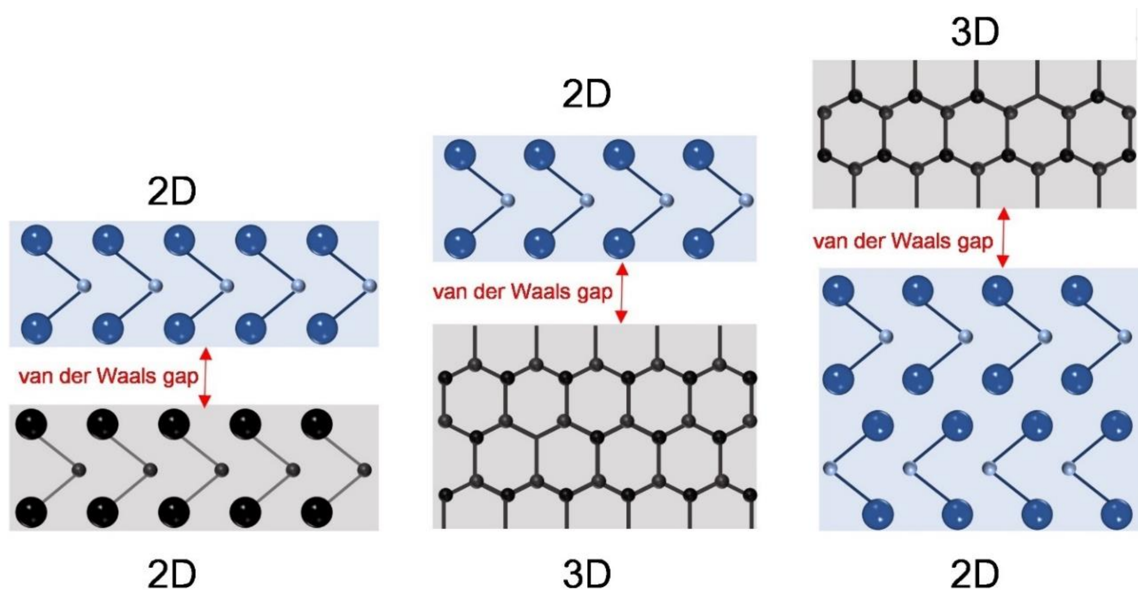

Figure 2.5: Schematic representation of van der Waals epitaxy. In this system, it is possible to observe the van der Waals gap at the layer-substrate interface relaxing the lattice mismatch condition found in convention epitaxy, nevertheless the overlayer grows oriented with the substrate. The figure is adapted from Ref. [29].

The van der Waals forces (vdW) do not represent a chemical bond between two materials, having their origin in the interaction between the induced dipole moments of the atoms involved [29, 30]. Thus, when compared to ionic/covalent bonds, the interaction of vdW is a weak interaction that allows the formation of a strain-free epitaxial layer, that is, the value of the lattice parameter in the material plane is the one referring to the bulk crystal even in the early stages of growth. Consequently, it is possible to obtain nanostructures with good crystalline quality even if the difference in the lattice parameter of the materials involved is larger than 40% [30].

2.1.3. Basics of elasticity theory

When an elastic body is subjected to stress, changes in size and shape occur as a consequence of the applied force. This sentence can be extended to an epitaxial layer since, as previously discussed, when it grows on a lattice-mismatched substrate, the layer can adopt the in-plane lattice constant of the substrate due strains that arise in the system. In a cubic lattice, the in-plane ($\varepsilon_{||}$) and out-of-plane ($\varepsilon_{\perp}$) strain components can be calculated in terms of the corresponding bulk value a_L:

$$\varepsilon_{||} = \frac{a_L^{||} - a_L}{a_L}, \tag{2.1}$$

$$\varepsilon_{\perp} = \frac{a_L^{\perp} - a_L}{a_L}, \tag{2.2}$$

where $a_L^{||}$ and $a_L^{\perp}$ are the in-plane and out-of-plane lattice parameter of the layer, respectively. A more general description can be made exploring the linear relationship between an applied stress σ and the strain ε, i.e, the corresponding deformation of the lattice due to applied force. This relationship is defined by generalized Hooke's Law [31, 32]:

$$\sigma_{ij} = \sum_{kl} c_{ijkl} \varepsilon_{kl}. \tag{2.3}$$

In this equation, σ_{ij} is the force per unit area along the direction i applied on a surface where the normal is oriented in the the j direction, ε_{ij} is the relative deformation along the i direction of that volume surface and c_{ijkl} are components of the fourth-order rank tensor (*stiffness* tensor) that defines the elastic constants of material. Components of the stress

tensor with repeating indices $i = j$ (e.g, σ_{11}) are defined as normal stress whereas those with different indices $i \neq j$ (e.g, σ_{12}) are denoted as shear stress.

Commonly, the c_{ijkl} tensor has $3^4 = 81$ elements. However, the symmetry properties of stress and strain tensors ($\sigma_{ij} = \sigma_{ji}$ and $\varepsilon_{ij} = \varepsilon_{ji}$) require 6 equations to calculate stress from strain since each tensor has only 6 independent terms. Based on this, the fourth-order *stiffness* tensor c_{ijkl} can be written in matrix notation $c_{\alpha\beta}$ (a tensor of second order) and the tensor indices can be simplified as follows:

Tensor notation (ij): 11 22 33 23,32 31,13 12,21

Matrix notation (α): 1 2 3 4 5 6

With this notation the *stiffness* tensor can be reduced to a matrix with 36 independents elements that depending on symmetry of the material can be further simplified.

For a cubic system oriented as show in figure 2.6, the symmetry allows to reduce the number of materials elastic constants to only three independent components c_{11}, c_{12}, c_{44}, and Eq. (2.3) reduces to:

$$\begin{cases} \sigma_{xx} = c_{11}\varepsilon_{xx} + c_{12}\varepsilon_{yy} + c_{12}\varepsilon_{zz} \\ \sigma_{yy} = c_{12}\varepsilon_{xx} + c_{11}\varepsilon_{yy} + c_{12}\varepsilon_{zz} \\ \sigma_{zz} = c_{12}\varepsilon_{xx} + c_{12}\varepsilon_{yy} + c_{11}\varepsilon_{zz} \\ \sigma_{ij} = c_{44}\varepsilon_{ij}, i \neq j \end{cases} \tag{2.4}$$

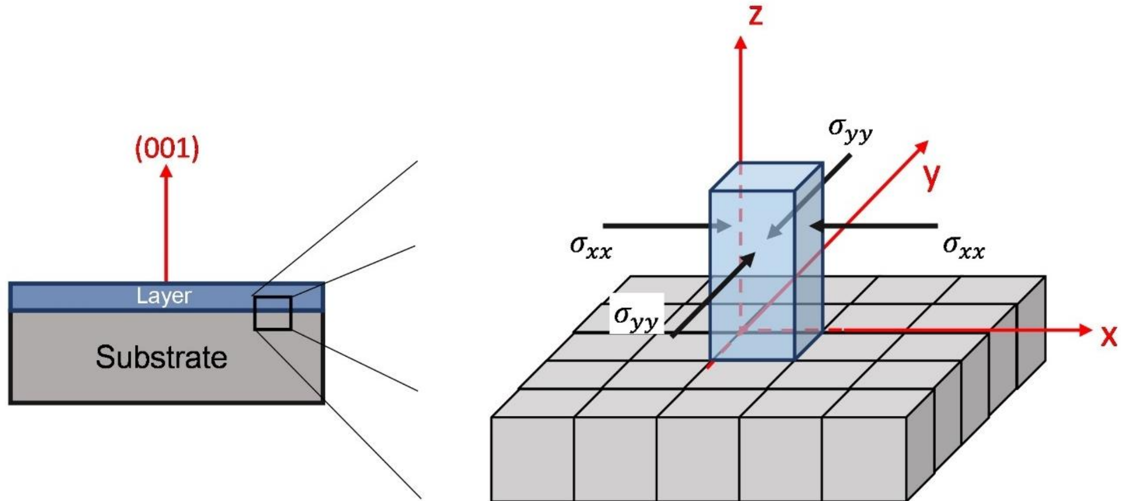

Figure 2.6: Schematic representation of an epitaxial layer ($a_L > a_s$) under the action of in-plane biaxial stress. The cubic substrate is oriented along [001] crystalografic direction. As a consequence of the strain, the unit cell of the material that forms the layer is deformed in order to adopt the lattice parameter of the substrate, forming a coherent interface ($a_L = a_s$).

Applying this result to an epitaxial layer deposited on a cubic substrate oriented along the [001] direction, i.e, the growth direction is defined along the z axes (see figure 2.6), the layer is deformed so that the lattice parameter in lateral direction (i.e x and y directions) are forced to match the lattice parameters of the substrate $a_L^{||} = a_S$. In this case, $\sigma_{zz} = 0$ since along this direction the layer is free to rearrange itself and the stress is delimited within the plane of the layer $\sigma_{xx} = \sigma_{yy} = \sigma_{||}$. Hence, the epitaxial layer strain components can be written in terms of material elastic constants:

$$\sigma_{zz} = c_{12}\varepsilon_{xx} + c_{12}\varepsilon_{yy} + c_{11}\varepsilon_{zz} = 0,$$
$$\varepsilon_{zz} = -2\frac{c_{12}}{c_{11}}\varepsilon_{yy} \text{ or } \varepsilon_{\perp} = -2\frac{c_{12}}{c_{11}}\varepsilon_{||}. \tag{2.5}$$

From this result it is possible to observe that the strain components have opposite signs, which means that the system tends to preserve the unit cell volume.

If the same formalism described above is applied to a hexagonal geometry the set of independent elastic constant become c_{11}, c_{12}, c_{13}, c_{33}, and c_{44}. In this case, for simplicity, the z direction is aligned with the c-axis of the hexagonal lattice. Then, the relationships between stress σ and strain ε is expressed by [32]:

$$\begin{cases} \sigma_{xx} = c_{11}\varepsilon_{xx} + c_{12}\varepsilon_{yy} + c_{13}\varepsilon_{zz} \\ \sigma_{yy} = c_{12}\varepsilon_{xx} + c_{11}\varepsilon_{yy} + c_{13}\varepsilon_{zz} \\ \sigma_{zz} = c_{13}\varepsilon_{xx} + c_{13}\varepsilon_{yy} + c_{33}\varepsilon_{zz} \\ \sigma_{xy} = c_{44}\varepsilon_{xy} \\ \sigma_{xz} = \frac{(c_{11}-c_{12})}{2}\varepsilon_{xz} \end{cases} \tag{2.6}$$

In the case of an epitaxial growth, again, we consider a biaxial strain $\sigma_{zz} = 0$, $\sigma_{xx} = \sigma_{yy} = \sigma_{||}$ and $\sigma_{ij} = 0$ for $i \neq j$, thus from equation 2.6 the strain state in the layer can be written as:

$$\sigma_{zz} = c_{13}\varepsilon_{xx} + c_{13}\varepsilon_{yy} + c_{33}\varepsilon_{zz} = 0,$$
$$\varepsilon_{zz} = -2\frac{c_{13}}{c_{33}}\varepsilon_{yy} \text{ or } \varepsilon_{\perp} = -2\frac{c_{13}}{c_{33}}\varepsilon_{||}. \tag{2.7}$$

The Elastic constants c_{ij} are expressed in terms of measurable quantities such as Poisson's ratio ν, shear modulus G and Young's modulus E. These quantities are usually measured using macroscopic tests such as uniaxial stress or pure shear. The Young's modulus E is an elastic constant that characterizes the stiffness of the material, that is, the higher the value of E, the more difficult it is to deform the material. The Poisson's ratio ν is

defined as the ratio between lateral and longitudinal strain in a condition of uniaxial tensile stress. Finally, the shear modulus G measures the material response upon shearing strains.

Sometimes it is more convenient to write Hooke's law in the inverse form, which means write the strain ε as a function of stress σ:

$$\varepsilon_{ij} = \sum_{kl} s_{ijkl}\sigma_{kl}, \tag{2.8}$$

here, the elements s_{ijkl} define the compliance tensor that are obtained from the relation $s_{ijkl} = \left(c_{ijkl}\right)^{-1}$.

2.1.3.1 Coherent energy

The ability of solid materials to deform under the application of an external force inevitably results in a buildup of strain energy. For systems where Hooke's law is valid, the general form of energy can be written as [31]

$$U = \frac{1}{2}\sum_{kl} c_{ijkl}\varepsilon_{ij}\varepsilon_{kl}, \tag{2.9}$$

where U is the strain energy per unit volume and, as expected, it is a quadradic function of the strain ε.

Based on this condition is possible to calculate the elastic energy accumulated in an epitaxial layer that are coherent strained with their substrate. Here it is possible to make an analogy with a rubber sheet. Experimentally, it is easier to deform (compress or stretch) a thinner rubber sheet than a thicker one. Therefore, as in epitaxy the substrate is usually thicker than the layer over it, it is reasonable to consider that at the initial growth stages the heterostructure are characterized by the pseudomorphic condition for which the elastic energy of deformation is stored in the epilayer lattice.

In this context, only the normal stress and strain in two perpendicular axes are considered to be produced as a result of lattice mismatch in epitaxial growth [32, 33]. When $\sigma_{zz} = 0$, Hooke's law written in terms of compliance components boils down to:

$$\varepsilon_{xx} = s_{11}\sigma_{xx} + s_{12}\sigma_{yy}, \tag{2.10}$$

$$\varepsilon_{yy} = s_{11}\sigma_{yy} + s_{12}\sigma_{xx}. \tag{2.11}$$

In the case where the layer and substrate are hexagonal and the last is oriented along the [0001] crystalografic direction (see figure 2.7), the in-plane strains (x and y

directions) are equal as required by symmetry and can be written in terms of lattice misfit f_m between the layer and the substrate.

$$\varepsilon_{xx} = \varepsilon_{yy} = f_m = \frac{a_L - a_s}{a_s}, \tag{2.12}$$

where a_L and a_s represent respectively the unstrained lattice parameters of the growth layer and the substrate. Using Eqs. (2.10) and (2.11), the stresses in the film/substrate interface can then be written as

$$\sigma_{xx} = \sigma_{yy} = \frac{1}{(s_{11}+s_{12})} \frac{a_L - a_s}{a_s}. \tag{2.13}$$

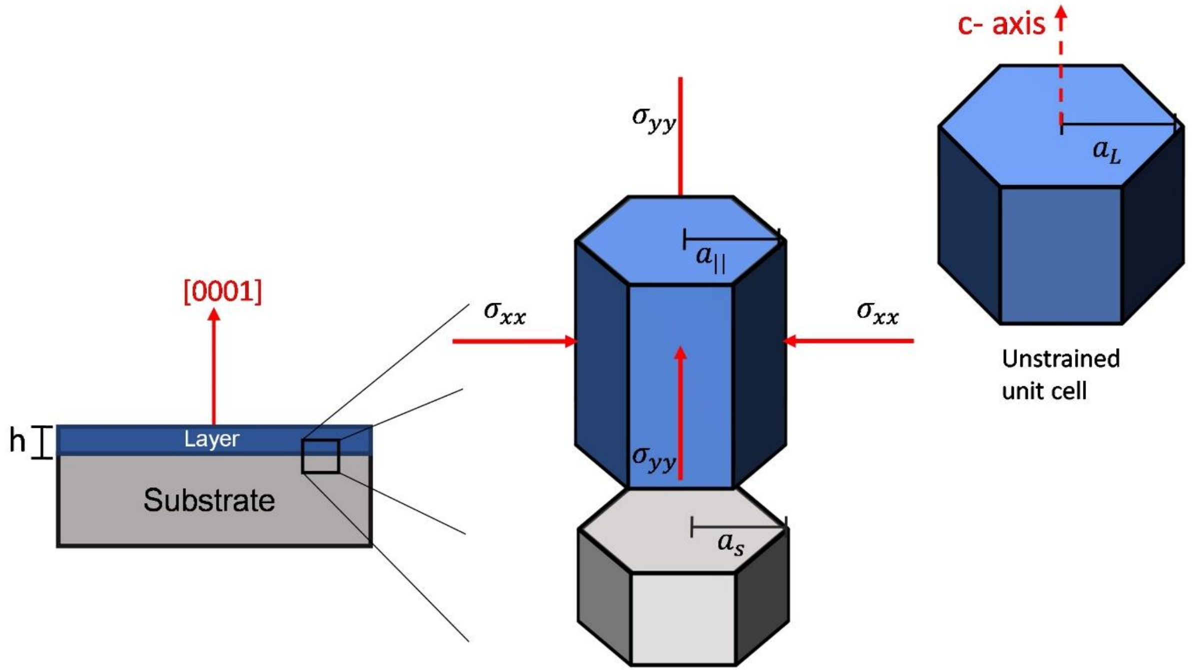

Figure 2.7: Sketch of an epitaxial layer coherently strained on a hexagonal substrate oriented along [0001] direction. Due to lattice mismatch between layer and substrate a in-plane biaxial stress arises resulting in an accumulation of elastic energy in the layer.

Hence from Eq. (2.9), assuming that the shear terms ($i \neq j$) are zero, the strain energy per unit volume is simply

$$U = \frac{1}{(s_{11}+s_{12})} \left(\frac{a_L - a_s}{a_s}\right)^2. \tag{2.14}$$

The cohence energy is then calculated multiplying equation 2.14 by the layer thickness h [33]:

$$u_{coh} = \frac{1}{(s_{11}+s_{12})} \left(\frac{a_L - a_s}{a_s}\right)^2 h, \tag{2.15}$$

from this equation it is possible to quantitatively infer the phenomenological discussion presented in section 2.1.1. The strain increases linearly with the layer thickness and depends on lattice mismatch. As a consequence, the strained growth mode is limited up to a critical thickness above which the system releases elastic energy favoring the appearance of defects.

In an epitaxial film composed of multilayers each with a different lattice parameter and comparable thickness, each layer deforms significantly when the crystal lattices are joined at their interfaces. Given the condition that, during coherent growth, the in-plane parameter must be the same on all interfaces, the multilayer coherency energy can be calculated by summing expressions such as Equation 2.15 for each layer [31]:

$$u_{coh} = \frac{1}{(s_{11}+s_{12})} \sum_i {\varepsilon_{i,//}}^2 h_i, \tag{2.16}$$

where h_i and $\varepsilon_{i,//}$ are the thickness and parallel strains of the i'th layer.

2.2. Introduction to topological insulator materials

In the last decade, materials called topological insulators (TI) have become objects of intense scientific investigation around the world. In a simplified way, these materials are characterized by having bulk states with energy band gap, but exhibiting gapless metallic states (conductors) in their edges or surfaces, protected by time reversal symmetry. The electrical conduction channel limited to the material boundary makes it possible to select the spin state of electrons, resulting in effects such as spin-dependent electronic transport without dissipation. This feature provides developments in spintronics and quantum computation, areas of fundamental interest in the current technological scenario.

2.2.1. Basic concepts of topology

Topology is a branch of mathematics that studies the shape properties of certain geometric objects that are insensitive to smooth deformations [34]. As an example, a soccer ball (sphere) can be deformed smooth and continuously into many different shapes, such as

a rubik's cube or wine glass, as depicted in Fig. 2.8(a), defining a manifold where these objects are equivalents even with a clear distinct geometric characteristic. Similarly, as ilustrated in Fig. 2.8(b), a doughnut is equivalent a coffee cup as both can be smootly deformed into each other. However, a sphere cannot be smoothly deformed into a surface of a donut, since in this process it is necessary to tear the surface representing a discontinous operation, which means that these two objects are topologically differents.

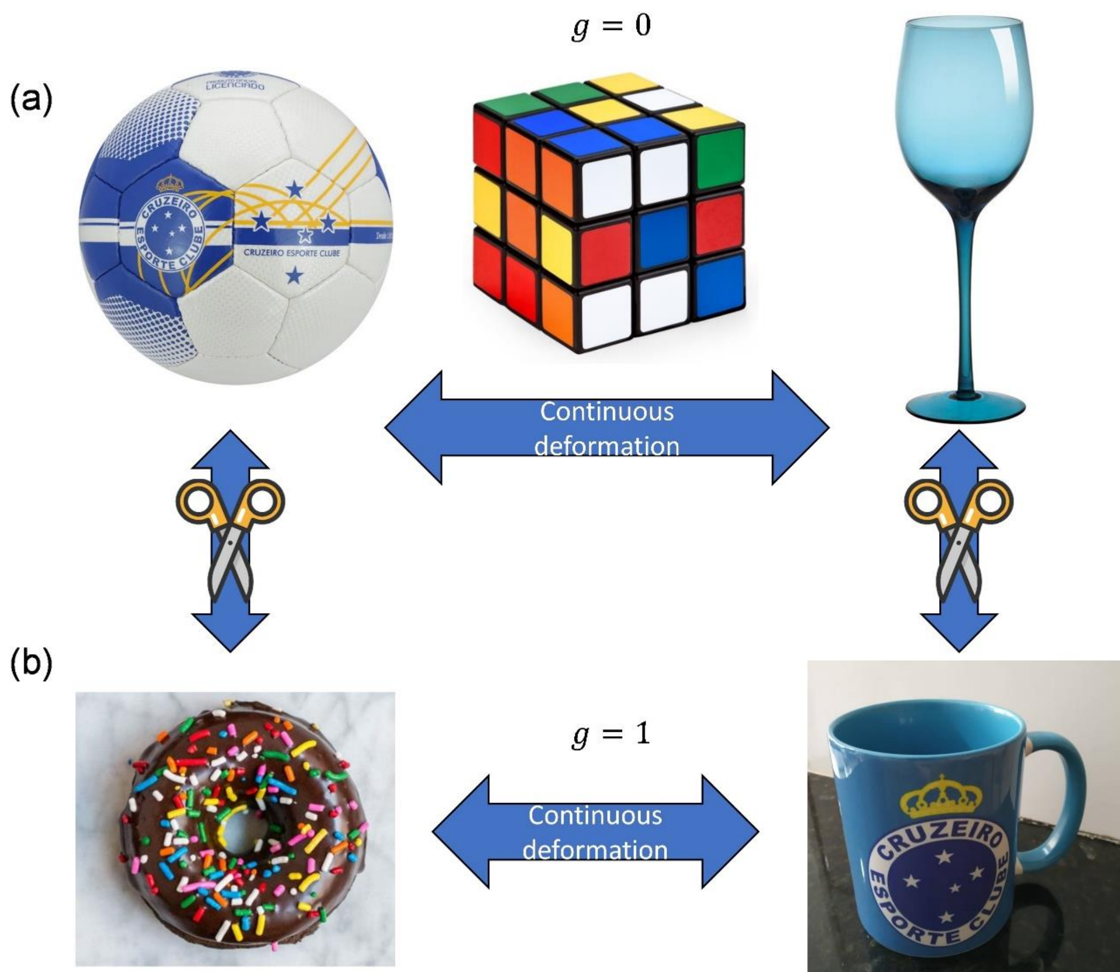

Figure 2.8: Schematic representation of topology. The ball, the cube and wine glass have completely different shapes. However, because they are connected through continuous deformation, they have the same topology. The cup and the donut have the same relationship. However, to transform the donut into the ball, for example, the penetrating hole in the donut must be filled in. Thus, it has a different topology, as it cannot be continuously deformed.

Formally, the topology of closed two-dimensional surfaces in three-dimensions can be defined by its genus g that essentially counts the number of holes in the surface [34]. An important result is expressed by the Gauss-Bonnet theorem which states that the surface integral of Gaussian curvature K over a surface of an object $\mathcal{O}$ is an invariant quantity, whose value is related to genus g, as shown in equation (2.17) [34].

$$\int_{O} KdA = 2 - 2g \ . \tag{2.17}$$

As a consequence of this theorem, although the integrand depends on surface details, the right side of the equation (2.17) remains unchanged unless a hole is created in the surface. Therefore, topological classification focuses on fundamental distinctions between objects regardless of geometric details (like distances and angles), being the smooth deformation of the object (one that does not cut or tear the surface) the fundamental concept to group it according to this classification. In this context, a donut has $g = 1$ while a sphere has $g = 0$ and these different equivalence classes are distinguished from each other by means of an integer number, so called topological invariant. Hence, there is no smooth and continous deformations that connect these two surfaces without change the topological invariant and, consequently, the topological class.

The concepts of topology can be extended to more abstract spaces, for example, the $\boldsymbol{k}$ space, where eletrons are studied. Therefore, in the field of band theory in solids, the process of smooth deformation can be applied in order to characterize the Hamiltonian (set of Bloch wave function) of a system with many particles that has an energy gap for electronic excitations, which separates the ground state from all excited states, like insulators and semiconductors [35]. This allows for a concept of topological equivalence classes in a similar way as described for geometrical objects. In this scenario, quantum phases with an energy gap are topologically equivalent if they can be smoothly deformed into one another without closing the gap, i.e, an adiabatic transformation is applied in one of the parameters of your Hamiltonian so that the energy gap remains finite. If such smooth deformation is not possible, the insulators materials are not in the same topological class, and a conection between them necessarily implies a phase transition that, in this case, means close the gap.

2.2.2. Topological phases of matter

The concept of topological invariants that allows classifying Hamiltonians of differents insulating systems started with Chern's theorem, which is a generalization of Gauss-Bonnet theorem discussed in the previous section. Analogously to equation 2.17, this theorem states that the integral over a curvature, in this case the Berry curvature of the energy band, carried out on the boundaries of the Brillouin zone is a quantized topological invariant $n \in \mathbb{Z}$, called Chern number [36]. Based on that, it is possible to define topological classes depending on the value of this invariant in a similar way to the concept of *genus* discussed earlier. Generally, $n = 0$ means a so-called trivial insulator while $n \neq 0$ is said to be non-trivial.

A fundamental consequence of this classification is the existence of gapless conducting states at interfaces where the topological invariant changes [36-38]. An important evidence of this is observed in the integer quantum Hall effect (figure 2.9). Due to the strong external magnetic field applied perpendicularly to electrons confined to a two-dimensional surface at low temperatures, the electron orbits occupy discrete values of energy, the Landau levels. The presence of occupied and unoccupied Landau levels results in an energy gap, characteristic of a conventional insulator, but unlike what is observed in a common insulator, the presence of an electric field in the plane of electron motion results in a current along the edges of the material, the direction of which depends directly on the applied magnetic field. The edge states of the material responsible for this current do not propagate in the opposite direction which means that these states are of chiral nature. Additionally, the probability of backscattering is suppressed and the edge states are robust to impurities, a fact that is not observed in the ordinary states of matter.

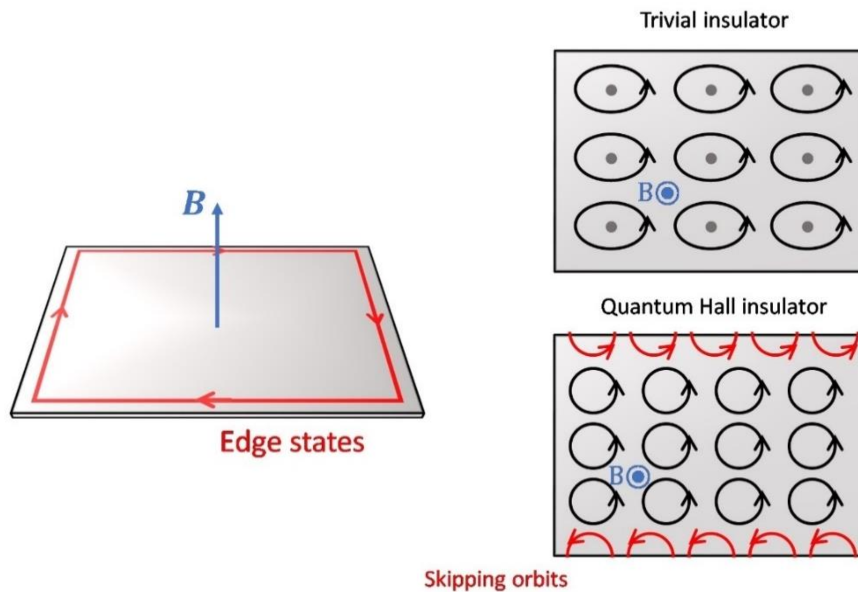

Figure 2.9: Quantum Hall effect. The presence of an external magnetic field induces conduction channels at the edges of the surface. Right side represents the contrast between the behavior of electrons in an ordinary insulator and in the quantum Hall effect. The insulator is characterized by a gap (Eg) that separates the occupied states (Valence Band VB) from the empty states (Conduction Band BC). In the quantum Hall effect, the circular orbit of electrons is interrupted at the edges, where the carriers conduct without dissipation.

The properties of such edge states were the first evidence of topological phases of matter. Indeed, in 1980 Klaus von Klitzing showed that Hall conductivity σ_{xy} is quantized in units of e^2/h (e is the electron charge and h the Planck's constant) and independent of the dimensions of the material studied. Two years later, Thouless, Kohmoto, Nightingale and Nijs showed that the quantum number that characterizes this system is in fact a non-zero Chern number, defining the material as topologically non-trivial [39]. Since vacuum is considered a trivial insulator ($n = 0$), at the edge of the material exists an interface that separates two insulators with different Chern numbers, thus they are topologically distinct. Hence, as mentioned in previous sections, their Hamiltonians cannot be smoothly deformed into one another without modifying the band structure of the resulting system, namely closing the band gap. This is known as the bulk-boundary correspondence (figure 2.10). As a consequence, metallic edge states arrises at the interface connecting conduction and valence band, and these states are protected by the bulk topology.

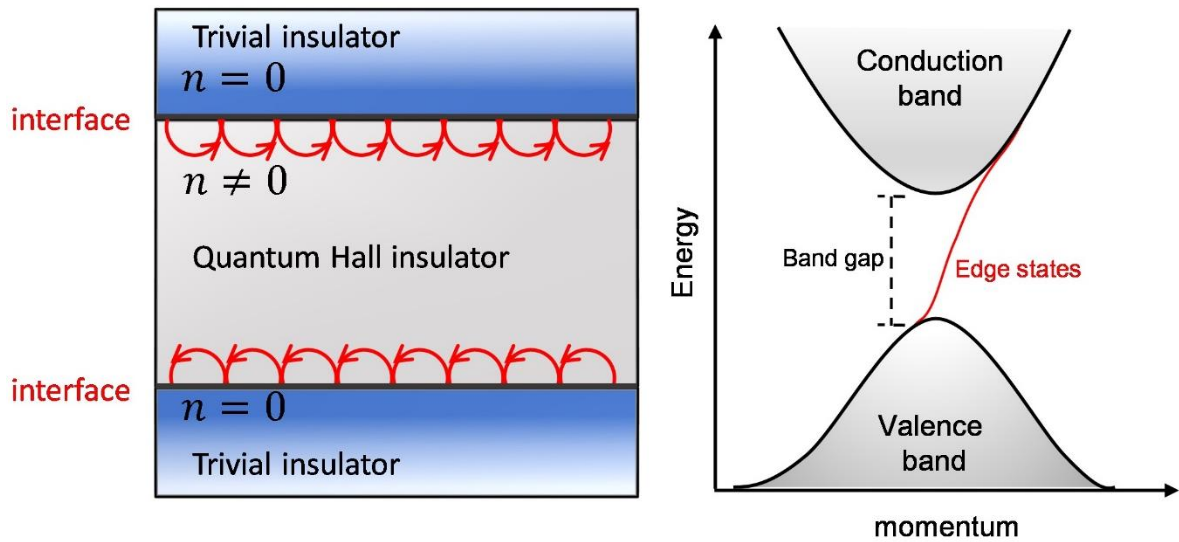

Figure 2.10: Bulk-Boundary correspondence between Quantum Hall insulator and trivial insulator (vacuum). At the interface their Hamiltonians cannot be smoothly deformed into one another without closing the band gap. As a consequence, in the band structure, states are observed (red line in the figure) that connect the valence band to the conduction band, passing through the bulk material gap.

2.2.3. Topological insulators

Although the Quantum Hall effect had been the first observation of the topological phases of matter, the presence of the applied magnetic field inevitably breaks the time-reversal symmetry (TRS) of the system. In this context, a natural question that arose at the time was whether such topological manifestations could emerge in more general systems without the presence of an external magnetic field. This question was answered by Kane and Mele who showed, in 2005, that the applied magnetic field can be replaced by a Spin-Orbit coupling (SOC), an intrinsic feature of all materials and more pronounced in heavy elements, preserving the TRS [36]. This model, known as Quantum Spin Hall insulator or two-dimensional (2D) topological insulator, represented the birth of topological insulators (TIs).

In a 2D topological insulators, topologically protected conductive edge states emerge as a consequence of strong spin-orbit coupling. Hence, differently from what was found in the quantum Hall effect, the Chern number in these materials is null since the time reversal symmetry is not broken. Based on this, eigenstates described by Hamiltonians that are time reversal invariant are inserted in another topological class, and consequently,

characterized by another topological invariant. Precisely, when a system exhibits time reversal symmetry its Hamiltonian $H(\boldsymbol{k})$, must satisfy

$$\Theta H(\boldsymbol{k})\Theta^{-1} = H(-\boldsymbol{k}), \tag{2.18}$$

where Θ is the time reversal symmetry operator. All Hamiltonians that are adiabatically connected so that equation 2.18 is satisfied without closing the gap are included in the same class, establishing the $\mathbb{Z}_2$ topological invariant ν [40].

Although the mathematical calculation of the $\mathbb{Z}_2$ invariant is complicated and beyond the scope of this thesis, the origin of this quantity can be understood based on the effect that the time reversal operator has on Dirac fermions characterized by half-integer spin. From quantum mechanics, Θ is an antiunitary operator given by

$$\Theta = \mathrm{e}^{\pi \mathrm{i} S_y/\hbar} K, \tag{2.19}$$

where S_y is the y component of the spin operator and K is a complex conjugation. Regarding spin 1/2 particles, equation 2.19 has the property $\Theta^2 = -1$. This property results in an important constraint on the eigenstates of the system known as Kramers' theorem, which states that any eigenstate that is time-reversal invariant and the total angular momentum is half-integer, will be at least two-fold degenerate [40]. When the system has no spin-orbit interaction, Kramers degeneracy refers to only the degeneracy between the up and down components of the spin. However, when this interaction is considered the band structure of the system splits and become degenerate, that is, the bands come in pairs $\boldsymbol{k}$ and $-\boldsymbol{k}$, called Kramers pairs, with opposite spin and displaying non-trivial topological properties.

The consequences of Kramers degeneracy are evidenced by observing the bulk-boundary correspondence in a 2D material invariant under TRS. Figure 2.11 represents two possible band structures at the edges of a 2D material as a function of the momentum along the edge. The finite energy gap between the conduction and valence band characterizes the insulator behavior in the bulk. Nevertheless, depending on the spectrum of $H(\boldsymbol{k})$ near the edges of the material, there may be states residing within the bandgap. When these edge states are present, they are doubly degenerate (Kramers pairs) at specific points in the Brillouin zone where time reversal symmetry is preserved. Due to spin-orbit interaction only

some discrete values of $\boldsymbol{k}$, denominated time-reversal invariant momentum (TRIM), satisfy equation 2.18. These points are designated by Γ_a and Γ_b in figure 2.11 and far from these points SOC lifts the degeneracy and the spins are decoupled, carriers with opposite spin move in opposite direction (helical property).

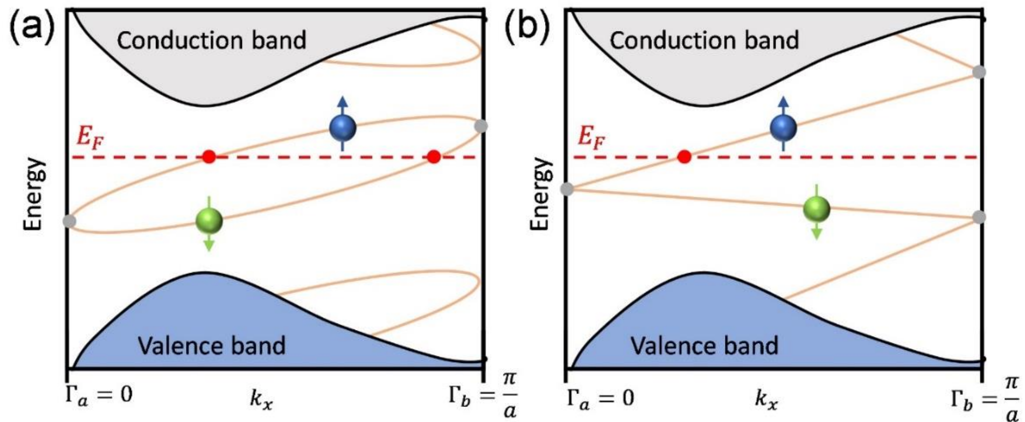

Figure 2.11: Two possible band structures at the edges of a 2D material as a function of the momentum along the edge. (a) Even number of edge states crossing E_F results in a trivial insulator. (b) Odd number of edge states crossing E_F, this implies robustness against small perturbations because there will be inter ligaments accessible to these states between the valence and conduction bands. The gray points represent the TRIM points within de Brillouin zone and only half of the Brillouin zone ($0 < k_x < \pi/a$) is show because TRS requires that the other half ($-\pi/a < k_x < 0$) is a mirror image. The figure is adapted from Ref. [40].

There are only two ways for edge states to connect between TRIM points in order to satisfy Kramers' theorem. They connect pairwise with other degeneracy points, forming a closed path, as shown in figure 2.11(a). In this case, shifting the Fermi level, e.g, with doping, it is possible to reach regions where there are no states in the band gap, thus these states can be eliminated by perturbations or disorders placing them outside the energy gap, the material is effectivelly band gapped and, consequently, topological trivial. This occurs when the Fermi level crosses the edge states an even number of times between the states $k_x = 0$ and π/a. However, if the Fermi level intersects the states residing in the bulk gap of the material an odd number of times, as shown in figure 2.11(b), these states are said to be topologically protected. In this situation, the edge states connect between the TRIM points switching pairs in a zig zag fashion and, regardless of the Fermi level position along the gap, they will always have intercepted states. These edge states continuously connect bulk valence and conduction bands and cannot be eliminated by perturbations.

It is the topology of the bulk that defines which of the two possibilities mentioned above occurs. The $\mathbb{Z}_2$ invariant denotes the topological classification based on parity [36], assuming only the values 0 or 1. Formally, each band crossing the Fermi energy at k_x has its degenerate Krammers partner at $-k_x$, the bulk-boundary correspondence relates the number of Krammers partners N_K crossing the E_F at the edge of the material, with the change of the $\mathbb{Z}_2$ invariant $\Delta\nu$ across the interface [40].

$$N_K = \Delta\nu \text{mod} 2. \tag{2.20}$$

In this equation, mod2 = 0 (1) means even (odd) parity. Hence, if the insulator has even N_K ($\nu = 0$), it is defined as topologically trivial and if N_K is odd ($\nu = 1$) it is said to be topologically non-trivial. In this context, at the edges of a two-dimensional topological insulator the same reasoning discussed in the previous section can be applied. The existence of edge states is associated with a change in the topological invariant at the interface between a common insulator and TI (figure 2.12). These states are robust against disorders, precisely because they are protected by the bulk topology, only disorders of magnetic origin can break the TRS. Furthermore, unlike what was observed in quantum Hall effect, due to SOC, the edge states separate into different conduction channels depending on the spin orientation, often referred to as spin-momentum locking.

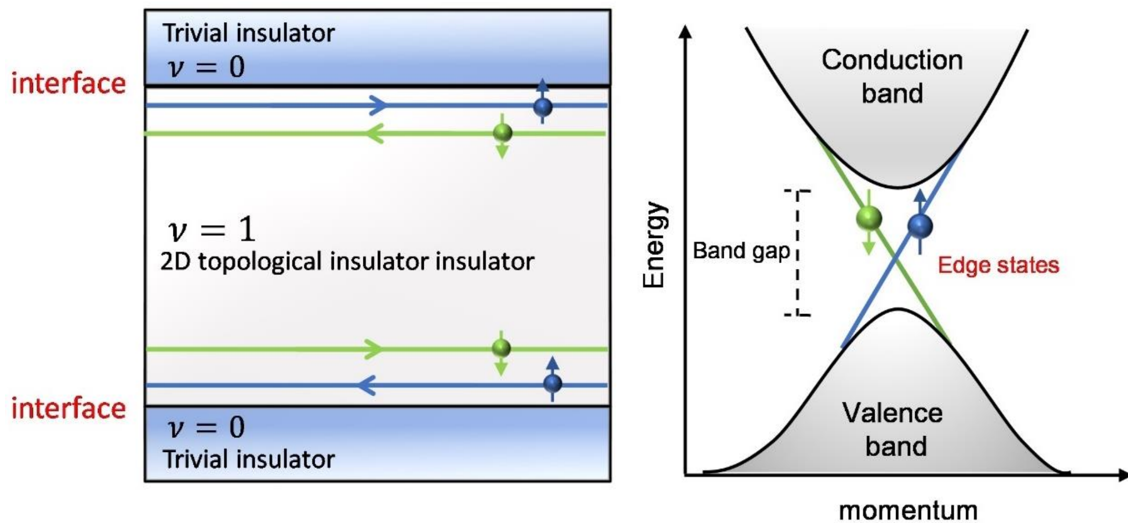

Figure 2.12: Bulk-Boundary correspondence between 2D topological insulator and trivial insulator (vacuum). The existence of edge states such that carriers with opposite spin move in opposite direction is associated with a change in the topological invariant at the interface. Consequently, in the band structure, two states with opposite spins are observed (blue and green lines in the figure) that connect the valence band to the conduction band, passing through the bulk gap.

The first experimental evidence of two-dimensional topological insulators was observed in a heterostructure of CdTe-HgTe in 2006 by Konig *et al*. As shown in figure 2.13, this structure consists of a thin layer of HgTe sandwiched between two layers of CdTe, the topological states were observed in quantum wells at the edges of these interfaces. Similar to other semiconductors, the conduction band of CdTe have s-type symmetry, while the valence band, have p-type symmetry [41]. In HgTe, p levels reside above s levels. The orderings of the energy levels of the band structure of the respective compounds are shown in figure 2.13(a).

When the thickness (d) of the HgTe film is below the critical value, $d_c \approx 6.5\ nm$, the energy bands show a normal ordering. However, for $d > d_c$, the bands and consequently the subbands in the quantum well structure are inverted, and the separation between these is a function of d. Such situations are illustrated in figure 2.13(a). At $d = d_c$, these bands cross closing the band gap, which implies the existence of metallic edge states protected by TRS, as shown in figure 2.13(b). This parity inversion is responsible for the quantum phase transition between a trivial insulator and a 2D topological insulator.

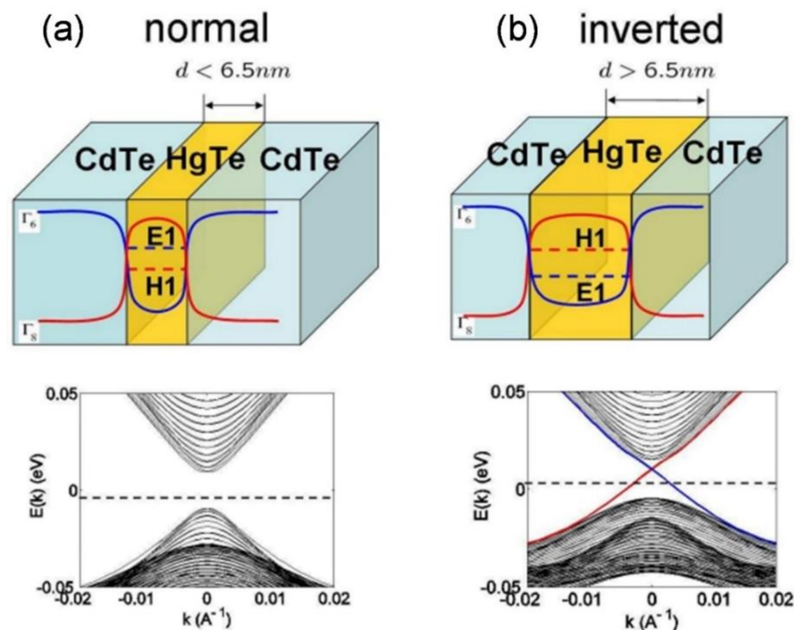

Figure 2.13: Experimental realization of 2D topological insulator. (a) For HgTe thickness below d_c the material behaves as a normal insulator with a bandgap between conduction and valence bands. (b) For HgTe thickness above d_c the inverted band structure results in edge states within the bandgap (blue and red line) connecting the conduction and valence bands [41].

Every theory discussed in the previous section can be extended to the case of three-dimensional topological insulators. In these materials, the non-trivial topology of the bulk results in gaplesss surface states rather than edge states. Formally, these materials are characterized by four $\mathbb{Z}_2$ invariants $(\nu_0; \nu_1\ \nu_2\ \nu_3)$ due to the number of TRIM points within the 3D Brillouin zone of a crystal, where kramers degeneracy occurs [40]. However, only ν_0 defines the topological class, whereas the invariants $(\nu_1\ \nu_2\ \nu_3)$ define the orientation of the projected studied surface, definng time-reversal invariant planes, like Miller's indices in crystallography (figure 2.14(a)).

In the same way as in the 2D case, whether the material is an ordinary or a topological insulator then depends on how different TRIM points connect to each other. The Fermi surface of the material can surround an odd or even number of these points within it. When an even number of TRIM points are enclosed, the material has $\nu_0 = 0$. In this case, two possibilities may occur. If along the gap there are no states, the material is a trivial insulator. However, if states are observed, the material is a weak topological insulator. These states are not robust even for non-magnetic disorders. This situation is represented in figure 2.14(b)[40].

Otherwise, when the Fermi surface encloses an odd number of TRIM points, the material has $\nu_0 = 1$, and exhibits a non-trivial topological phase, defing a strong topological insulator [40]. In this material, the surface states are protected by time-reversal symmetry and form a unique 2D topological metal [40]. In the simplest configuration, only one projected TRIM at the Brillouin zone center is enclosed by the Fermi surface. Since time-reversal symmetry requires that states at momenta $-\boldsymbol{k}$ and $\boldsymbol{k}$ have opposite spin, the momentum vector is able to completely surround the Fermi surface as long as the spin vector rotates simultaneously [40], as shown in figure 2.14(c).

These surface states support electronic motion in any direction along the surface, however, the spin-momentum locking is still observed with the orientation of the spin coupled to the direction of motion, consequently spin and momentum are perpendicular to each other (helical property). This leads to a prohibition on backscaterring and a reduction in

scattering at other angles from nonmagnetic perturbation, vacancies, and other defects, since a change in momentum requires a change in spin [40].

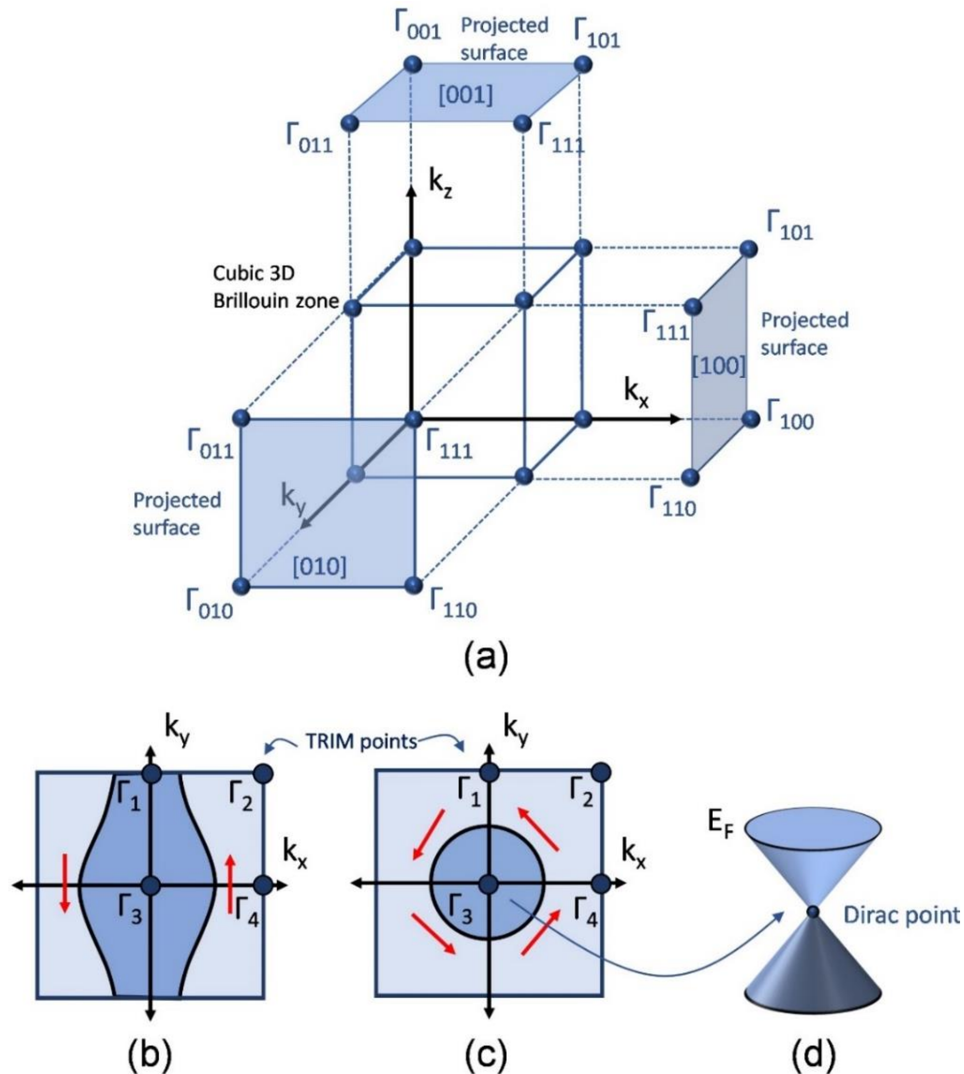

Figure 2.14: (a) Example of a 3D Brillouin zone for a cubic symmetry showing the two-dimensional projected surfaces where the parity of the TRIM points (Γ_i) is evaluated. (b) Even number of TRIMs encompassed by the Fermi surface. (c) Odd number of TRIMs encompassed by the Fermi surface resulting in a strong topological insulator. (d) Dirac cone representing the 2D surface states within the bandgap of a 3D topological insulator. The figure is adapted from Ref. [39].

In the 3D band structure of this materials, under a variation of the Fermi surface along the energy scale, a linear dispersion with respect to momentum is observed and the so-called surface Dirac-cone is drawn connecting valence and conduction band, whereas degeneracy is only present at the intersection point k = 0 of spin up and spin down states

(see figure 2.14(d)). This point is called Dirac-point. The Dirac nomenclature has its origin in the similarity of the dynamics of surface states with the quantum theory for massless relativistic particles that are governed by the Dirac equation [39-41].

The first experimental evidence of surface states in 3D materials was made through studies on $Bi_{1-x}Sb_x$ alloys. In 2008 Hsieh *et al.* showed that for certain concentrations of antimony, the strong SOC results in a band inversion at specific points in the Brillouin zone, with Angle Resolved Photoemission Spectroscopy (ARPES) technique the surface states could be detected. However, $Bi_{1-x}Sb_x$ alloys have a complex band structure and small gap ($\sim$ 300 meV), which makes a deeper study of the surface states in these structures difficult.

The state of the art of 3D topological insulators practically began with the theoretical prediction and later experimental verification that stoichiometric compounds of group V-VI chalcogenide semiconductors exhibit topological properties at room temperature. Bi_2Te_3, Bi_2Se_3 and Sb_2Te_3 have a simpler band structure than $Bi_{1-x}Sb_x$ alloys with a bandgap of the order of a few hundred meV (up to 300 meV in Bi_2Se_3). Since SOC lifts the degeneracy in the l orbital quantum number, this effect is more pronounced for p ($l = 1$) and d ($l = 2$) orbitals and is negligible for s orbitals since $l = 0$. As in a typical semiconductor, the valence and conduction bands are associated with the p and s orbitals, respectively. Due to the strong SOC the p orbital can be pulled in energy above the s orbital resulting in a band inversion at the center of the Brillouin zone. This property assigns non-trivial topological characteristics to these materials ($\nu_0 = 1$) and, consequently, conductive states are observed on the surface. Figure 2.15(a) shows the band structure for group $\mathrm{V_2}$-$\mathrm{VI_3}$ obtained by first principles calculations [42]. The characteristic linear dispersion of conductive states connecting the valence and conduction bands can be observed across the bandgap. Panel (b) shows the effect of SOC on the band structure of Bi_2Se_3, only in the presence of SOC is observed the inversion of bands that originate the surface states. Finally, in panel (c) an ARPES measurement for Bi_2Se_3 is shown, the single Dirac cone at the gamma point is observed experimentally.

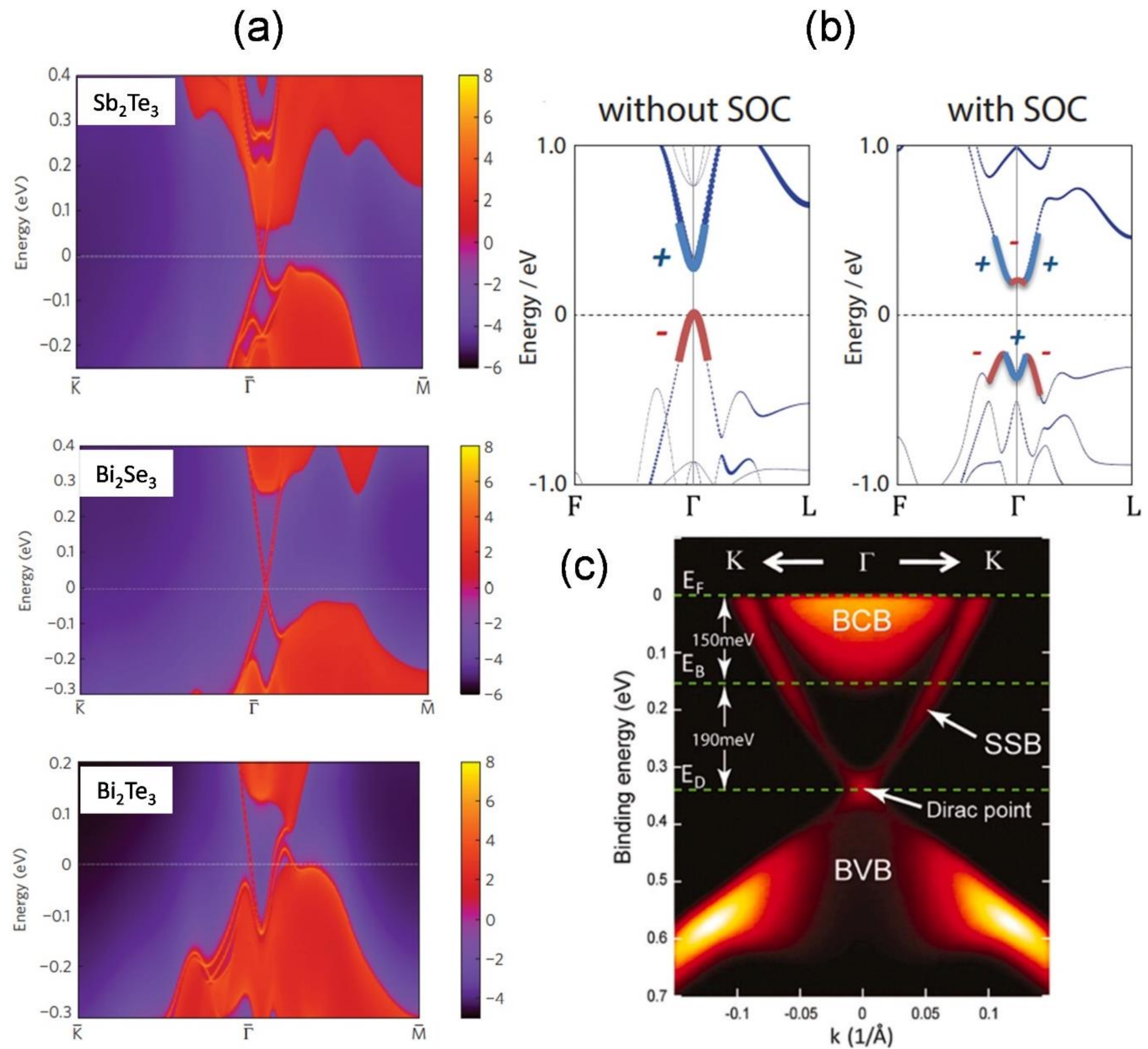

Figure 2.15: (a) The band structure for group V_2-VI_3 obtained by first principles calculations showing the linear dispersion of the surface states in these materials. (b) Effect of SOC on the band structure of Bi_2Te_3, the strong SOC causes the valence band states to be pushed higher in energy than the conduction band states, leading to a parity inversion between them. (c) ARPES measurement showing the presence of surface states within the bulk band gap for a Bi_2Se_3 crystal. The figure is adapted from Refs. [39-42]

2.2.3.1 Magnetic impurities

As discussed in the previous sections, the main characteristic of topological insulating materials is the presence of edge/surface states that are protected by the bulk topology, and therefore, insensitive to non magnetic disorder. In these materials, electric current can flow without dissipation since backscattering is inhibited by time-reversal symmetry. This fact can

be seen in figure 2.16(a), where the two situations that can occur when charge carriers encounter defects are represented.

For electrons that propagate from left to right with spin up, the impurity can be bypassed either clockwise or counterclockwise. If the first case occurs, the electron spin rotates by an angle of π to the opposite direction. On the other hand, in the second situation a counterclockwise contour results in a rotation of $-\pi$ in the electron spin. In both situations the electron ends up at the backward state with inverted spin and, consequently, the two situations differ from a full rotation of 2π in the electron spin.

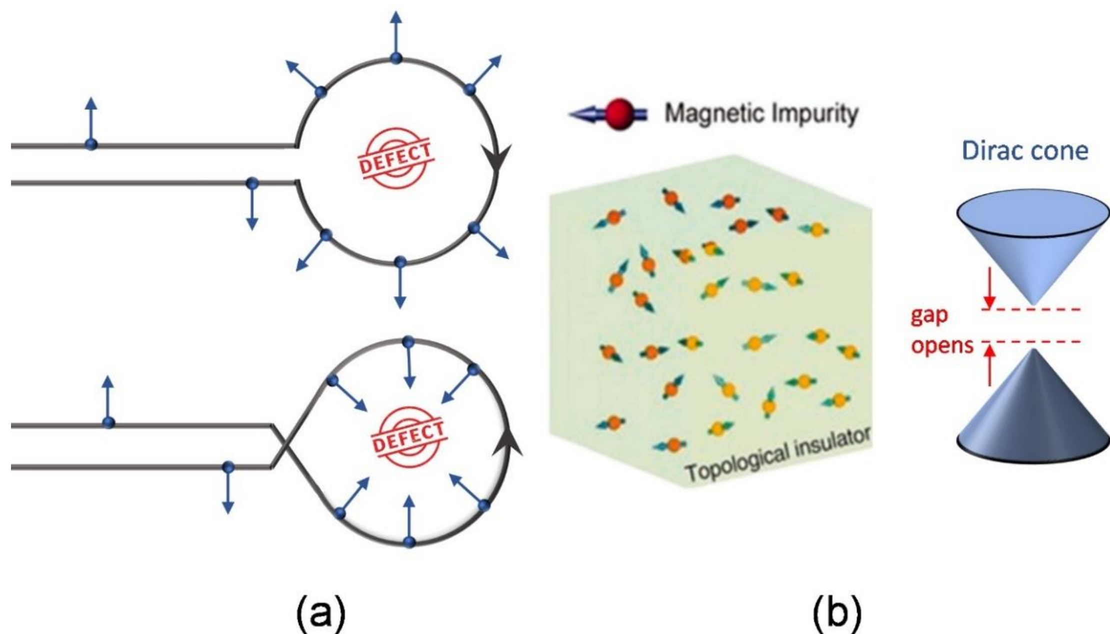

Figure 2.16: (a) Two possible paths for the electron to bypass a non-magnetic impurity in a topological insulator. (b) Theoretical prediction for the opening of the Dirac cone due to the presence of impurities that violate the time reversal symmetry. The figure is adapted from Ref. [43].

In the field of quantum mechanics, it is known that the wavefunction of spin 1/2 fermions acquires a negative sign under rotations of 2π [43]. Then, regardless of the path taken by the electron around a defect, destructive interference will always occur so that the backscattering is nullified enabling perfect transmission. However, if this defect is magnetic or the topological insulator is subjected to an external magnetic field, the time-reversal symmetry is broken and, in principle, the robustness of the edge/surface states is affected.

A gap can be opened in the Dirac cone, lifting the Kramers degeneracy and giving rise to massive fermions allowing backscattering processes, as represented in figure 2.16(b).

The influence of magnetic impurities is still an open question in the analysis of topological insulators. There are different studies where, for example, Bi_2Te_3 and Bi_2Se_3 were doped with magnetic atoms both in the bulk and on the surface. Many of these works report the opening of the gap in the Dirac cone with the increase of the concentration of magnetic impurities, however many other works indicate that even with a considerable concentration of magnetic atoms in the structure of the TI the Dirac cone remains preserved.

Chen *et al* showed that in Fe-doped Bi_2Se_3 crystals it is possible to observe the gap opening in the dirac cone for Fe concentrations greater than 10% [44]. ARPES measurements showed that for samples doped with 12% and 16% Fe a gap of the order of 44 meV and 50 meV, respectively, was observed. Morever, Kou *et al* shows that the bandgap os Bi_2Se_3 surface is open and monotonically increases with Cr concentration up to 100 meV, as shown in figure 2.17 [45]. This confirms the theoretical prediction that magnetic impurities affect surface states due to TRS breakdown.

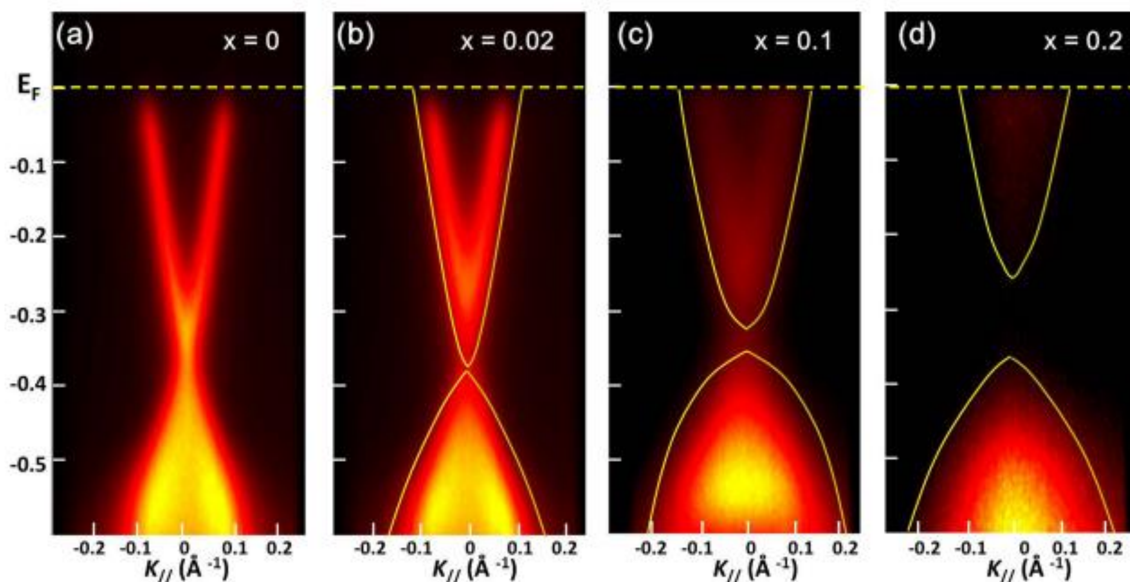

Figure 2.17: ARPES measurement in the vicinity of Γ point showing the monotonic opening of the band gap of surface states with increasing Cr concentration in Bi_2Se_3 films. The figure is taken from Ref. [45].

On the other hand, SCHOLZ *et al* [46] and Fornari *et al* [47] studied Bi_2Te_3 doped with Fe and Eu respectively, and did not observe gap opening. These results are shown in figure 2.18, where it is possible to observe the preserved Dirac cone. A greater understanding of the interaction between surface states and magnetic impurities is essential for device development based on TI materials. For example, eliminating a spin channel on the surface results in a fully polarized current, an excellent alternative for application in spin transistors [43]. Furthermore, the interface between a TI and a magnetic material can offer an interesting platform for studying the phenomenon of superconductivity [44].

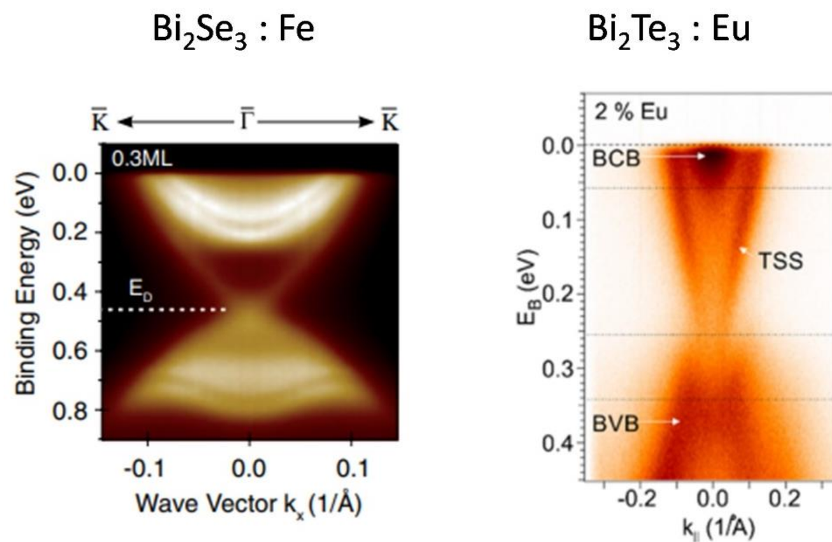

Figure 2.18: ARPES measurement in the vicinity of Γ point of the Bi_2Se_3 and Bi_2Te_3 films doping with Fe and Eu, respectively. Both figures show an intact Dirac cone, indicating the presence of surface states even with magnetic-type impurities. Imagens taken from [46, 47].

3. Materials

3.1. Silicon-Germanium alloy

The advancement of technology from the development of semiconductor devices is evident. It is possible to say that all this progress is based on the Germanium (Ge) and Silicon (Si) elements since they represent the core of the entire microelectronics industry. The former was the material used for the development of the first transistor in 1947 [1]. The second, due to its excellent natural properties and ease of growth/deposition, quickly became to dominate the electronic devices market [2].

Over the years, the performance of CMOS (Complementary Metal-Oxide Semiconductor) devices, which have Si as a raw material, has been improved through the miniaturization process of all components of the so-called integrated circuits (ICs). However, the reduction in size and increase in the operating frequency is reaching the limits of the integrity of the physical properties of the materials, resulting in undesirable effects such as excessive leakage currents, parasitic capacitance and high energy consumption [48].

In this context, new materials compatible with CMOS technology are being studied in order to improve the performance of devices. A candidate for this position is biaxially strained Silicon (sSi). In this material, the initially cubic structure of Si is tetragonally distorted, resulting in an improvement in the electronic properties since it has a greater mobility for both electrons and holes [49-52]. The increase in electron mobility in the sSi occurs due to the decrease in its effective mass and the decrease in scattering events in the valleys of the conduction band [49]. Thus, compared to Si, sSi requires a lower electric field value to generate the same carrier speed, dissipating less power. In addition, the sSi channel MOSFET (Metal-Oxide-Semiconductor Field Effect Transistor) device, main component of the electronics industry today, present higher values of saturation current in the drain and are faster.

Currently there are some methods for obtaining high quality sSi. The most common method for obtaining sSi-based devices is the heteroepitaxial growth of Si on a

substrate containing a layer of SiGe, called virtual substrate [4]. In this kind of heterostructures silicon becomes biaxially strained due to its lattice parameter being smaller than that of SiGe alloy. Based on this, the study and growth of SiGe layers with high crystalline quality is extremely important. Furthermore, Silicon Germanium alloy does not face any process compatibility issues, offering easy integration with current transistor production technology. This alloy combines the thermal stability of Si with the low resistivity of Ge in order to offer a material with great advantages and easy integration into the device production process.

3.1.1. Properties of SiGe alloy

Both Silicon and Germanium are semiconductors materials that belongs to group IV of the periodic table and crystallize following a diamond-like cubic structure, represented in figure 3.1. This structure consists of two interpenetrated face-centered cubic lattices and displaced, relative to each other, by a quarter of the cube's diagonal by a vector $\boldsymbol{r} = \frac{a}{4}\hat{x} + \frac{a}{4}\hat{y} + \frac{a}{4}\hat{z}$, where a is the lattice parameter of the material. For Si lattice constant are 5.430 Å whereas for Ge the value is 5.658 Å.

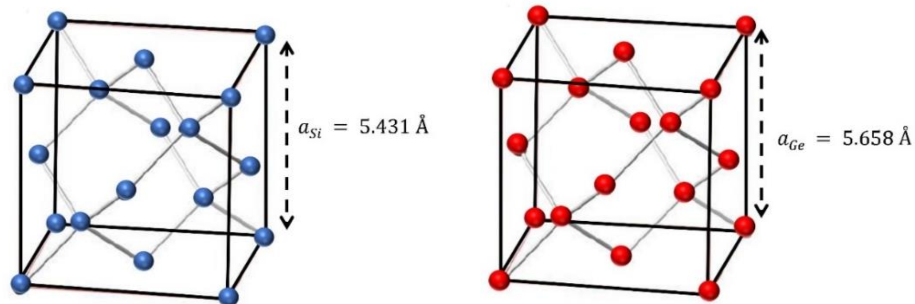

Figure 3.1: Cubic crystal structure of Si (left) and Ge (right), respectively.

Since Si and Ge are completely miscible, the $Si_{1-x}Ge_x$ alloy is of the substitutional type, resulting in liquid and solid stable phases over the entire composition range. Its structure is obtained by the random substitution of Si (Ge) atoms for Ge (Si) atoms while the diamond crystal lattice is preserved. For a given mole fraction x, the number of atoms (N) obeys the following rule [53]:

$$x = \frac{N_{Ge}}{N_{Ge}+N_{Si}} \tag{3.1}$$

The equilibrium phase diagram of the SiGe system is represented in figure 3.2. As can be seen, this alloy is characterized by a wide range of liquid-solid coexistence. Furthermore, an increase in Ge concentration results in a decrease in the melting point. These two properties are important factors to consider when growing SiGe crystals and in the development of heterostructures devices [54, 55].

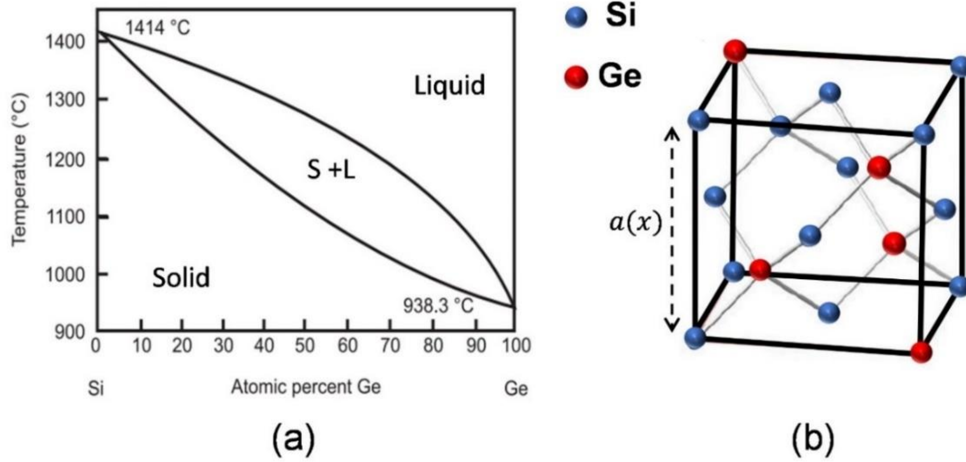

Figure 3.2: (a) Phase diagram of SiGe alloy as a function of Ge concentration. (b) Crystal structure of the SiGe alloy in stable solid phase, the lattice constant $a(x)$ of relaxed SiGe is almost linearly depending on the alloy composition x. The figure is adapted from Ref. [55].

The crystal structure of the SiGe alloy in stable solid phase is schematically represented in figure 3.2(b). Although some variations have been observed, the lattice constant of relaxed SiGe is almost linearly depending on the alloy composition x and can be obtained from the lattice parameters of its constituents according to Vegard's Law [52]:

$$a(x)_{SiGe} = (1-x)a_{Si} + xa_{Ge}. \tag{3.2}$$

Another characteristic of the SiGe alloy is its electronic structure, intermediate to that of its components (figure 3.3). Both Si and Ge are characterized by an indirect bandgap, since the minimum of the conduction band and the maximum of the valence band are located at different points in the Brillouin zone. Although, they have different bandgap energy $E_g^{Si} = 1.11\,eV$ and $E_g^{Ge} = 0.66\,eV$ (Ge bandgap is half of Si bandgap) this two materials have very similar electron affinities (distance between the vacuum level and the conduction band), consequently in the alloy the relative positions of

the conduction band and, mainly, of valence band can be adjusted between the two extremes (pure Si and pure Ge). In this way, one can make use of the Work Function Engineering, that is, one can vary the level of the bandwidth valence up to 400 mV, just controlling the amount of Ge in the alloy [56], which can particularly benefit p-MOS devices.

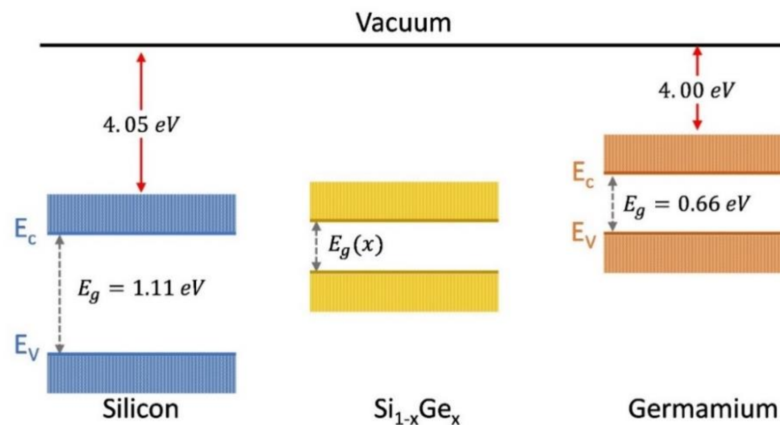

Figure 3.3: Schematic representation of SiGe band structure intermediary between the Si and Ge band structure. The energy band gap can be controlled through the concentration of Ge in the alloy. The figure is adapted from Ref. [56].

3.1.2. SiGe heteroepitaxy

As discussed in section 3.1, the growth of SiGe structures with high crystalline quality and controlled composition is important since it can be used as a substrate for the growth of strained Si. Besides that, most SiGe applications are made using its single-crystalline phase. In this context, SiGe/Si heterostructures can be grown by different epitaxy techniques, such as molecular beam epitaxy (MBE) and chemical vapor deposition (CVD) [57, 58]. With these techniques it is possible to grow epitaxial layers with controllable thickness and Ge composition. The possibility of strain engineering and the consequently improved electrical properties, mainly concerning carrier mobility and resistivity, had lead to several forms of fabrication of micro/nano-electronic devices through heteroepitaxy growth on Si or SOI (Silicon-On-Insulator) substrates.

Due to the 4.2% difference in the lattice parameter of Ge with relation to Si, the epitaxy of SiGe on top of a Si substrate (heteroepitaxy) can generate layers defined as pseudomorphic or relaxed, as discussed in chapter 2. In a pseudomorphic growth, since the

lattice parameter of the alloy can be obtained to a first approximation by Vegard's law (eq 3.2), for any non-zero Ge concentration value, the initially cubic structure of the SiGe system is tetragonally distorted due to compressive strain associated with the fact that $a_{SiGe} > a_{Si}$ (figure 3.4(a)). In this situation, the in-plane lattice parameter ($a_{||}$) will be the same as that of Si. The perpendicular component can be obtained with good approximation by the elastic theory [59], being equal to:

$$a_{\perp} = a(x) + 2\frac{c_{12}^{SiGe}}{c_{11}^{SiGe}}(a(x) - a_{||}), \tag{3.3}$$

where $a(x)$ is the SiGe relaxed lattice parameter, C_{11} and C_{12} are the elastic constants of the alloy, whose values can be obtained from the relationship [52]:

$$c_{ij}^{SiGe} = (1 - x)c_{ij}^{Si} + xc_{ij}^{Ge}, \tag{3.4}$$

where C_{ij}^{Si} and C_{ij}^{Ge} are the elastic constants of Si and Ge, respectively.

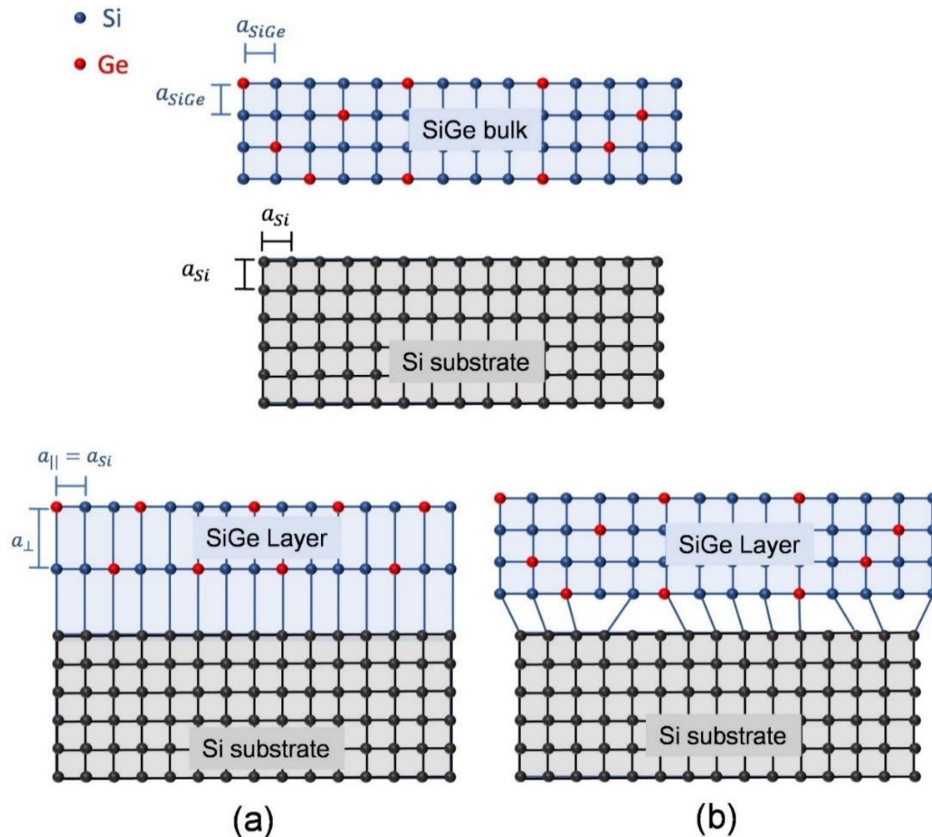

Figure 3.4: (a) Fully strained (pseudomorphic) SiGe layer deposited on a Si substrate, the initially cubic structure of the SiGe system is tetragonally distorted due to compressive strain. (b) Relaxed SiGe layer with a non-coincident interface. The presence of interface defects is not a desired characteristic for the manufacture of electronic devices, especially when dealing with transistors.

The elastic energy accumulated in the pseudomorphic SiGe layer increases with increasing layer thickness and also with the concentration of Ge. For a given concentration of Ge, there is a thickness, called critical thickness, beyond which the elastic energy can no longer be compensated through pseudomorphic growth. From this thickness, the layer begins to relax through the formation of defects in the SiGe-Si interface, as illustrated in figure 3.4(b).

The presence of interface defects is not a desired characteristic for the manufacture of electronic devices, especially when dealing with transistors, as the defects act as traps and/or scattering centers, reducing carrier mobility. Thus, the growth of pseudomorphic layers is desirable for the fabrication of heterostructures. In addition to the absence of defects, the strain present in the SiGe epitaxial layer can further reduce the alloy bandgap and increase carrier mobility. However, this pseudomorphic growth is limited by the concentration of Ge and the thickness of the alloy layer, facts that motivated the development of new growth methods, such as the Ge condensation technique discussed in Chapter 5. In this technique, the selective oxidation of the Silicon allows to obtain SiGe layers with good crystalline quality and high Germanium concentration [6, 48]. Table 3.1 lists the values of the main elastic constants of Si and Ge crystals.

Table 3.1: Lattice parameters and main elastic constants of Si and Ge materials.

Properties		Si	Ge
Lattice parameter (Å)		5.431	5.658
Elastic constant (GPa)	c11	165.8	128.5
	c12	63.9	48.3
	c44	79.6	66.8
Bulk modulus (GPa)	B	97.9	75.1
Shear modulus (GPa)	S	51.00	40.15
Young modulus (GPa)	Y	130.2	102.1
Poisson ratio (GPa)	ν	0.278	0.271

Source: Data taken from Ref. [60]

3.2. Bismuth Telluride

3.2.1. The Bi_xTe_y compound

The V-VI group chalcogenides are compounds that have been extensively studied in the field of thermoelectric materials. Within this group, bismuth telluride (Bi_2Te_3)

has received special attention from researchers over the years due to the fact that it has the highest electricity-to-heat conversion coefficient [61], a fact that enabled the development of high-performance thermoelectric devices at room temperature [62, 63]. However, the recent discoveries of the presence of topologically protected surface states in this compound, represented a new search for the synthesis of Bi_2Te_3 crystals with high structural quality and accurate stoichiometry.

The growth of crystals with the correct stoichiometry is extremely complicated in this material, since, contrary to what is observed in more common binary semiconductors (compounds of families III-V and II-VI) whose crystal structure is formed in stoichiometry 1:1, in Bismuth Telluride there is the development of multiple phases with different chemical compositions, denoted Bi_xTe_y, which are directly related to the growth conditions [64, 65]. In practice, the Bi_xTe_y compound establishes a homologous series of crystalline structures where the occurrence of two fundamental atomic sets is observed in each phase, as shown schematically in figure 3.5. In the first set, denoted in blue, the atoms are arranged in a sequence of the type: $Te^{(1)}$-Bi-$Te^{(2)}$-Bi-$Te^{(1)}$ constituting a quintuple layer (QL). The second set, denoted in pink, is a bismuth bilayer (BL) with a sequence of Bi-Bi-type atomic planes.

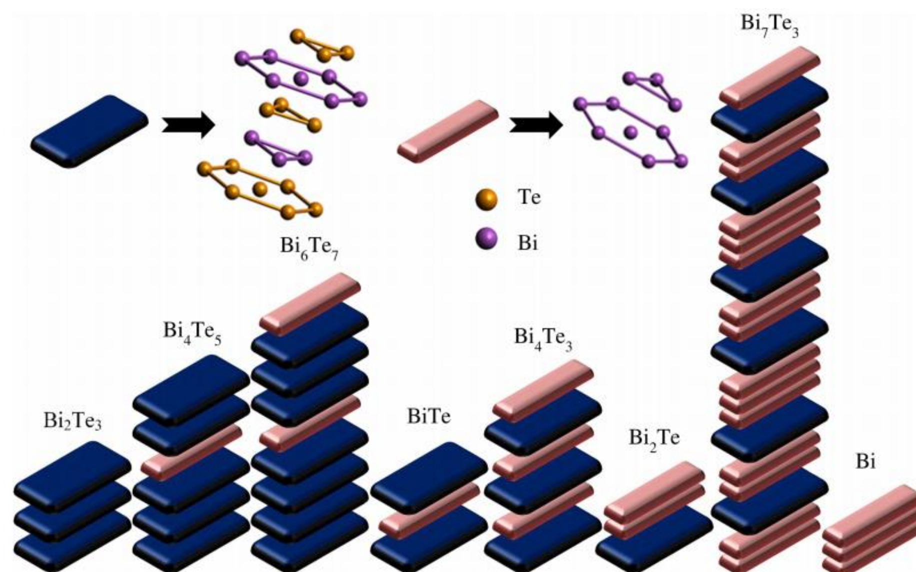

Figure 3.5: Schematic representation of the different phases of the BixTey compound. The fundamental sets of quintuple layers are represented by the blue colored blocks and the bismuth double layers are represented by the pink colored blocks. The unit cell for each of the above compounds consists of the repeat set of stacked layers shown for each stoichiometry. Figure adapted from reference [65]

By constituting a homologous series, all phases of Bismuth telluride share similarities in crystal structure. It is possible to represent all phases in the hexagonal system with in-plane lattice parameter a and out-of-plane lattice parameter c. Table 3.2 shows the values of a and c for the different phases of this compound. It is worth mentioning that it is in the Bi_2Te_3 phase that the states of surfaces are observed, therefore, this is the phase said to be topological insulator.

Table 3.2: Different phases that define the homologous series of the Bi_xTe_y compound with the respective in-plane (a) and out-of-plane (c) lattice parameter values.

Bi_xTe_y	a (Å)	c (Å)
Bi_2Te_3	4.395	30.440
Bi_4Te_5	4.415	54.742
Bi_6Te_7	4.424	79.011
Bi_8Te_9	4.425	103.279
Bi_1Te_1	4.433	24.269
Bi_4Te_3	4.444	42.332
Bi_2Te_1	4.465	18.064
Bi_7Te_3	4.472	120.241
Bi	4.545	11.859

Source: Adapted from reference [64].

3.2.2. The Bi_2Te_3 phase

3.2.2.1. Crystalline structure

From a theoretical point of view, the electronic properties of Bi_2Te_3 are closely related to the topology of the crystal structure as well as the strong spin-orbit coupling present in this compound. Formally, Bi_2Te_3 is a binary compound that has a rhombohedral structure belonging to the $D_{3d}^5(R\overline{3}m)$ space group with 5 atoms per unit cell. However, as already mentioned, this structure can be represented in terms of a unit cell with hexagonal symmetry obtained by stacking three quintuple layers (QLs) along the z-axis. The rhombohedral and hexagonal structures are represented in figure 3.6.

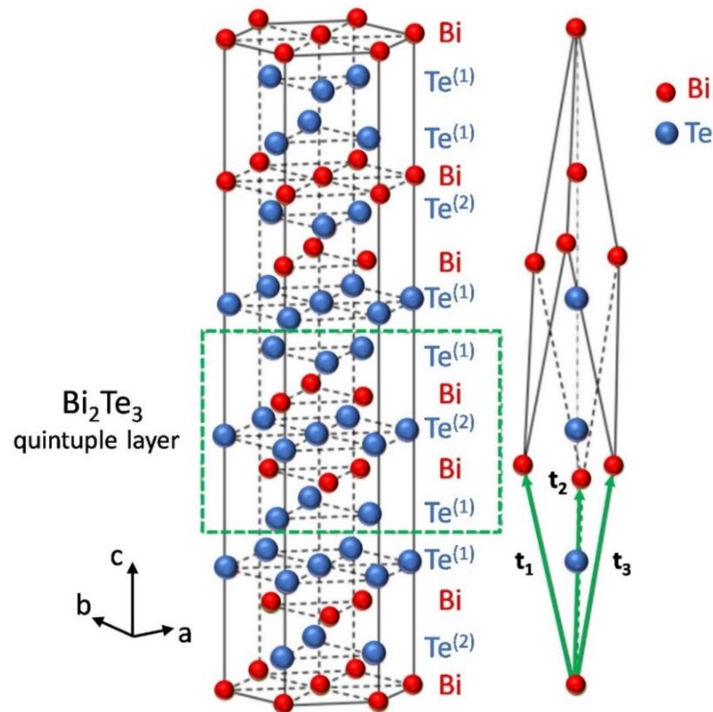

Figure 3.6: Crystal structure of the Bi_2Te_3 phase. The rhombohedral unit cell is highlighted and defined by the set of vectors $\mathbf{t}_1$, $\mathbf{t}_2$ and $\mathbf{t}_3$. Also represented is the alternative definition in terms of a unit cell with hexagonal symmetry obtained by stacking fivefold layers. Adapted from reference [19]

The entire crystalline structure of bismuth telluride can be constructed through linear combinations of the lattice vectors, indicated in figure 3.6 as $\boldsymbol{t}_1, \boldsymbol{t}_2$and $\boldsymbol{t}_3$. These vectors can be written in the form [19]:

$$\boldsymbol{t}_1 = \left(-\frac{a}{2}, -\frac{\sqrt{3}a}{6}, \frac{c}{3}\right), \boldsymbol{t}_2 = \left(\frac{a}{2}, -\frac{\sqrt{3}a}{6}, \frac{c}{3}\right), \boldsymbol{t}_3 = \left(0, \frac{\sqrt{3}a}{3}, \frac{c}{3}\right), \quad (3.5)$$

where a and c are the in-plane and out-of-plane lattice parameters whose values are indicated in table 3.2.

Due to its simplicity, the hexagonal cell is the most used. Figure 3.7 details the stacking process of the atomic planes that form the hexagonal crystal lattice of Bi_2Te_3. As the stacking sequence is of the ABCABC type... there is a set of three fundamental atomic planes where only the chemical element (Te or Bi) is altered, the first being formed by Te atoms, with a distance between atoms equal to that of the in-plane lattice parameter lattice a, with an atom centered at the origin of the lattice, as shown in figure 3.7(a). The second atomic plane is composed of Bi, having the origin shifted 2/3 a along the $[1\bar{1}00]$ direction and $\frac{1}{3}a$ in

the $[\bar{1}100]$ direction. In this plane, represented in figure 3.7(b), the spacing between the atoms is also a. The third atomic plane, detailed in figure 3.7(c), is again composed of Te atoms, originating at a distance of $\frac{1}{3}a$ in the $[1\bar{1}00]$ direction and $\frac{2}{3}a$ in the $[\bar{1}100]$ direction.

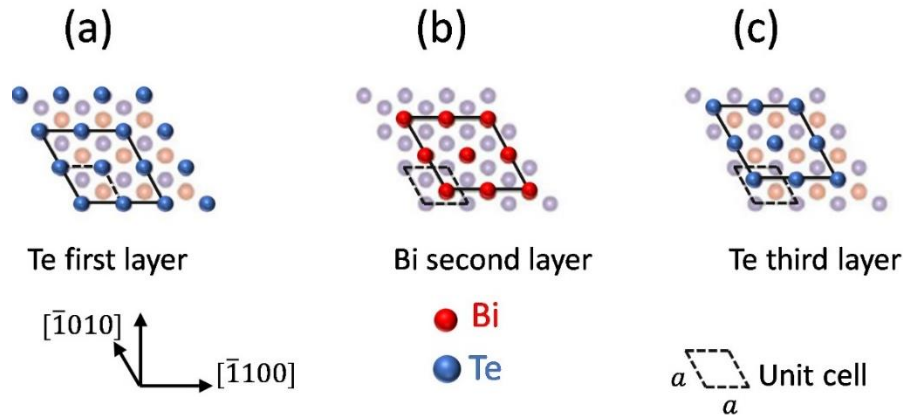

Figure 3.7: Representation of the ABC-type stacking sequence that constitutes the surface (001) of bismuth telluride. Two azimuths of symmetry are plotted in the xy cartesia plane. Taken from reference [66].

As schematically represented in figure 3.8, $Te^{(2)}$ atoms are positioned between two Bi layers, while $Te^{(1)}$ atoms have a Bi layer on one side and $Te^{(1)}$ on the other, thus the subscripts serve to distinguish the two types of sites at which the tellurium atom can be found. Adjacent quintuple layers have two atomic planes of tellurium, which are connected by weak van der Waals-type interactions. On the other hand, within each QLs the adjacent atomic planes of bismuth (Bi) and tellurium (Te) are then connected through strong covalent bonds. The presence of different chemical bonds introduces an anisotropic character in the crystalline structure of the Bi_2Te_3 phase, as in other layered materials (graphene, for example). The facility in the process of mechanical exfoliation of the material is precisely attributed to the rupture of the bonds between adjacent tellurium ($Te^{(1)}$-$Te^{(1)}$) planes.

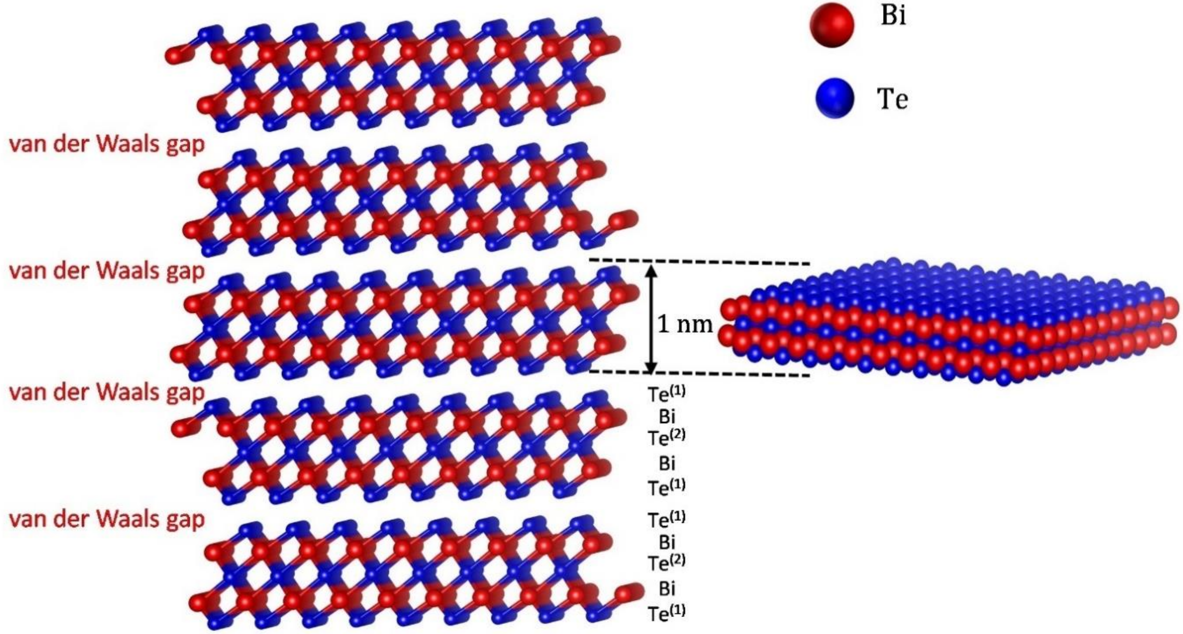

Figure 3.8*:* Detailed representation of the stacking sequence of the quintuple layers along the [001] direction, connected by van der Waals interactions. The height of a quintuple layer is approximately 1 nm.

3.2.2.2. Electronic structure

From the lattice vectors in real space, it is possible to obtain the vectors that define the reciprocal lattice, that is, a representation of the periodicity of the Bi_2Te_3 crystal structure in Fourier space. According to the relation $\boldsymbol{t}_i.\boldsymbol{G}_j = 2\pi\delta_{ij}$ the vectors that allow building the reciprocal lattice are given by:

$$\boldsymbol{G}_1 = \frac{2\pi}{a}\left(-1,-\frac{\sqrt{3}}{3},\frac{a}{c}\right), \boldsymbol{G}_2 = \frac{2\pi}{a}\left(1,-\frac{\sqrt{3}}{3},\frac{a}{c}\right), \boldsymbol{G}_3 = \frac{2\pi}{a}\left(0,\frac{2\sqrt{3}}{3},\frac{a}{c}\right). \quad (3.6)$$

Once the reciprocal lattice is known, it is possible to define the first Brillouin zone (BZ) of the bismuth telluride, represented in figure 3.9(a). Due to the rhombohedral symmetry, this structure is composed of 8 hexagonal facets and 6 rectangular facets where the main points of symmetry referring to the bulk crystal are represented. As mentioned in section 2.2.3, this high symmetry points define four nonequivalent time-reversal-invariant points (TRIMs), denominated as $\Gamma(0,0,0)$, $L(\pi,0,0)$, $F(\pi,\pi,0)$ and $Z(\pi,\pi,\pi)$, where Kramers degeneracy occurs. In this figure it is also possible to observe the projection of the first BZ along the direction perpendicular to the plane and which represents the surface

region of the crystal, resulting in a two-dimensional BZ with hexagonal symmetry along which the three points of high symmetry $\overline{\Gamma}$, $\overline{K}$ and $\overline{M}$ which are commonly used to calculate the band structure of the material.

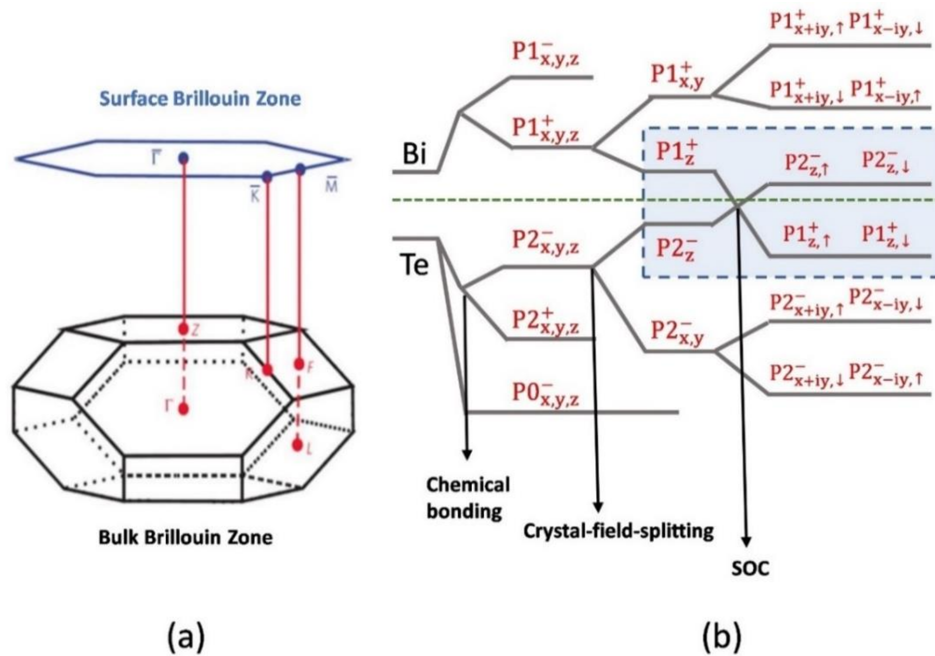

Figure 3.9: (a) Bulk first Brillouin zone of Bi_2Te_3 with surface 2D Brillouin zone projection represented by the blue hexagon. The high symmetry points $\overline{\Gamma}$, $\overline{K}$ and $\overline{M}$ are time-reversal-invariant points (TRIMs) in the 2D Brillouin zone, where Kramers degeneracy occurs. (b) Schematic representation of the band inversion process, where the Bi_2Te_3 atomic energy levels is represented taking into account different interactions such as the impact of chemical bounds, crystal field splitting and SOC, successively. The blue rectangle highlights the inversion between the Bi and Te p-orbitals. Dash green line represents the Fermi level. The figure is adapted from Ref. [19].

The band structure of Bi_2Te_3 has already been calculated in theoretical works through different methods, considering relativistic corrections and spin-orbit interaction effects between the energy levels of this material [67, 68]. As already mentioned in chapter 2, the main effect of spin-orbit coupling is to shift the minimum of the conduction band downwards relative to the valence band, resulting in inversion of bands at point Γ of the Brillouin zone. This inversion process is detailed in figure 3.9(b), where the Bi_2Te_3 atomic energy levels is represented taking into account different interactions such as the impact of chemical bounds, crystal field splitting and SOC, succesively. Since the states near the Fermi

level are predomintly from p-orbitals of Bi and Te, the states originating from s-orbitals can be neglected [19].

Initially, the strong chemical bond between the Bi and Te atomic planes within the QL (covalent or ionic) is considered. Three states related to Te p-orbital and two states from each Bi p-orbital are formed, respectively. As a consequence of chemical bonds, these initial states are hybridized and thus energetically pushed down (Te) or lifted up (Bi). The +/- signals indicates the parity of each state. Secondly, considering the effect of crystal-field-splitting, the p_z-orbital is split from the p_x and the p_y-orbitals which remain to be still degenerate. The energy levels closest to the Fermi Energy acquire opposite parity.

Finally, turning on the SOC the eigenstates are split according to their spin orientations. The position of the respective p_z-level is reversed. According to the fermi level position, band inversion occurs. This opposite parity of the inverted states results in a bulk nontrivial topology defining the Bi_2Te_3 as a strong topological insulator and leads to the formation of so-called topological states within the bulk band gap.

Figure 3.10(a) shows results of ARPES measurements along Γ-K and Γ-M directions evidencing the density of surface states existing in the electronic structure of Bi_2Te_3. In this figure it is possible to observe the conduction (BCB) and valence (BVB) bands associated with the bulk of the material separated by a finite energy gap of approximately 200 meV at room temperature. Additionally, as a result of the surface states, at point Γ, a Dirac cone-like linear energy dispersion relation that connects the valence band to the conduction band is observed. Although this material is characterized by a single Dirac cone, its band structure is a little more complicated than the band structure of Bi_2Se_3 shown in figure 2.15(c). Surface states are characterized by a Dirac point located below the maximum of the bulk valence band. In addition, a hexagonal deformation is observed in the Dirac cone (figure 3.10). In the vicinity of the Dirac point it is possible to obtain circular constant energy contours for the surface states, however, when these constant energy contours are taken in regions far from the Dirac point a snowflake-like shape is observed. This Fermi surface shape was explained with including a hexagonal warping term in the surface Hamiltonian, which can be connected with some surface properties in Bi_2Te_3 [19].

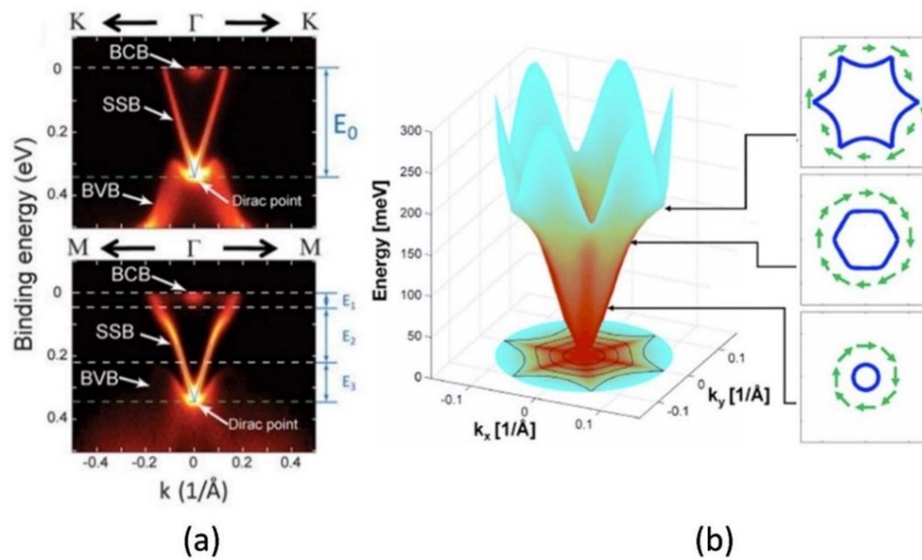

Figure 3.10: Bi_2Te_3 band structure. (a) ARPES measurements along Γ-K (upper panel) and Γ-M (lower panel) directions showing the surface states (SSB) connecting the bulk valence band (BVB) and bulk conduction band (BCB) along the band gap. The Dirac point where the surface states crosses are viable and are located buried under the bulk valence Band. (b) In Bi_2Te_3 the surfaces states linear energy dispersion deviates slightly from Dirac cone showing a hexagonal deformation. Circular constant energy contours (right panel) are shown as a function of Dirac point distance. The figure is adapted from Ref. [69].

These surface states have many interesting properties. For example, they are states protected by time-reversal symmetry so that a gap cannot be opened by non-magnetic impurities. Furthermore, the spins of electrons are correlated to their electronic moment in such a way that their spin angular momentum is always perpendicular to the **k**-wave vector and is contained on the surface of the material. Time reversal forces states with wave vectors with opposite signs **k** and - **k** to have opposite spin orientations [19] as a consequence a surface charge current inevitably results in a non-zero spin density.

All the mentioned properties make Bi_2Te_3 a promising material in the development of devices used in the areas of quantum computing and spintronics. However, there are still some challenges to be overcome regarding the exploration of surface states. Recent studies indicate a strong dependence of the electronic properties with the thickness, as can be seen in figure 3.11, that is, with the number of quintuple layers (QLs) [69]; in addition to the already mentioned difficulty of growth of the Bi_2Te_3 stoichiometric phase. Bulk monocrystal growth techniques, such as the Bridgman method, result in structures with a large number of charge carriers in the volume that shift the fermi level from the material

to the conduction band and end up masking the contribution of surface metallic states. For this reason, an alternative found by the researchers is the growth of nanostructures and thin films of Bi_2Te_3 through various epitaxial growth techniques that allow the production of high-quality structures and with a higher surface-to-volume ratio that helps to suppress the bulk residual conduction.

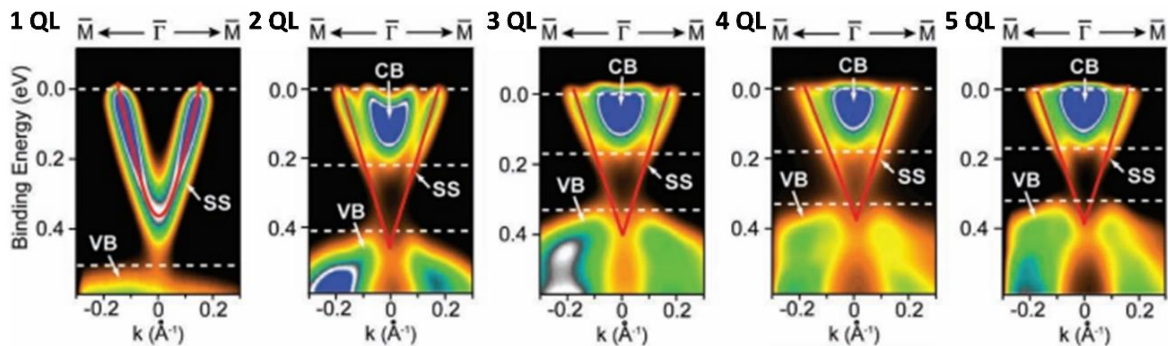

Figure 3.11: Band structure of Bi_2Te_3 obtained by the technique of angle-resolved photoemission spectroscopy (ARPES) as a function of the number of quintuple layers of the material. It is possible to observe that the Dirac cone at Γ point appears only for a thickness above 2 QL. The figure is adapted from Ref. [70].

3.2.2.3. Vibration properties

There are several works that indicate a close relationship between the surface states and the phonons in topological insulators materials [71-74]. Based on this, it is important to detail the vibration properties of Bi_2Te_3 crystals.

The primitive rhombohedral unit cell of Bi_2Te_3 shown in figure 3.6 contains five distinct atoms, each with three degrees of freedom. It is important to note that within the quintuple layer the central Tellurium atom denoted by superscript 2 represents an inversion center resulting in a centro-symmetric structure. Based on this, is expect a total of fifteen lattice vibration modes at any given wave vector in Brillouin zone center, three acoustic and twelve optical. A schematic representation of atomic displacements for these modes at the Γ point are displayed in Fig. 3.12. Based on Group theory, the Bi_2Te_3 vibration modes are labeled according to their symmetry with *A* modes belonging to a one-dimensional irreducible representation and *E* modes belonging to a two-dimensional (doubly degenerate) irreducible representation [71]. The subscripts *u* and *g* indicate an odd or even parity about the central atom in the primitive cell ($Te^{(2)}$) making these lattice vibration modes exclusively

either Raman or infrared active. As a consequence of inversion crystal symmetry, the A_{1u} mode must be odd parity and accessible only by IR (Infrared) spectroscopy whereas the E_g, A_{1g} modes must be even parity and are only accessible via Raman scattering. Since the E modes are doubly degenerate the number of unique optical phonon frequencies is reduced from twelve to eight [72-74].

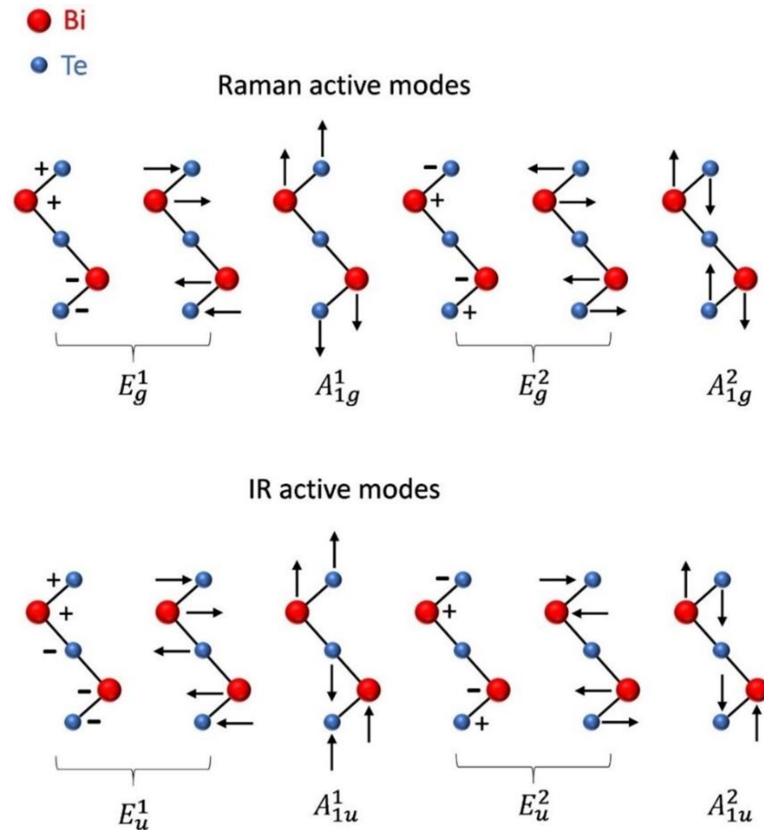

Figure 3.12: Schematic representation of Raman active and Infrared-active (IR-active) vibration modes in the Bi_2Te_3 crystal. The "+" and "-" signs in the figure indicate atomic displacement toward and from the observer. The figure is adapted from Ref. [71].

Regarding Raman active modes, the A_{1g}^1 mode represents symmetric out-of-plane stretching of Bi-Te atoms vibrating in opposite directions, while the A_{1g}^2 mode represents out-of-phase vibrations between Bi and Te atoms, a short displacement induces higher phonon frequency in this vibration modes. On the other hand, E_g mode is caused by symmetric in-plane bending and shearing the upper two layers of Bi-Te atoms vibrating in the same direction, which make a greater atomic displacement by producing lower phonon frequency.

4. Experimental techniques

In this chapter, the most relevant experimental techniques used throughout this thesis will be described. The first section is dedicated to the molecular beam epitaxy (MBE) technique, used in the growth of SiGe layers and Bi_2Te_3 nanostructures and thin films. The following sections depict structural and morphological characterization techniques. X-ray diffraction and x-ray reflectivity were used in the analysis of both SiGe layers and Bi_2Te_3 structures, allowing a detailed study of the strain conditions and epitaxial relations in these systems. Finally, the chapter ends with an exposition of scanning probe microscope techniques. Atomic force microscopy (AFM) and scanning tunneling microscopy and spectroscopy (STM/STS) were essential tools in the study of Bi_2Te_3 structures and electronic properties of Europium-doped Bi_2Te_3 films.

Other techniques were used in this work to complement and/or corroborate the structural and morphological analysis of MBE grown structures such as Raman spectroscopy, Ultra Low Energy Secondary Ion Mass Spectroscopy (ULE-SIMS), Scanning Electron Microscope (SEM) and Density Function Theory (DFT). Since they were carried out with the help of collaborators, a brief description of each of them will be provided throughout the text.

4.1. Molecular Beam Epitaxy (MBE)

Molecular Beam Epitaxy (MBE) is a powerful technique for growing thin epitaxial layers and nanostructures made of a variety of materials such as semiconductors [75], metals [76], insulators [77] or organic compounds [78]. The main advantage of MBE compared to other growth techniques is its significantly more precise control of the beam fluxes and growth conditions, allowing the deposition of structures with high crystalline quality, accurate thickness control, smooth and abrupt interface formation for heterojunctions, reliable stoichiometry and broad range of doping conditions [26].

In general, the physical principles of this technique can be grouped in three main steps: production of target atomic or molecular species, mass transport of this material to a substrate and atomic assembly of the species on the substrate surface. MBE systems work in ultra-high vacuum environment that enable atoms and molecules to travel in nearly collision free paths before arriving at the substrate surface. Furthermore, the growth occurs under conditions far from thermodynamic equilibrium and is controlled mainly by adatom kinects at the substrate surface. Such process takes place when the impinging beam reacts with the topmost atomic layers at the growth front [26].

A general schematic of an MBE growth chamber is shown in figure 4.1(a). It consists of an ultra-high vacuum deposition chamber (typically 10^{-8} Pa, or 10^{-10} Torr) with several built-in effusion cells, each of them charged with solid sources of different elements. In a growth process, the effusion cells are heated up to a temperature in which their elements start to evaporate. At this stage, precise control of cell temperature is necessary to provide a stable molecular beam, with a fixed deposition rate of compounds. The temperatures of effusion cells and the substrate holder are individually stabilized by means of controllers and power sources. In front of each of effusion cell mechanical shutters are installed. When activated or shutted off, they can allow or block (respectively) the passage of molecular beams enabling the growth of layers with sharp interfaces.

Once the cell shutter of the desirable element is open, an atomic or molecular beam (depending on the source element or compound) leaves the cell targeting a heated crystalline substrate. The atomic beams combine the elements at the surface of the substrate, which is kept at a fixed and calibrated temperature, that provides sufficient thermal energy to the impinging atom to migrate across the surface [26]. The substrate holder can also be rotated to homogenize the thickness of grown layers.

On the substrate surface, several chemical and physical processes occur, represented in figure 4.1(b), which are associated with the interaction of the atom/molecule coming from the beam with the surface sites, that is, regions with suitable chemical activity and interaction probability. Some surface regions such as atomic steps and lattice vacancies present low activation barriers for adatoms, allowing that adsorbed species bond to the

substrate crystal lattice. During a typical growth process, atoms that reach the substrate surface have an energy distribution, often related to the source (effusion cell) temperature. After reaching a surface that has usually a lower temperature adatoms can be re-evaporated immediately, or exchange energy with atoms on the surface of the substrate, until local conditions near thermodynamic equilibrium are reached and they incorporate into the substrate.

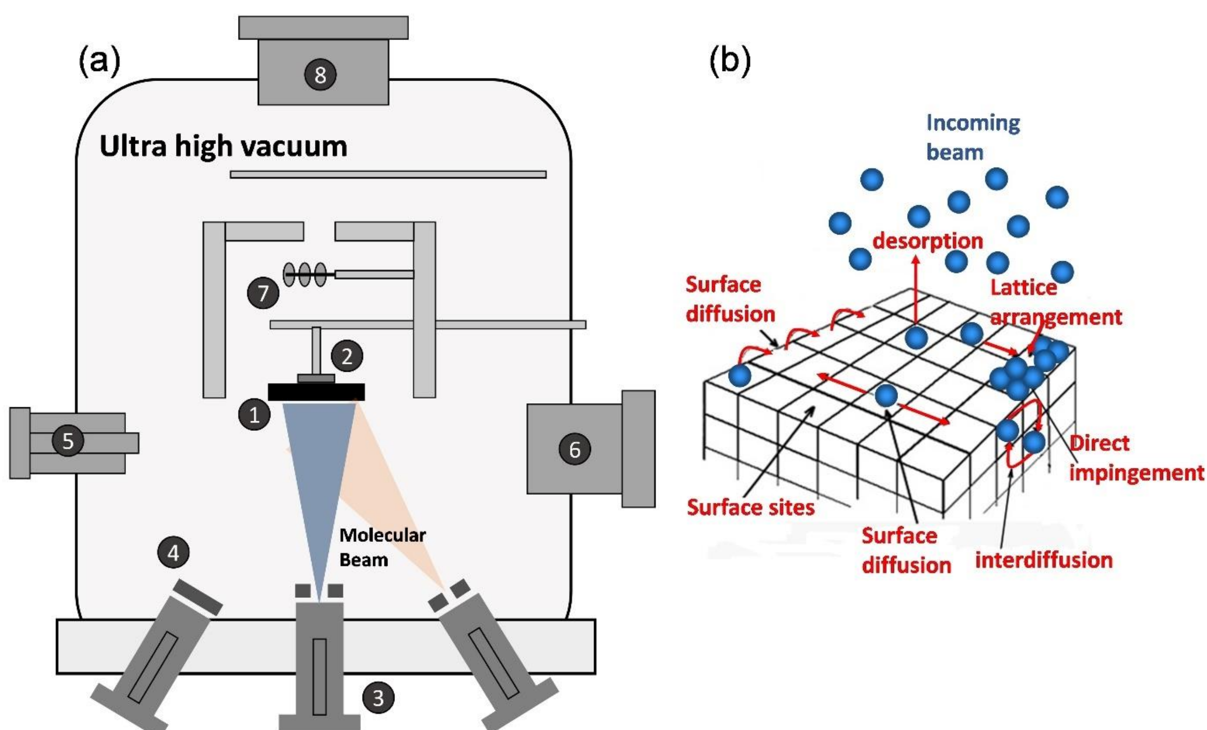

Figure 4.1: (a) Schematic representation of the main elements of an MBE growth chamber: 1-crystalline substrate, 2-sample holder, 3-effusion cells, 4-shutters, 5 and 6 represent, respectively, an electron gun and a fluorescent screen used for Reflection High Energy Eletron Diffraction (RHEED) to monitor in-situ characterization, 7-vacuum gauge and 8- Sample transfer port. (b) Schematic representation of processes that take place at the substrate surface during the MBE growth. The most relevant processes are: Adsorption of species on the substrate surface; surface diffusion of the adsorbed molecules/atoms; incorporation and lattice arrangement of the constituent atom into the surface sites or epilayer and thermal desorption of the species not incorporated into the crystal lattice.

As the growth proceeds and more atoms are adsorbed, they interact with each other, resulting in the spontaneous formation of nuclei along the surface of the substrate, a process called nucleation. From this process, these nuclei grow occupying the entire surface of the substrate, leading to the formation of an epitaxial layer. The growth mechanism by which this occurs depends on several factors, including a balance of kinetic processes

depicted in figure 4.1(b). However, a broad and general description of the growth leads to one of three main categories: Island growth (Volmer-Weber), layer-by-layer growth (Frank van der Merwe) and an intermediate stage in which layer-island growth occurs (Stranski-Krastanov). A schematic comparison of these modes is shown in figure 4.2.

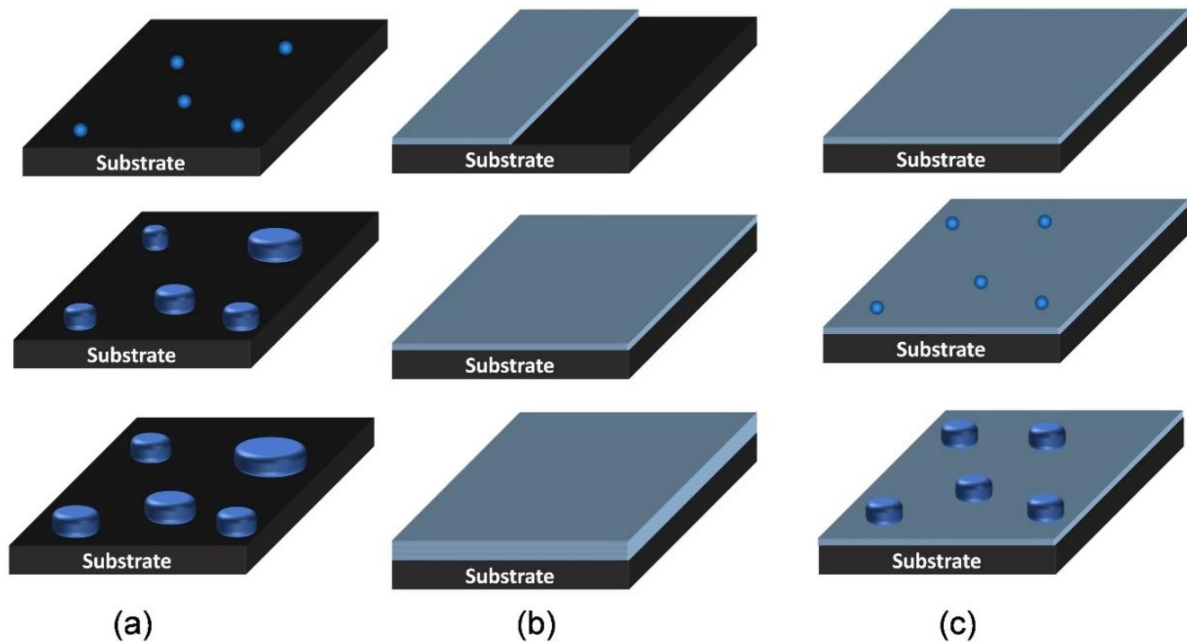

Figure 4.2: Schematic illustration of the three different epitaxial films growth modes. (a) Volmer-Weber growth mode; (b) Frank-van der Merwe growth mode and (c) Stranski-Krastanov growth mode.

Volmer-Weber mode is obtained when atoms deposited are strongly bonded to each other and have reduced chemical or structural affinity with the substrate. Small clusters (e.g, dimers or trimers) are nucleated at various points on the substrate surface, and subsequent atoms tend to bound at these points. The result is an ensemble of 3D islands that grow and eventually coalesce as more material is deposited. In contrast, growth in the Frank van der Merwe mode occurs when deposited atoms are more likely to bond with the substrate, so that the atoms tend to cover the surface and from there the growth always proceeds layer-by-layer. The Stranski-Krastanov mode is a combination of the previous two modes and initially results in the formation of a complete layer. However, after a certain thickness in which a given elastic energy threshold is reached, the growth of islands becoms more favorable, allowing strain tensions to accommodate in the lattice [26].

4.2. X-ray diffraction (XRD)

X-rays were discovered by Wilhelm Conrad Röntgen at the end of the 19th century. Since that time, they have become established as an indispensable probe of the structure of matter [79]. In particular, the completely non-destructive character and the fact that in general it does not require any prior sample preparation have render X-ray diffraction into a highly versatile characterization technique allowing the structural investigation of many material classes ranging from low-dimensional structures [80-82] to complex systems of biological macromolecules [83]. Indeed, the analysis of X-ray diffraction pattern makes possible the accurate determination of atomic positions and the strain tensor components in heteroepitaxial systems, providing information about in-plane (interfacial) and out-of-plane (along growth direction) lattice parameters [79].

Basically, the phenomenon of diffraction in solids is associated with the coherently scattering process that the X-ray beam with wavelength λ undergoes when interacting with atoms of a given sample. In particular, the beam will interact with the electron clouds and will be scattered in directions that are ultimately related to the order and periodicity of atoms in the material. The strength with which atomic species scatter x-rays is proportional to the number of electrons that characterize the atom [84].

In this sense, the periodicity of the crystal structure added to the fact that the wavelength of the radiation is comparable to interatomic distances allows that, for very specific directions, the X-rays on a crystal are scattered in phase and, consequently, can intensify x-ray reflections in these directions due to the constructive interference phenomena. The necessary condition for this process to occur is given by Bragg's law, proposed in the beginning of the 20th century.

4.2.1. Bragg's Law and diffraction condition in reciprocal space

When observing the X-ray diffraction pattern presented by a crystalline solid, in 1913, W. L. Bragg verified a certain similarity of this diffraction pattern with experiments that involved the specular reflection of visible light [85]. Bragg then introduced the hypothesis that a collimated X-ray beam, when incident on a crystal, would be reflected in a

specular way by the set of parallel and equidistant planes of atoms inside the material. In this way, for certain directions and fixed wavelength, very pronounced intensity maxima of scattered radiation would be observed.

The presence of these maxima, called Bragg peaks, would be closely related to the optical path difference between beams scattered by different crystal planes. The occurence of constructive interferences depends on the angle of incidence (θ), the wavelength of the radiation (λ) and the spacing between adjacent planes (d_{hkl}) of the material. The relationship between these variables is expressed by Bragg's law (for integer n):

$$2d_{hkl}\sin\theta = n\lambda\,. \tag{4.1}$$

Thus, the condition for observing a Bragg peak and, therefore, for constructive interference to occur is that the optical path difference is equal to an integer number of wavelengths. In equation (4.1), θ is known as the Bragg angle, and is defined between the incident beam and the crystal plane, d_{hkl} is the interplanar distance between planes defined by Miller indices (hkl), λ is the radiation wavelength and n is an integer that defines the order of the studied diffraction. A geometric description of this law is sketched in figure 4.3.

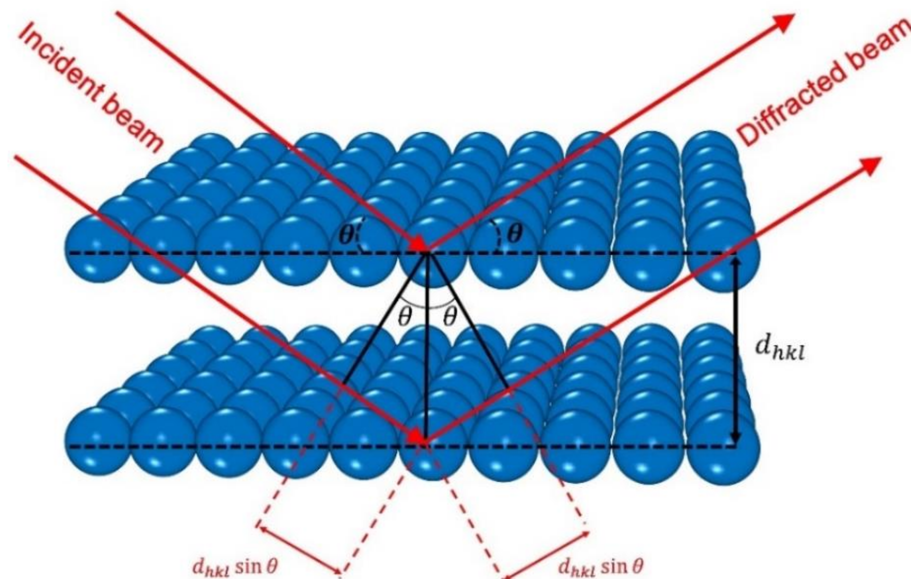

Figure 4.3: Schematic representation of X-ray diffraction by parallel planes. Bragg's law states that constructive interference occurs whenever the path difference is an integer of the wavelength.

The d_{hkl} values are obtained through specific equations for each type of crystal structure. In particular, equations (4.2) and (4.3), shows the relationship between interplanar distance, d_{hkl}, and the lattice parameter for the cubic and hexagonal structure, respectively:

$$d_{hkl} = \frac{a}{\sqrt{h^2+k^2+l^2}} \quad (4.2)$$

$$d_{hkl} = \frac{a}{\sqrt{\frac{4}{3}(h^2+hk+k^2)+\left(\frac{a}{c}\right)^2 l^2}} \quad (4.3)$$

where a and c are the in-plane and out-of-place lattice parameters.

As a direct consequence of Bragg's formulation, for diffraction to occur, the wavelength is limited to the condition of being at most equal to twice the interplanar distance, that is, $\lambda \leq 2d_{hkl}$. For this reason, this phenomenon is not observed even in environments where Young's experiment works. Another important feature is that in equation (4.1) the parameter associated with the crystal is the interplanar distance, not appearing any magnitude associated with the position of the atoms in these planes, which, in fact, are responsible for the scattering power of the radiation as initially discussed in the previous section. Therefore, Bragg's law is a necessary condition that provides the possible direction for a diffracted beam to be observed, but not sufficient for the observation of an intensity maximum. The scattered intensity is proportional to the modulus of the structure factor, expressed in equation (4.4), which depends on the symmetry of atomic positions within the unit cell (lattice), and on the presence of an atomic basis inserted within this symmetry [84].

$$F_{hkl} = \sum_{i=1}^{n} f_n \, e^{2\pi i(hx_n+ky_n+lz_n)} \quad (4.4)$$

In equation (4.4), f_n is the atomic scattering factor, that represents the strength which an atom scatters x-rays, x_n, y_n and z_n are the coordinates of nth atom in the unit cell and (hkl) are Miller indices.

Thus, depending on the crystal structure, Bragg's law can be satisfied, but if structure factor is null no diffracted beam is observed. As an example, the layered structure of Bi_2Te_3 results in a structure factor that allows non-zero reflection intensity of the crystalline planes of the $(00L)$ family only if $L = 3n$ (with integer n) [86].

In addition to the features highlighted above, a simple manipulation of equation (4.1) allows us to observe that the Bragg angle θ, which is the quantity determined in a typical X-ray diffraction experiment, is inversely proportional to the interplanar distance, i.e, $sin \ \ \theta \propto 1/d_{hkl}$. However, from solid state physics theory the inverse of the interplanar distance is precisely the modulus of the reciprocal lattice vector that represents the set of (hkl) planes of the direct lattice [79]. Consequently, the reciprocal lattice of a crystal is closely associated with the diffraction pattern presented by it.

The concept of reciprocal space offers a simple geometric basis for understanding the phenomenon of X-ray diffraction [85]. However, it is convenient to express Bragg's law in vector notation [84].

From a geometric point of view, Bragg's law is essentially represented in two dimensions with the incident beam, the diffracted beam and the normal to the plane considered being always coplanar. In this way, X-ray diffraction can be represented in terms of an incident wave vector $\boldsymbol{K}_0$ and a diffracted wave vector $\boldsymbol{K}$. The direction of $\boldsymbol{K}_0$ differs from the direction of $\boldsymbol{K}$ by 2θ. In the condition of elastic scattering, we have that $|\boldsymbol{K}| = |\boldsymbol{K}_0 \ | = k$. In terms of these two vectors, the scattering vector (also known as the moment transfer vector) is defined as $\boldsymbol{q} = \boldsymbol{K} - \boldsymbol{K}_0$, and according to the geometric relation represented in figure 4.4, it has a modulus given by:

$$| \ \boldsymbol{q} \ | = | \ \boldsymbol{K} - \ \boldsymbol{K}_0 \ | = 2k \sin \theta \tag{4.5}$$

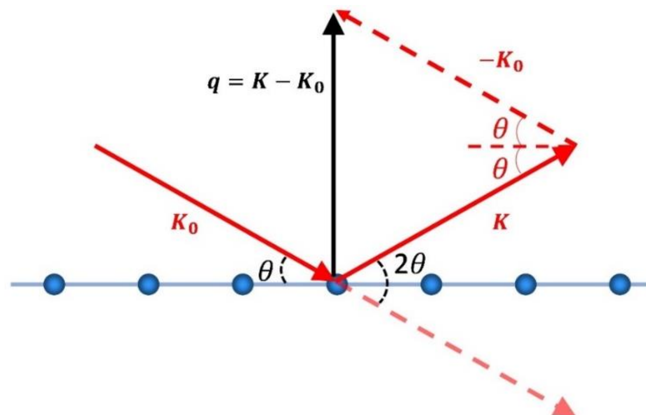

Figure 4.4: Definition of scattering vector $\boldsymbol{q} = \boldsymbol{K} - \boldsymbol{K}_0$; $\boldsymbol{K}_0$ points in the incident direction, and $\boldsymbol{K}$ in the scattered direction.

Considering the equation that defines the wave vector $k = 2\pi/\lambda$, we obtain

$$|\boldsymbol{q}| = \frac{4\pi \sin\theta}{\lambda} \tag{4.6}$$

Now, by combining equations (4.1) and (4.6), we find a reciprocal relationship between the magnitude of the scattering vector $\boldsymbol{q}$ and the interplanar distance d_{hkl},

$$|\boldsymbol{q}| = \frac{2\pi}{d_{hkl}} \tag{4.7}$$

but, as discussed, the right side of equation (4.7) is the modulus of the reciprocal lattice vector, $|\boldsymbol{G}_{hkl}|$, associated with the plane (hkl) of the crystal. Therefore, the reciprocal space diffraction condition, known as Laue's condition, is written as:

$$\boldsymbol{K} - \boldsymbol{K}_0 = \boldsymbol{G}_{hkl} \tag{4.8}$$

In other words, constructive interference occurs whenever the scattering vector $\boldsymbol{q}$ is a vector of the reciprocal lattice of the crystal. At this moment, the importance of the reciprocal lattice concept in the study of diffraction becomes evident, since it is possible to represent the set of all possible crystalline planes simply by points in the reciprocal lattice. Furthermore, in an X-ray diffraction measurement, the scatter vector is the physical quantity under full control [87], as the sample orientation and the detector position determine the directions of the vectors $\boldsymbol{K}_0$ and $\boldsymbol{K}$, respectively. Figure 4.5 illustrates the constructive interference process in reciprocal space.

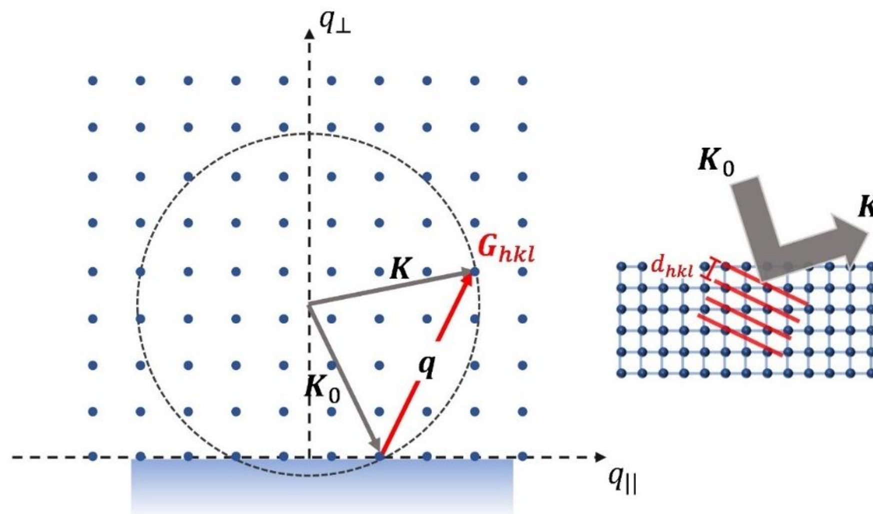

Figure 4.5: Schematic representation of the diffraction condition in reciprocal space. The laue condition states that only if the scattering vector $\boldsymbol{q}$ is equal to a reciprocal lattice vector G_{hkl}, constructively interference occurs and diffraction can be observed. In this figure, blue solid dots represent reciprocal lattice points and in reciprocal lattice each point represents a vector which, in turn, represents a set of Bragg planes. The correspond scattering process in real space is also shown.

4.2.2. Measurement setup

The basis for understanding how an X-ray diffraction measurement works is all contained in Bragg's law and its reciprocal space version. In practice, when a collimated X-ray beam with a defined wavelength impinges on a crystal, only the sets of planes that present a given interplanar distance and a given direction relative to the incident beam, satisfying Bragg's law, scatter the radiation constructively. Thus, the measurement process is limited to an orientation of the sample, in terms of incidence angle and diffraction angle, which allows observing the intensity of the diffracted beam in a certain region.

Usually, there are two types of sources for generating x-rays: the x-ray tube and the synchrotron. In the first one, X-rays are generated when an accelerated electron beam is produced by a heated filament and accelerated by a fixed potential. The beam energy is set to values near $40\ keV$ (depends on the target metal), and collides with a heavy metal target. In addition to the discrete values of energy that are characteristic of the target material, there is a continuous part that encompasses several wavelengths, generated by the breaking process of the electron beam when they reach the target. In the second one, charged particles accelerated at velocities close to the speed of light, are confined to travel in near-circular paths in a 'storage ring' which consists in a series of dipole magnets placed at regular intervals around the ring [79]. Thus, X-rays are emitted as a result of the frequent inward radial acceleration of the electrons generating a much more intense and continuous radiation spectrum when compared with x-ray tubes.

In this work, all samples were analyzed in synchrotron radiation sources. Figure 4.6(a) shows a schematic of the key components of a typical beamline. After leaving the storage ring, the radiation passes through several optical elements, inside a vacuum path, which precedes the sample. The first optical element is a curved mirror, which aims to block high-energy photons. This mirror works in practice as a low pass filter. The second element of the beamline is a crystal monochromator, which allows one to select a certain wavelength. The optical system also has some elements which are able to monitor, for instance, the intensity and wavelength of the incident beam. The radiation then passes through a focusing device resulting in a narrow, parallel beam before reaching the sample.

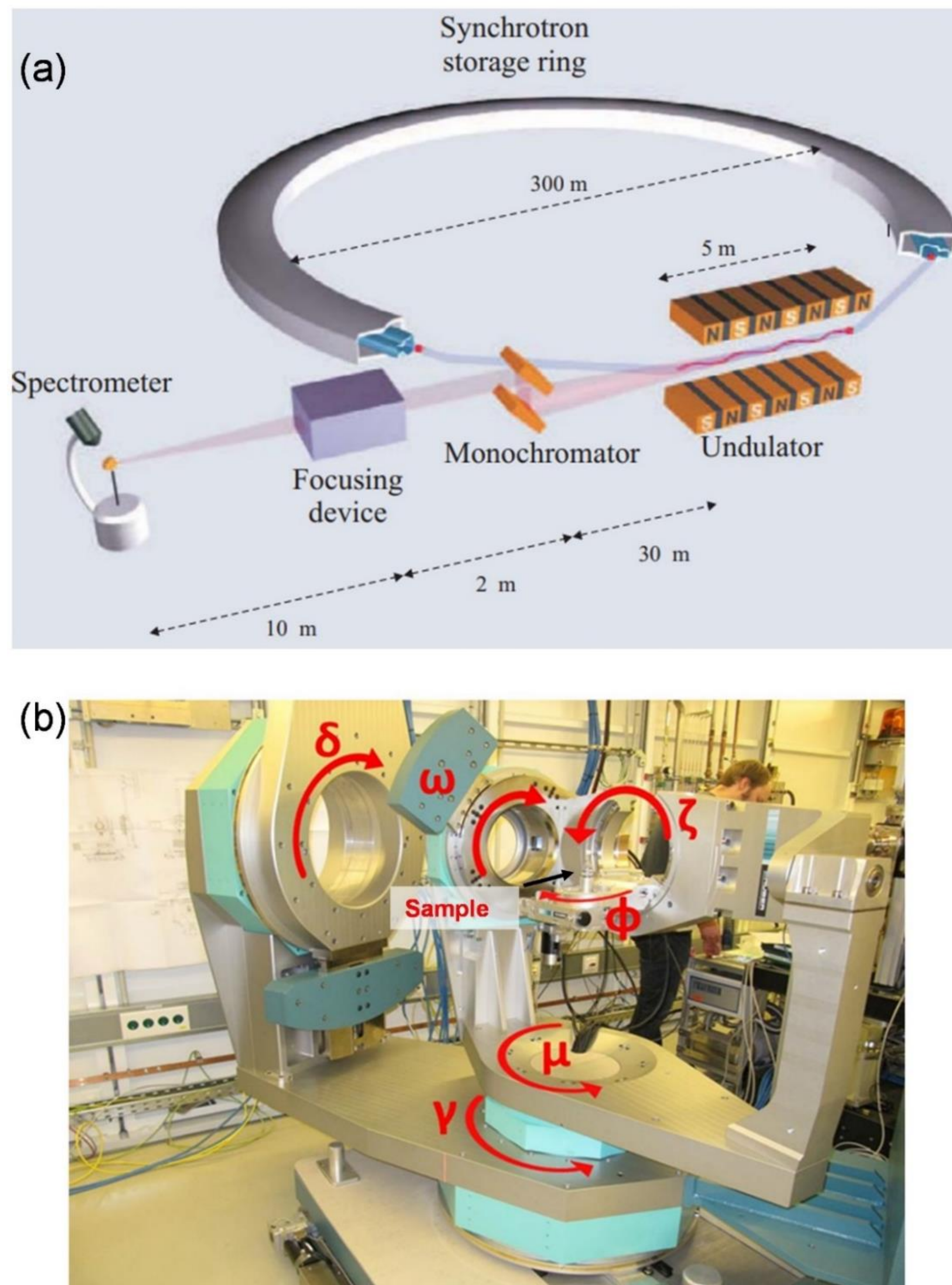

Figure 4.6: (a) Schematic representation of a typical synchrotron beam line. The ring is designed with straight sections, where an insertion device, such as undulator is place. The lattice of magnets in an insertion device forces the charged particles to execute small oscillations which produces intense beams of radiation. Figure taken from reference [79]. (b) Schematic representation of the six-axis goniometer, showing the different degrees of freedom (δ, ω, ζ, ϕ, μ and γ) of the sample.

The sample is fixed in a six-axis goniometer and X-ray diffraction data are obtained through so-called scans, where the different angular degrees of freedom shown in

figure 4.6(b) are explored, while the diffracted intensity is registered. Each type of scan provides different structural information about the studied sample and allows exploring different regions of the reciprocal space.

4.2.2.1 $\boldsymbol{2\theta-\omega}$ Scans

In this type of scan, an X-ray beam is focused at an angle ω always in relation to the sample surface and the detector is positioned at an angle 2θ always in relation to the incident beam. The scan is then carried out by increasing 2θ by twice the increment used in angle ω, which is equivalent to moving detector and sample simultaneously, keeping the angular velocity of the detector twice the angular velocity of the sample. A schematic representation of the setup used during this kind of scans can been show in figure 4.7(a).

In a scan like the one described above, the direction of the scattering vector, $\boldsymbol{q}$, remains unchanged while its modulus is varied by scanning the reciprocal space always perpendicular to the crystalline plane under investigation. Furthermore, this scan is called coplanar because the vectors $\boldsymbol{K}_0$, $\boldsymbol{K}$ and $\boldsymbol{q}$ are contained in the same plane, giving information about the volumetric configuration of the atomic planes.

When $= 2\theta/2$, the vector $\boldsymbol{q}$ is oriented along the normal to the surface of the sample, as illustrated in figure 4.7(b), characterizing a so-called symmetric $(2\theta-\theta)$ scan (often also called longitudinal or radial scan). In this condition, if the sample is single-crystalline, only planes parallel to the surface of the sample whose points of the reciprocal lattice are along the normal are investigated. If the sample is polycrystalline, all planes are measured, because there will always be some crystalline domain (crystallite) with the correct plane parallel to the surface [84]. In addition to allowing inferring whether the sample is monocrystalline or polycrystalline, this type of measurement provides information about the out-of-plane lattice parameter and also allows obtaining information about the epitaxial layer/substrate relationship.

In the case of $\omega \neq 2\theta/2$, the vector $\boldsymbol{q}$ is inclined relative to the normal to the sample surface, as illustrated in figure 4.7(c), characterizing an asymmetric scan. In the case of single crystals, in this scan we are interested in those planes that are not parallel to the

sample surface, whose reciprocal lattice points are not along the direction normal to the surface. The difference between the incidence angle ω, defined with respect to the surface, and the Bragg angle θ, defined with respect to the crystalline plane, is called the offset. This type of measurement is extremely important in epitaxial systems, as it allows obtaining information about the in-plane and out-of-plane lattice parameter.

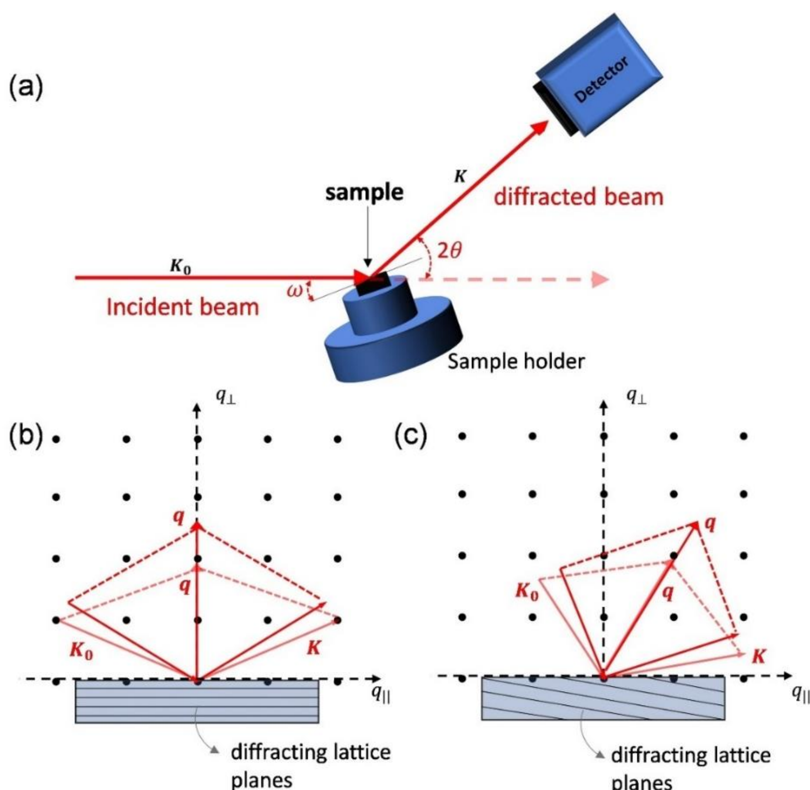

Figure 4.7: (a) Schematic representation of a $2\theta - \omega$ scan, in this type of scan, an X-ray beam is focused at an angle ω with respect to the sample surface and the detector is positioned at an angle 2θ always in relation to the incident beam. (b) Diagram where we can see how reciprocal space is swept in a symmetrical $2\theta - \theta$ scan, only those crystalline planes that are parallel to the sample surface can be measured. (c) Reciprocal space geometry in an asymmetrical $2\theta - \theta$ scan, scanning those planes that are inclined with respect to surface normal. The solid black dots in panels (b) and (c) representing the reciprocal lattice points.

Depending on the material studied, the Laue geometry can be applied. In this measurement, represented in figure 4.8, a collimated and monochromatic x-rays beam hits the sample and the detector is positioned to receive the radiation transmitted by it, i.e., the x-ray beam penetrates through the sample. The scanning is performed in the same way described above with increasing 2θ by twice the increment used in angle ω. In this type of geometry surface normal is parallel to the reflecting planes, thus providing information

about the in-plane lattice parameter. However, this geometry is limited to practical uses in micrometer- or milimiter-thin samples (depending on average atomic number Z and energy used) due to x-rays absorption phenomenon.

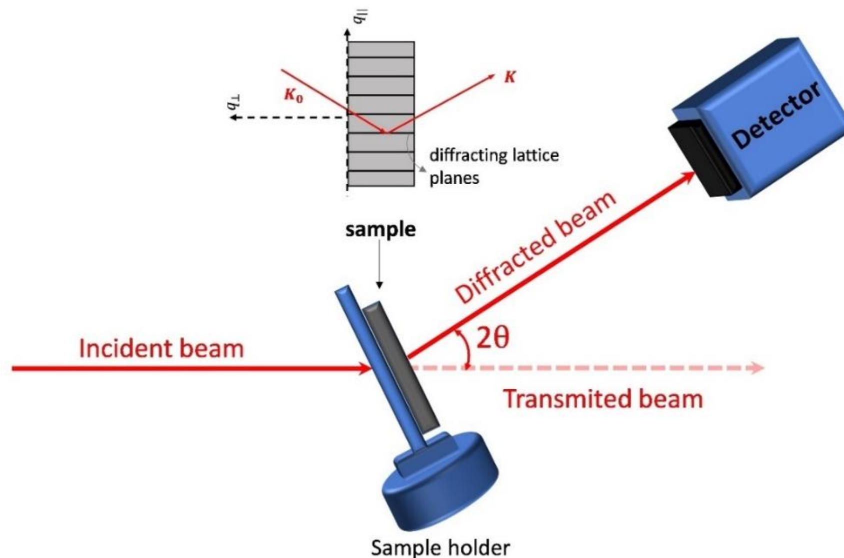

Figure 4.8: Schematic representation of a Laue $2\theta - \omega$ scan, in this type of scan, a collimated and monochromatic x-rays beam hits the sample and the detector is positioned to receive the radiation transmitted by it. The inset shows the diffraction by crystalline planes whose normal are parallel to the surface sample.

4.2.2.2 Grazing Incidence Diffraction (GID)

As discussed in previous section the coplanar X-ray diffraction geometry can provide information about in-plane and out-of-plane lattice parameter depending on the orientation of sample with respect to incident and diffracted beam. However, when studying an epitaxial system, it is expected that the crystalline arrangement of the substrate will be repeated in the layer that has been grown. Thus, when performing an X-ray diffraction measurement in this material, two contributions are expected: one referring to the layer and the other referring to the substrate. In this situation, depending on the information you want to study, the scattering associated with the substrate can overshadow the scattering of the epitaxial layer, especially in the case of nanostructures which has much smaller volume than the substrate and materials where the transmission geometry cannot be applied.

Based on this, in order to minimize the substrate signal and use x-ray as a surface sensitive probe a non-coplanar geometry known as Grazing Incident Diffraction must be

employed. Due to refraction of the incoming beam at the air-sample interface the penetration depth of the probing x-ray can be controlled [88]. Hence, below a certain critical angle the incoming beam became evanescent and propagates parallel to and close below the sample surface, thus we are able to investigate the planes perpendicular to the sample surface.

In a GID measurement setup, a large part of the incident beam is specularly reflected on the sample surface and a small part penetrates a few nanometers into the material, being diffracted by planes perpendicular to the surface plane. As depicted in figure 4.9, the incident $\boldsymbol{K}_0$ and the diffracted $\boldsymbol{K}$ wave vectors are almost confined to the surface plane and consequently is the scattering vector $\boldsymbol{q}$ that is nearly perpendicular to the substrate normal [88]. During a measurement a monochromatic and parallel x-ray beam strikes the sample surface at an angle α_i close to the critical angle α_c. As usual the recording of the diffraction pattern proceeds by continuously increasing the scattering angle 2θ moving the detector perpendicularly oriented with respect to the sample surface.

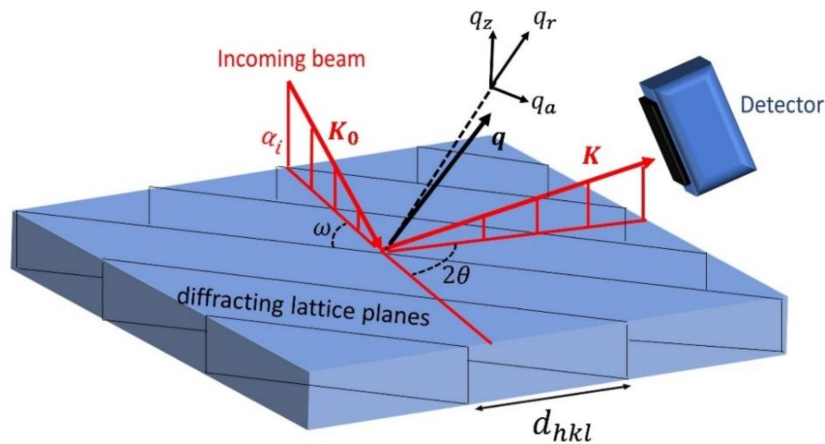

Figure 4.9: Diffraction by a crystal with lattice spacing d_{hkl} in GID geometry. In this configuration a monochromatic and parallel x-ray beam strikes the sample surface at an angle α_i close to the critical angle α_c, the diffracted beam mainly conveys information about the surface structure of the sample. The scattering vector $\boldsymbol{q}$ is decomposed into three components (q_a, q_r and q_z) that que provide different information during a scan.

In this framework, the scattering vector can be decomposed in three components, represented in equations 4.9, each of them can be used to study different properties of the sample. By scanning along q_a, we can obtain information about the size

and shape of a region with a certain lattice parameter. Scans along q_r are analogous in GID to $2\theta - \omega$ scans discussed in the previous section in the specular techniques, whereas with scans along q_z, we can analyze the crystal structure of the material.

$$q_a = \frac{4\pi}{\lambda}\sin\left(\frac{2\theta}{2}\right)\sin\left(\frac{2\theta}{2} - \omega\right)$$
$$q_r = \frac{4\pi}{\lambda}\sin\left(\frac{2\theta}{2}\right) \quad (4.9)$$
$$q_z = \frac{4\pi}{\lambda}(\sin\alpha_i + \sin\alpha_f)$$

4.3. X-ray reflectivity (XRR)

X-ray specular reflectivity (XRR) is a surface sensitivity technique that can be applied in order to obtain a detailed surface property of materials. Specifically, X-rays are used to probe the electron density perpendicular to the surface and thereby obtain information about the surface roughness, layer thickness and average density of a layered system [79].

As already introduced in the previous sections, at very low angles, X-rays do not penetrate the sample volume due to total external reflection. This property is directly associated with the fact that refractive index of material media n in the region of X-rays is slightly smaller than unity. Indeed, it can be defined as:

$$n = 1 - \delta + i\beta \quad (4.10)$$

where δ is the correction due to dispersion and β the correction associated with absorption effects [79]. Typically, the magnitude of δ is in the range of 10^{-6} and β is much smaller [79].

In this context, the condition in which the total external reflection occurs can be easily deduced from figure 4.10 that represents the reflection and transmission (refraction) of X-ray beam when it is incident on a smooth interface between air and medium. According to Snell's law the relation between incident angle α and transmitted angle α' in a regime where the constant β is negligible are:

$$n_{air}\sin\alpha = n_{medium}\sin\alpha'$$
$$\cos\alpha = n_{medium}\cos\alpha'$$
$$\cos\alpha = (1-\delta)\cos\alpha'$$

where we use the trigonometric relation $\sin(a-b) = \sin a \cos b - \cos a \sin b$ in order represent the angles with respect the surface normal and equation 4.10 for refractive index in the medium. Now, the critical angle $\alpha = \alpha_C$ for total reflection is obtained by choosing $\alpha' = 0$, and by expanding the cosines for arguments close to 1 ($\cos \alpha \approx 1 - \frac{\alpha^2}{2}$).

$$1 - \frac{\alpha_C^2}{2} = (1 - \delta)$$

$$\alpha_C = \sqrt{2\delta} \tag{4.11}$$

thus, for values of α such that $\alpha \leq \alpha_c$ the total reflection occurs and only an evanescent wave that is exponentially damped penetrates into the material. Moreover, the dispersion coefficient can be described by $\delta = 2\pi\rho r_0/k^2$, where ρ is the electron density and r_0 the Thomson scattering amplitude. Hence, the critical angle does not depend on the arrangement of electrons in the unit cell and on the crystal structure, then unlike X-ray diffraction, reflectivity can be done in a wide range of materials at the condition that there exists a good contrast in electron density for layered samples and interfaces with roughness lower than (approximately) 10 times the used wavelength [79].

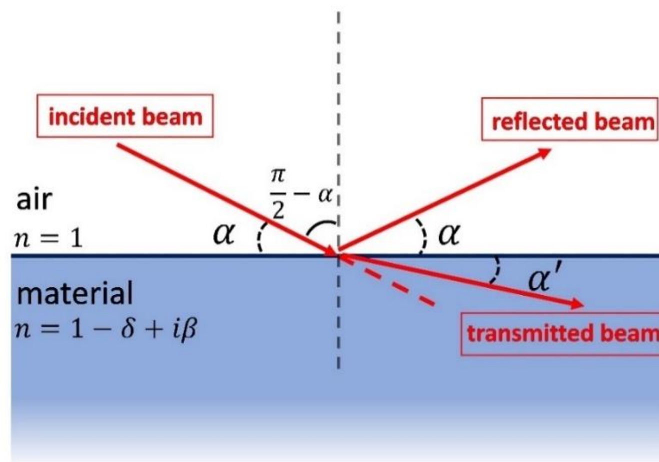

Figure 4.10: Refraction and reflection in a smooth interface that separates two media with different refractive indices. Snell 'law and Fresnel equations can be derived by requiring continuity at the interface of the wave and its first derivative.

The basic principles of the X-ray reflectivity technique can be understand applying the continuity conditions for electromagnetic waves at an interface. In the situation depicted

in figure 4.10 the coefficients of reflected (r) and transmitted (t) x-rays beam can be calculated by means of Fresnel's equations:

$$r \equiv \frac{\alpha-\alpha'}{\alpha+\alpha'} \tag{4.12}$$

$$t \equiv \frac{2\alpha}{\alpha+\alpha'} \tag{4.13}$$

As an example, in figure 4.11 we plot the reflectivity $|r|^2$ curve of a Silicon (Si), Germanium (Ge) and Gold (Au) substrate calculated for the wavelength $\lambda = 1.54$ Å as a function o incident angle α according to equation (4.12). Below the critical angle α_c, the reflectivity curve exhibits a plateau associated with the regime where the total external reflection is taking place. Above the critical angle, the reflectivity rapidly decreases. The dependence of the critical angle with the electron density ρ can also be observed, the higher the electron density of a material the higher the critical angle.

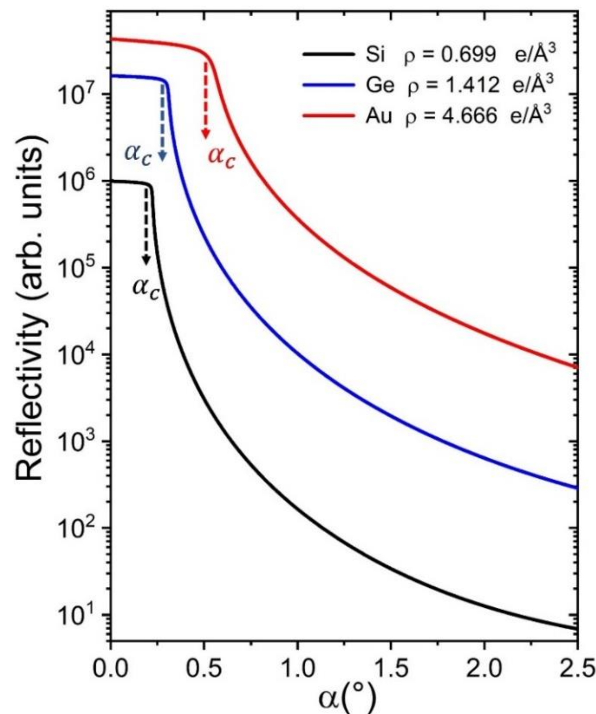

Figure 4.11: X-ray reflectivity curves for different materials. It is possible to see that above the critical angle, the reflectivity rapidly decreases. Au has a higher electronic density than Si and Ge, thus it has a higher critical angle.

For a situation of a thin layer with thickness Δ deposited on a substrate, the reflectivity is a little more complicated than the expression of equation 4.12. In this

situation, it is necessary to take into account the transmitted and reflected waves in each interface, as represented in figure 4.12(a). In contrast to the case of a single substrate, the reflectivity curves show intensity oscillations that are associated with the interference of the waves reflected from the upper and lower interfaces of the layer (see figure 4.12 (b)). The maximum intensities are observed whenever the phase difference between the reflected and transmitted beam is multiple of the wavelength. Using the matrix method, it is possible to obtain the following expression for the total amplitude reflectivity coefficient r [79]:

$$r_{layer} = \frac{r_{01}+r_{12}p^2}{1+r_{01}r_{12}p^2} \quad (4.14)$$

where r_{01} and r_{12} correspond to the reflectivity coefficient of air to layer and layer to substrate, respectively, $p^2 = e^{iQd}$ corresponds to the phase difference between the rays reflected on top and bottom faces of the layer.

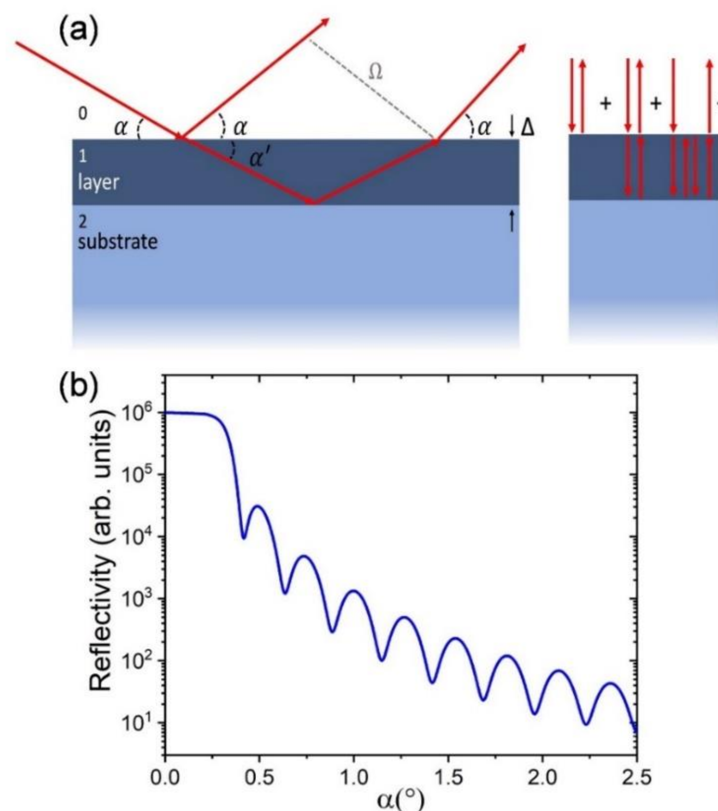

Figure 4.12: (a) Reflection and transmission from a thin layer deposit on a substrate. The layer is of thickness Δ and the total reflectivity ca be calculated taking into account the transmitted and reflected beam waves in each interface. (b) The reflectivity curves show intensity oscillations that are associated with the interference of the waves reflected from the upper and lower interfaces of the layer. The maximum intensities are observed whenever the phase difference associated with path difference Ω between the reflected and transmitted beam is multiple of the wavelength.

The situation described above for a single layer can be extended to a sample formed by several stacked layers deposited on a substrate. The reflectivity coefficient can be exactly calculated by a series of recursive equations developed by Parrat in 1954 [79]. In this formalism, the N stacked layers are indexed in order from the top to the bottom, as schematically show in figure 4.13, and each layer has thickness Δ_j and a refractive index $n_j = 1 - \delta_j + i\beta_j$ that depend on the material, where j goes from 1 to N. Therefore, starting from the interface between the bottom of Nth layer and substrate and account for the reflection of the incoming and exiting beam at the $j, j-1$ interface, similarly to equation 4.14 the reflectivity coefficient at each interface can be determined:

$$r_{j-1,j} = \frac{r_{j-1,j} + r_{j+1,j} p_j^2}{1 + r_{j,j-1} r_{j+1,j} p_j^2} \tag{4.15}$$

Then in order to calculate the final amplitude reflectivity the recursive process continues until the reflectivity coefficient at the interface between the air and first layer is computed.

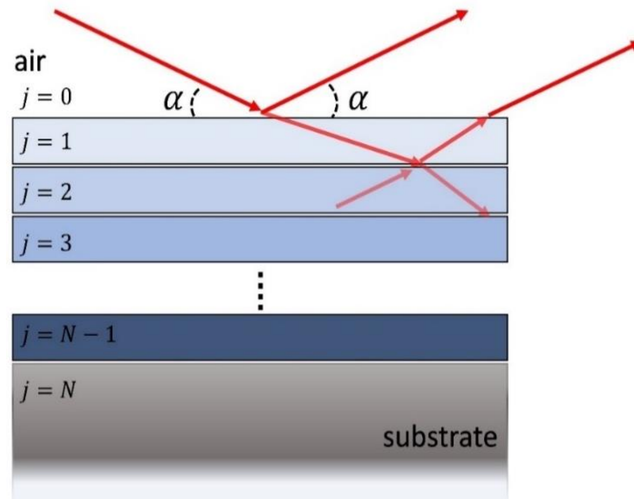

Figure 4.13: Reflection and transmission from a multilayer deposit on a substrate. The system is modeled as being composed of N layers, localized on top of an infinitely substrate. Each layer has thickness Δ_j and a refractive index $n_j = 1 - \delta_j + i\beta_j$ that depend on the material. In order to calculate the final amplitude reflectivity a recursive process is necessary.

It is important to note that equations 4.14 and 4.15 correspond to the ideal case of surfaces without roughness, however, for a more realistic case, the interfaces present a roughness that has an important role in the change in the phase of the incident wave and causes a more dramatic decrease in reflectivity. The treatment of this effect consists in

multiplying the reflectivity coefficients by an additional phase factor in order to consider the diffuse scattering due to surface roughness [79].

4.3.1. Measurement setup

In a typical XRR measurements, represented in figure 4.14, a monochromatic and parallel x-rays beam is incident at a grazing angle of incidence and specular reflection from the sample surface is measured. The configuration is essentially the same as used in a symmetrical $2\theta - \omega$ scan seen in X-ray diffraction technique, with the difference that now the X-ray beam hits the surface at very grazing angles of incidence.

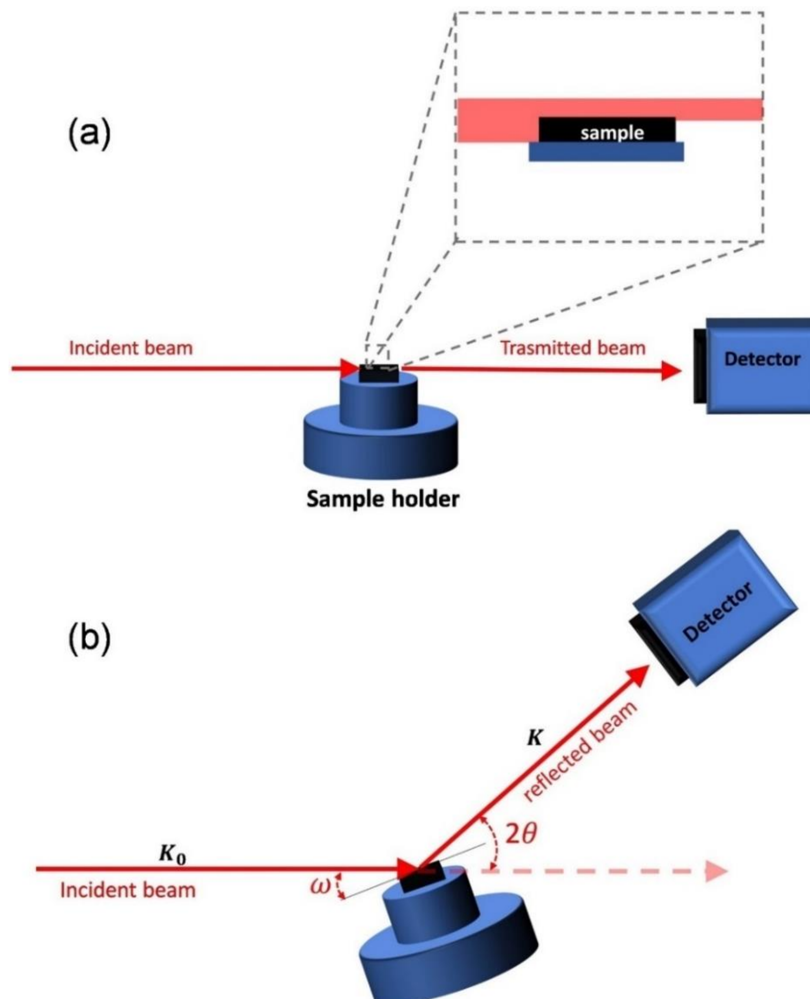

Figure 4.14: (a) Schematic of the alignment of the x-ray beam with respect to the sample, when incidence and detector angles are equal to zero, the sample surface is perfectly parallel to the beam and the sample covers exactly half of the beam. (b) X-ray reflectivity setup. The specular reflectivity is recorded increasing 2θ by twice the increment used in angle ω, which is equivalent to moving detector and sample in such a way that $\omega = 2\theta/2$ keeping the incident and reflected angle always equal.

Initially, a careful alignment of the sample with respect to the incident beam must be done, so that when the incidence and detector angles are equal to zero, the sample surface is perfectly parallel to the beam and the sample covers exactly half of the beam (figure 4.14 (a)). Afterwards, the specular reflectivity is recorded increasing 2θ by twice the increment used in angle ω, which is equivalent to moving detector and sample in such a way that $\omega = 2\theta/2$ keeping the incident and reflected angle always equal. Figure 4.14(b) shows the XRR setup, where ω is the experimental angle that corresponds to the same angle of incidence α defined in the last section and 2θ is the detector position with respect to the incident beam direction (figure 4.14 (b)).

4.4. Atomic Force Microscopy (AFM)

Atomic force microscopy is a versatile technique used to map and measure the surface morphology with extremely accurate spatial resolution [89]. Its development can be attributed to IBM researchers Binning, Quate and Gerber in 1986, when they created a new type of microscope that incorporated features of the scanning tunneling microscope (STM) and the profilometer [89]. The main advantage of this technique is based on the fact that almost any sample can be measured conductive or not, be it very hard, such as a dispersion of metallic nanoparticles, or very soft, such as individual molecules or biological structures [90].

Contrasting with others techniques such as optical or electron microscope where an image is formed by focusing light or electrons onto a surface, an AFM physically 'feels' the surface scanning the sample with a sharp probe, building up a map of the height of sample's surface [90]. In addition, the AFM does not require vacuum or liquid nitrogen and can be operated either at room temperature or under special conditions such as, for example, inert atmosphere and heating.

The fundamental principle of the AFM technique is the measurement of the atomic forces related to deflections of a support denominated cantilever under which a very sharp tip (typical radius of curvature is $5 - 10\ nm$) is coupled. The schematic of an AFM, showing the main components is shown in figure 4.15. A laser beam is focused on the

cantilever and reflected to a photosensitive detector which, in turn, captures the beam deflections arising from interactions between the tip and the sample surface during scanning. The data obtained are recorded and processed by the computer generating a bidimensional profile traced by the tip. It is important to note that the scanner responsible for the distance and relative movement between tip/sample is the piezoelectric device. This device undergoes nanometric displacements when a voltage is applied between its terminals, enabling a controlled point-to-point movement during the measurement.

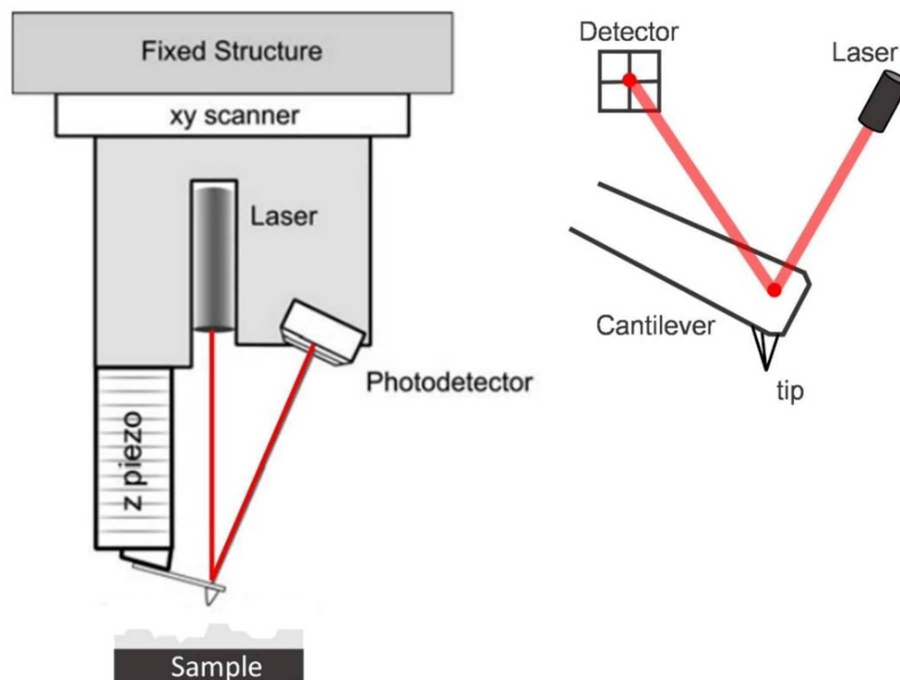

Figure 4.15: Schematic representation of an atomic force microscope. A laser beam is focused on the cantilever and reflected to a photosensitive detector which, in turn, captures the beam deflections arising from interactions between the tip and the sample surface during scanning. The cantilever is mounted on a piezo device and it moves under control of constant quantity (force, amplitude, frequency) feedback loop. Adapted from the reference [90].

The deformations result from the interaction forces between the probe and the sample. When the tip is approached to the sample, it is initially attracted to the surface as a function of van der Waals forces. As this approximation increases, the electronic orbitals of the sample and tip atoms begin to repel each other, decreasing the attractive force. When the distance between the atoms is of the order of angstroms, the force vanishes and it can

be said that, from then on, the atoms in the tip and in the sample are in “contact” and the repulsive forces dominate.

The image acquisition mode, called scans, are related to the distance between the tip and the sample during the measurement and with the manner in which the tip moves over the surface to be analyzed [90]. Images can be obtained by three basic modes of operation: contact, non-contact or semi-contact, depending on the net force between tip and specimen. When working in the region of attractive forces, the scanning method is called non-contact. Operation in the region of repulsive forces is called contact. In semi-contact mode, the operation takes place in both force regions. Figure 4.16 shows the relationship between the force between the tip and the sample and the distance between them. The modes to be used depend on factors such as the type of sample studied and the type of cantilever used.

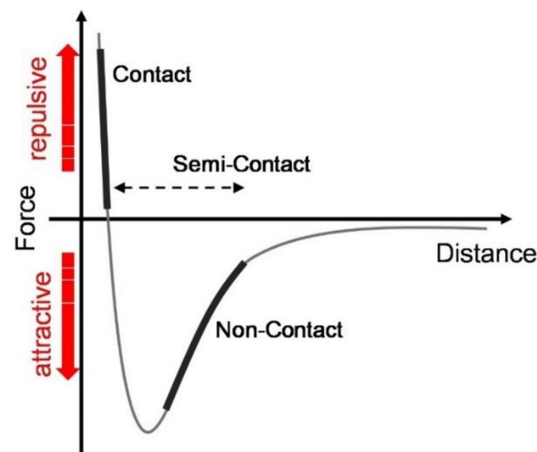

Figure 4.16: Interaction forces between tip and sample surface as a function of their distance.

In this work, the semi-contact or tapping mode was chosen. This mode has the advantage of minimizing possible damage to the sample surface and frictional forces when compared to the contact mode. During the scan the cantilever oscillates at a frequency close to its natural frequency, while the sample is swept. The tip is brought closer to the sample until it starts to make intermittent contact with the surface (the tip touches the sample surface only for a short periods of time), which causes a reduction in the oscillation amplitude, as shown in figure 4.17(a). Consequently, the reduced amplitude value activates

an electronic feedback mechanism, which will keep the reference oscillation amplitude constant by adjusting the z-piezo in order to move the cantilever probe up and down. Panel (b) represents how the z-piezo position values during scanning are used to reconstruct the topography creating the surface image. Finally, one must keep in mind that while the height resolution is intrinsically determined by the piezo steps (usually of the order of tens of picometers), lateral resolution is often restricted to probe sharpness (even if in-plane piezos can move in picometer steps), usually of the order of 1 - 10 nm.

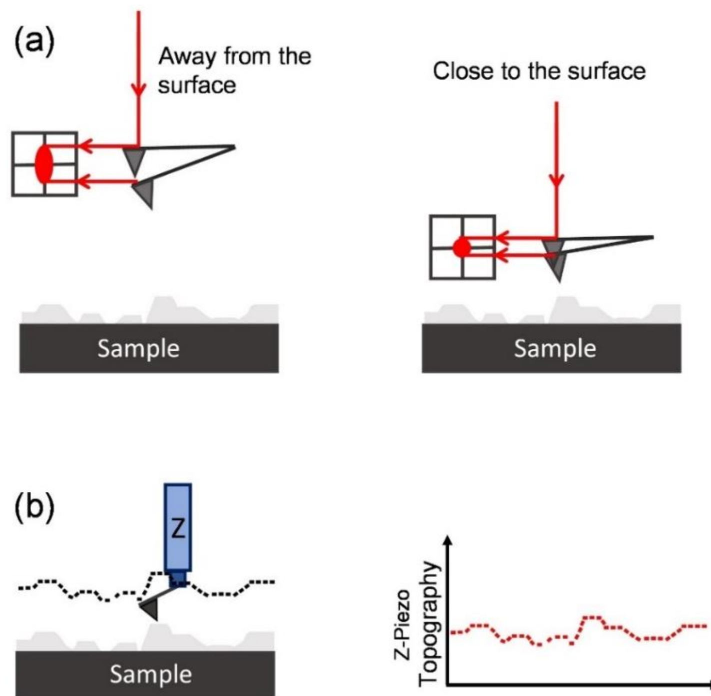

Figure 4.17: (a) In the tapping mode, tip is set to oscillate near to its natural resonance frequency and gets close to the surface until the oscillation amplitude became reduced to the smaller referential value. (b) The z-piezo adjusts, through a feedback system, the height axis to maintain the amplitude constant. The surface topography is reconstructed from those z values recorded by the piezo.

4.5. Scanning Tunneling Microscopy (STM)

The development of the scanning tunneling microscope is attributed to Gerd Binnig and Heinrich Rohrer in 1981 when they worked at the IBM Research Laboratories. It was the first technique that was able to generate real-space imagens of surfaces with atomic resolution [91]. Compared to AFM, the STM has limited applications due to the fact that requires electrically conductive samples. Despite this limitation, scanning tunneling

microscopy (STM) has become a powerful surface technique for realizing atomic scale analyses with much higher resolution than AFM [92].

The physical principle behind this technique is the establishment of a tunneling current between a sharp metallic tip and the sample of interest. Based on this, the fundamental concepts about quantum tunnelling can be understand modeling the system tip-sample as an one-dimensional rectangular barrier of height V_0, as shown in figure 4.18. Tip and sample are represented by the regions of potential equal to zero, since in them the electron can propagate as a free particle. The barrier symbolizes the distance between the sample and tip.

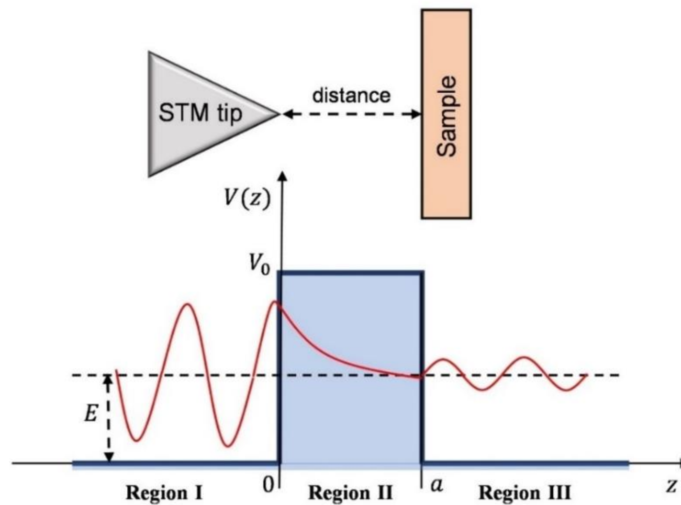

Figure 4.18: In a simplified view, the tip-sample system can be modeled as one-dimensional rectangular potential barrier of height V_0. Tip and sample are represented by the regions of potential equal to zero where the solutions of time independent Schrodinger equation are oscillatory. The barrier symbolizes the distance between the sample and tip where the solution shows an exponential decay.

Dividing the space into three regions and solving the time independent Schrödinger equation for a particle with energy $E < V_0$ moving from left to right is possible to show that the solutions consist of a linear combination of waves in both direction in each of the three regions, indeed:

$$\begin{aligned} \psi_{\mathrm{I}}(z) &= Ae^{i\beta z} + Be^{-i\beta z}, \qquad z \leq 0 \\ \psi_{\mathrm{II}}(z) &= Ce^{\kappa z} + De^{-\kappa z}, \quad 0 \leq z \leq a \\ \psi_{\mathrm{III}}(z) &= Fe^{i\beta z} + Ge^{-i\beta z}, \qquad z \geq a \end{aligned} \tag{4.16}$$

where $\beta = \frac{\sqrt{2mE}}{\hbar}$ and $\kappa = \frac{\sqrt{2m(V_0-E)}}{\hbar}$. The coefficients A, B, C, D and F are determined by the boundary conditions of the system. The coefficient G can be set to zero since the particle is moving from left to the right.

Hence, for regions I and III the solutions are of the oscillatory type. However, inside de barrier (region II) the solution decay exponentially. An important consequence of all this is that contrary to classical expectations which would suggest that the particle has zero probability of travelling beyond $z = 0$, quantum mechanics asserts that the particle has a finite probability of tunneling through the rectangular potential barrier, despite having a total energy less than V_0. Thereby, if the barrier is thin enough then wavefunction will not have decayed to zero when it reaches other side, and wave continues on for $z > a$.

Applying the boundary conditions, i.e., the continuity of wave function $\psi(z)$ and its first derivative at $z = 0$ and $z = a$, the coefficients of equations 4.16 can be determined. The four equations that allows relating the coefficients are:

$$\begin{aligned} A + B &= C + D \\ i\beta(A - B) &= \kappa(C - D) \\ Fe^{i\beta a} &= Ce^{\kappa a} + De^{-\kappa a} \\ i\beta Fe^{i\beta a} &= \kappa(Ce^{\kappa a} - De^{-\kappa a}) \end{aligned} \tag{4.17}$$

The fraction of particle incident on the barrier which are transmitted can be found by the ratio between coefficients F and A. Thus, solving the equations 4.17 for F in relation to A, the transmission coefficient T, after some algebra, can be written [93]:

$$T = \frac{|F|^2}{|A|^2} = \left\{1 + \frac{{V_0}^2[senh(\kappa a)]^2}{4E(V_0-E)}\right\}^{-1} \tag{4.18}$$

In limit where $\kappa a \gg 1$, T can be simplified as:

$$T = \left[\frac{4E(V_0-E)}{{V_0}^2}\right] e^{-2\kappa a} \tag{4.19}$$

This equation indicates that the probability to observe tunneling depends on the intensity of the potential energy V_0 and the width of the barrier a. However, as mentioned, the rectangular potential barrier is modelling the situation of an electron tunneling through vacuum from the tip to de sample or vice and versa. Therefore, the

exponential attenuation within the barrier is the key element of STM. This exponential dependence allows adjusting the tip-sample distance with a very accuracy making it possible to achieve atomic resolution.

4.5.1. Measurement setup

The scanning tunneling microscope is designed in order to register the quantum tunneling events by bringing a sharp conducting tip (usually made of W or Pt-Ir alloy) in a close proximity with a conducting surface (typically few angstroms). In a typical STM system, an atomically thin conducting tip is supported by scanners. Similarly, to AFM, these scanners are made from a piezoelectric material that expands and contracts proportionally to an applied bias voltage suffering well-behaved sub nanometric deformations to move the tip in relation to the sample along the lateral directions (x and y), and also vertical (z) position. Additionally, the sample is placed on a stage supported by springs to avoid mechanical vibrations. A schematic illustration is show in figure 4.19.

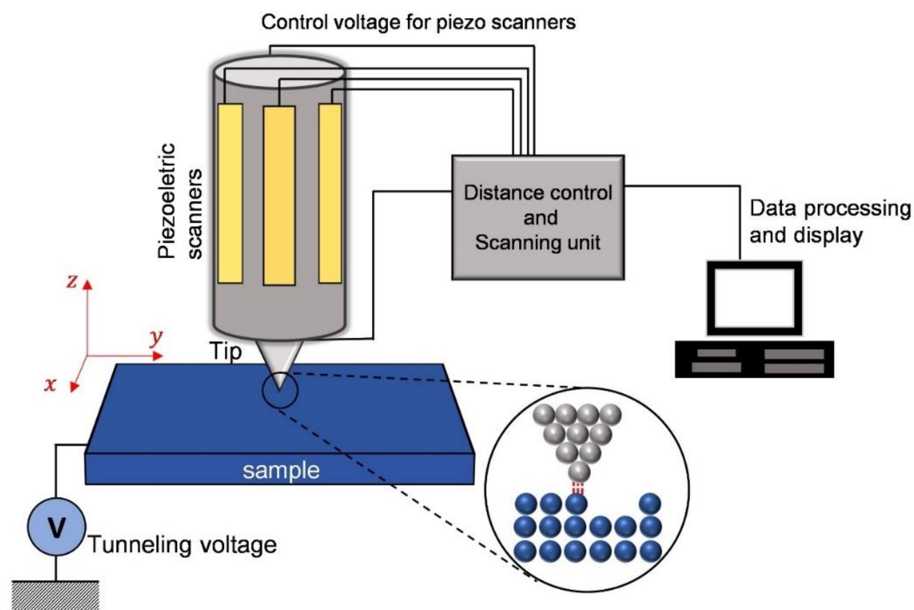

Figure 4.19: Basic scheme of working principles of a scanning tunneling microscope. In a typical STM system, an atomically thin conducting tip is supported by scanners. These scanners are made from a piezoelectric material that expands and contracts proportionally to an applied bias voltage suffering well-behaved sub nanometric deformations to move the tip in relation to the sample along the lateral directions (x and y), and also vertical (z) position. The figure is adapted from Ref. [94].

Approaching the tip close enough to the sample surface, but not allowing contact between them, i.e., ohmic contact, an externally bias voltages between these two objects is applied in order to enable a tunneling current flowing through the system. Initially, the system is grounded so that the tip is at the same voltage as the sample. Thus, applying a positive voltage V to the sample while the tip is maintained grounded, the electrons will tunnel from the occupied states of the tip to the unoccupied states of the sample. On the other hand, if $V < 0$ tunneling is reversed, the electrons from the occupied states of the sample migrate to the unoccupied states of the tip.

Once the tunnelling current has been stablished, the most common mode to image the sample surface is set a reference value for the current (constant current operation mode) and during the scan, the distance between the tip and the sample surface will be controlled through a feedback system in order to maintain this value. As represented in figure 4.20, the topography of this surface is constructed by recording the movements of the z piezoelectric element at each position (x, y) of the analyzed area.

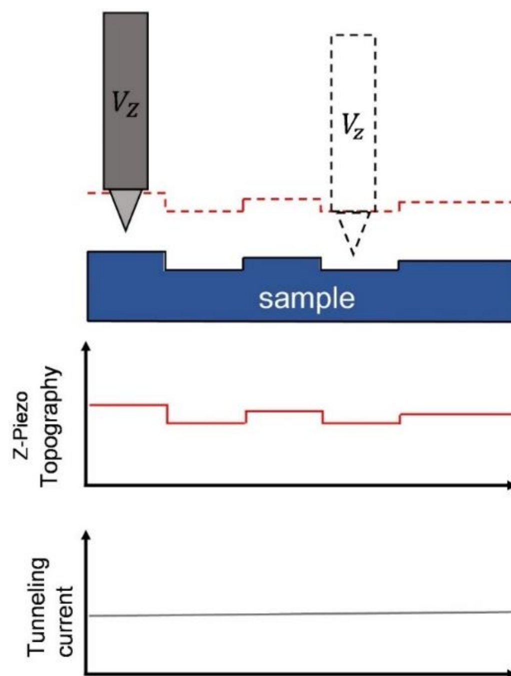

Figure 4.20: Schematic representation of constant current mode. During STM measurement, the tunneling current is set in a determined value and z-piezo adjust the distance to the sample surface in order to hold the current value. The topography of this surface is constructed by recording the movements of the z piezoelectric element at each position (x, y).

As depicted in equation 4.19, the electron tunnelling scales exponentially with the barrier width, and thus with the tip-sample distant. Consequently, the tunneling current is very sensitive to height variations at the surface, for instance, if the tunneling current exceeds the reference value, the feedback system connected to the z piezoelectric scanner will increase the distance between the tip and the sample surface, decreasing the tunneling current. Now, if the detected tunneling current is less than the reference value, the feedback system will bring the tip closer to the sample, increasing the tunneling current.

4.5.2. Scanning Tunneling Spectroscopy (STS)

As introduced in the previous section, depending on the polarity of the applied voltage V to the sample (positive or negative, respectively), the direction of the tunneling current can be changed. This property can be used to probe the local state density of the sample (LDOS). In this case, tunneling current can be used as a spectroscopy technique known as scanning tunneling spectroscopy (STS).

The tunneling current can be calculated with a more sophisticated approach based on time-dependent perturbation theory, in this approach the tunneling current is represented in terms of integral over the energies of the involved tip and sample states [95-97], yielding

$$I(V) \propto \int_{-\infty}^{\infty} [f(E_F^S - eV + \varepsilon) - f(E_F^T + \varepsilon)] \rho_T(E_F^T + \varepsilon) \rho_S(E_F^S - eV + \varepsilon) \mid M \mid^2 d\varepsilon, \quad (4.20)$$

in this equation, $\mid M \mid^2$ is the matrix element for tunneling across the barrier, ρ_T, E_F^T and ρ_S, E_F^S are the local density of states and Fermi energy of the STM tip and sample respectively and $f(\varepsilon)$ is the Fermi-Dirac distribution.

A first simplification in equation 4.20 can be done considering that for measurements at room temperature $(k_B T \propto 0.025\, eV)$ and below the Fermi-Dirac distribution can be approximated for the step function. In this way we will have:

$$I(V) \propto \int_0^{eV} \rho_T(E_F^T + \varepsilon) \rho_S(E_F^S - eV + \varepsilon) \mid M \mid^2 d\varepsilon. \quad (4.21)$$

A second simplification can be made based on Bardeen theory of tunneling [97]. He showed that under the real conditions, the matrix element for tunneling $\mid M \mid^2$ is independent of the energy difference between the two sides of the barrier. Indeed, it is

possible to show that $| M |^2 \propto e^{-2\kappa a}$, recovering the exponential dependence on the distance a between the tip and the sample [95], κ is a factor associate with the work functions ϕ of the tip and sample materials. Therefore, it is reasonable take it as a constant in the tunneling theory [97]. Finally, it is possible to choose a tip material which has a relatively flat LDOS that does not change appreciably in energy, so that ρ_T can be treated as a constant and taken out of the integral. In summary, the tunneling current can be reduced to:

$$I(V) \propto \int_0^{eV} \rho_S(E_F^S - eV + \varepsilon)\, d\varepsilon. \tag{4.22}$$

This result shows that the tunneling current is strongly affected by the density of states of the sample at the Fermi level and a qualitatively description of this can be found in figure 4.21 that represents the energy diagrams for different conditions of tunneling between STM tip and sample surface. Panel (a) shows a situation where tip and sample are close enough to allow a tunneling current, but there is no externally applied bias voltage V, the tip-to-sample and the sample-to-tip tunneling probability are the same which results in zero tunneling current flow. Consequently, the Fermi levels of the tip (E_F^T) and sample (E_F^S) are aligned. In contrast, panels (b) and (c) depict the case when an external bias voltage V is applied between the sample and tip, a tunneling current will flow through the vacuum barrier between them and the sample Fermi level will be shifted either downward or upward with respect to the tip Fermi level depending on the polarity of the applied voltage V to the sample. Because of this shift, electrons tunnel in an energy range $[E_F^S, E_F^S + eV\,]$ either from the filled states of the tip to empty states of the sample or from filled states of the sample to the empty states of the tip.

Hence, by varying the bias, the tunneling current becomes a measure of local density states of the sample at a fixed position of the tip. This can be evidenced taking the derivative of the equation 4.22 as a function of the bias voltage, defining the differential conductance [95]:

$$\left.\frac{dI}{dV}\right|_{V=V_{bias}} \propto LDOS_{sample}(E_F^S). \tag{4.23}$$

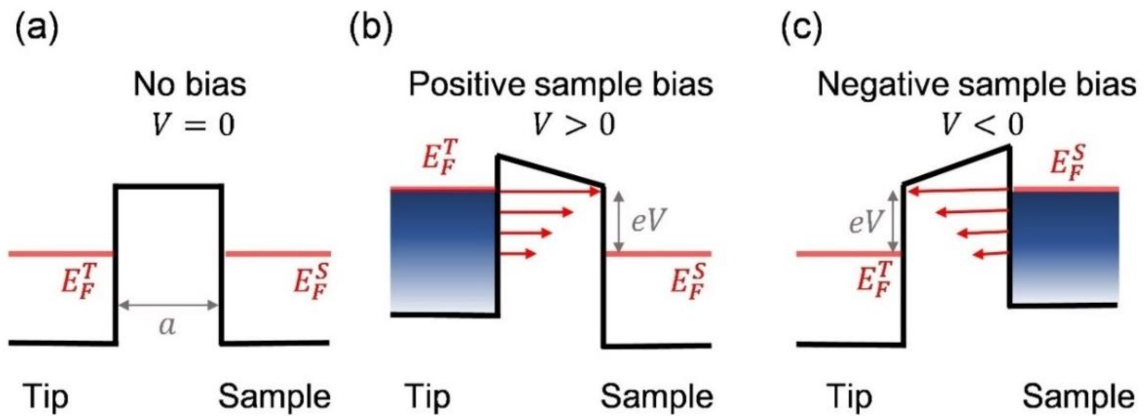

Figure 4.21: Energy diagrams for different conditions of tunneling between STM tip and sample surface. (a) Tip close to sample (within tunneling distance) but no bias ($V = 0$), Fermi level aligned and zero current flow. (b) Sample positively biased ($V > 0$), eletrons from tip tunnel to empty states of sample. (c) Sample negatively biased ($V < 0$), eletrons from occupied states of sample tunnel to tip.

In general, spectroscopic measurements are performed by positioning the STM tip in the region of interest, the feedback system is turned off in order to keep the tip-sample distance fixed. Thereafter, by changing the applied voltage, for example, in the interval $[-V_0, V_0]$ the corresponding variations in the tunneling current are registered. In practice, a lock-in amplifier can be used to measure $\mathrm{d}I/\mathrm{d}V$ directly. A voltage modulation $\mathrm{d}V$ is applied to the bias, and a resulting response in current modulation $\mathrm{d}I$ is measured at the same frequency.

Although some approximations have been made to obtain the equation 4.22, it is important to note that during an STS measurement we are measuring a quantity that is locally proportional to the density of states of the sample and, then, can be used to study the electronic properties of different systems. As an example, in figure 4.22 we shown schematically how the current and dI/dV-signal varies as a function of the applied voltage for different type of materials. As well stablished in solid states physics, conductors do not possess an energy gap between the occupied states (valence band) and the unoccupied states (conduction band) and the variation in LDOS is relatively small. Thus, resulting in a very small dI/dV variation. Otherwise, for semiconductors and insulators, the conductance around the Fermi level is zero due to presence of energy band gap. In these materials, the threshold voltage can be used to determine the band gap, i.e., $E_g = |V_{+\,bias}| + |V_{-\,bias}|$,

with $V_{\pm\ bias}$ representing the bias voltage points where the conductance returns to grow after the plateau [98].

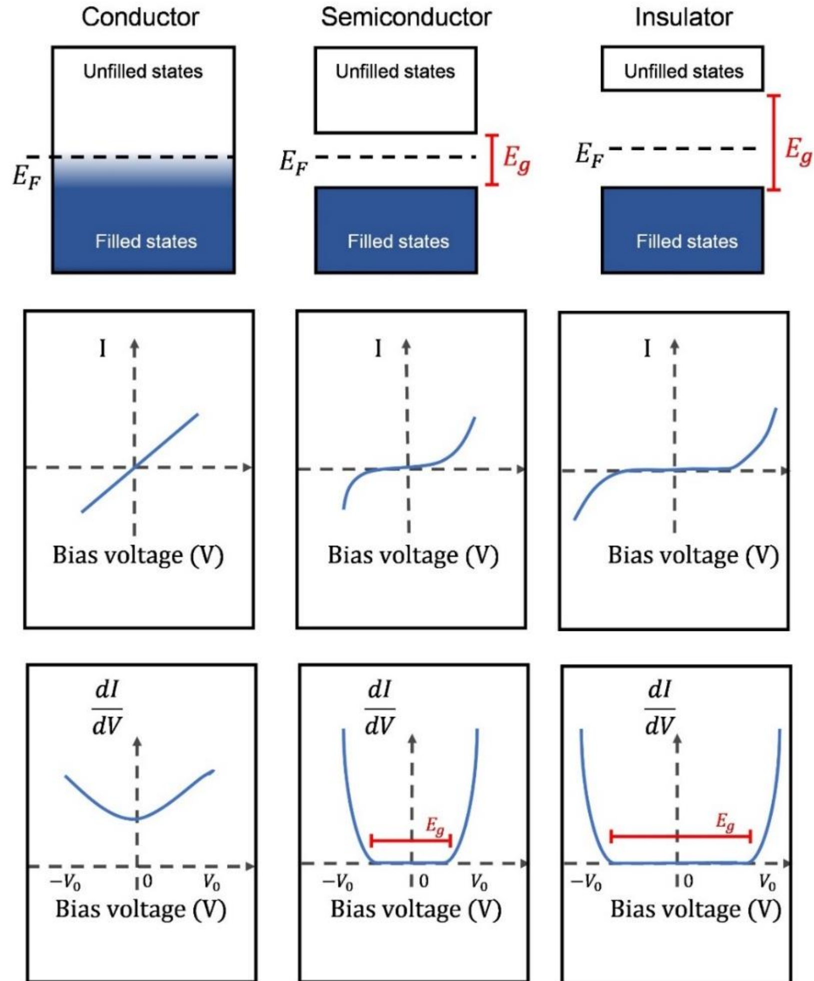

Figure 4.22: Electronic structure and corresponding I/V and dI/dV-signal for conductors, semiconductors and insulator materials. The regions that corresponds $V > 0$ is probing the empty states (conduction band) and the regions that corresponds $V < 0$ is probing filled states (valence band). The zero delimits the Fermi levels. The figure is adapted from Ref. [98].

5. Structural properties of SiGe layers after Ge-condensation technique

5.1. Introduction

Integrated circuit (IC) construction technology has evolved since the 1960s, when it was implemented on an industrial scale. Since then, finding materials that allows one to reduce cost and energy consumption, while increasing processing speed and complexity of ICs is a major goal of all semiconductor industry. The improvement of such parameters results from the ability to reduce device dimensions, scaling down ICs and field-effect transistor technology devices such as metal-oxide-semiconductor transistors (MOSFET) [99]. Although Silicon remains the broadly used, the interaction between transistors and Si substrates introduces a series of parasitic effects [100]. In this scenario, several studies and propositions concerning device processing were established in order to minimize these effects, replacing conventional Si-bulk planar technology [101]. Among them, SOI (Silicon on Insulator) [102] and SGOI (Silicon-Germanium on insulator) [103] technology has attracted industrial attention.

In particular, Silicon-Germanium-on insulator technology refers to the use of a layered thin SiGe-insulator-silicon substrate in place of a conventional bare Si substrate [103]. The presence of a buried oxide allows for better current control and lower power dissipation [103]. Besides that, thin SiGe layers on insulator can be used as a growth template for creating a thin Si layer under strain that offers improved charge carrier transport properties compared to unstrained Si layers [104-106]. Therefore, the growth of SGOI layers with low defect concentration and controlled composition/strain is a key process for future MOSFET devices.

In order to obtain high quality SGOI substrates, the almost 4% of lattice mismatch between silicon and germanium has to be overcome. Since the growth of SiGe layer with high Ge content inevitably introduces interfacial defects that affects devices

performance, Ge condensation processes emerge as a promising technique for SGOI production [105]. Particular interest must be devoted to strain conditions of these layers. Semiconductor systems are known to present a plethora of properties that are modified under elastic strain. Among these properties are, e.g., effective carrier mass [107-109], direct/indirect bandgap condition [110, 111], carrier mobility [112-114], optical excitation selection rules [115] and band alignment [116]. The ability to fine tune the built-in strain is, in this case, highly desirable.

In Ge condensation processes a thin SiGe layer with low Ge concentration and calibrated thickness is epitaxially deposited on top of a Si template (either a thick substrate or a layered system). If annealed in an oxidizing environment [105, 117] the favorable formation enthalpy of Si-oxide with respect to Ge-oxide becomes the driving force for in-depth Ge segregation, while Si atoms remain at the surface forming a reaction interface with the oxygen. As a result, the crystalline SiGe layer becomes thinner and more Ge-rich.

Although previous studies have quantified the Ge fraction in SiGe layers [105, 117, 118], the compositional profile has not been accurately correlated to the strain distribution along the in-plane and the out-of-plane (growth) directions. The precise knowledge of in-plane and out-of-plane strain components allows a better understanding of defect nucleation at the layer interface or after to chemical processing if the insulator layer is removed. It also provides evidences of pseudomorphic relaxation, which indicates the presence of dislocations and is of crucial relevance for electronic band properties that impact on applications.

In this chapter, we combine x-ray diffraction (XRD), x-ray reflectivity (XRR), ultra-low-energy secondary ion mass spectroscopy (ULE-SIMS), Scanning Electron Microscopy (SEM) and rolled-up nanotech [119-122] to correlate compositional and strain profiles in SGOI obtained via different oxidation processes. Our results show that a monotonic increase of the average Ge content in the SGOI film at increasing oxidation time is not accompanied by an increase in both in-plane and out-of-plane strain. The description provided here can open up potential applications where Ge concentration gradient must be maximized, surface

oxidation with Ge losses must be avoided and in-plane or out-of-plane strain must be tuned to achieve specific lattice conditions.

5.2. Methods

All samples analyzed in this chapter were provided by Dr. Francesca Cavallo. The fabrication of SGOI layers began with solid-source molecular beam epitaxy of $Si_{(1-x)}Ge_x$ layers with low Ge concentration on commercially available Silicon-on-Insulator (SOI) substrates, as shown schematically in Fig. 5.1. The as-grown $Si_{(1-x)}Ge_x$ layer were 100 nm thick and had a nominal (calibrated) Ge fraction of 0.08. The growth temperature was 350 °C. Next $Si_{0.92}Ge_{0.08}$ layers underwent dry thermal oxidation at 900°C with different oxidation times (6 to 10h in 1h steps). The thermally grown SiO_2 was then removed by etching in a hydrofluoric acid and water solution HF (49%): H_2O with 1:1 volume]. These samples were then characterized by X-ray diffraction, X-ray reflectivity and ULE-SIMS.

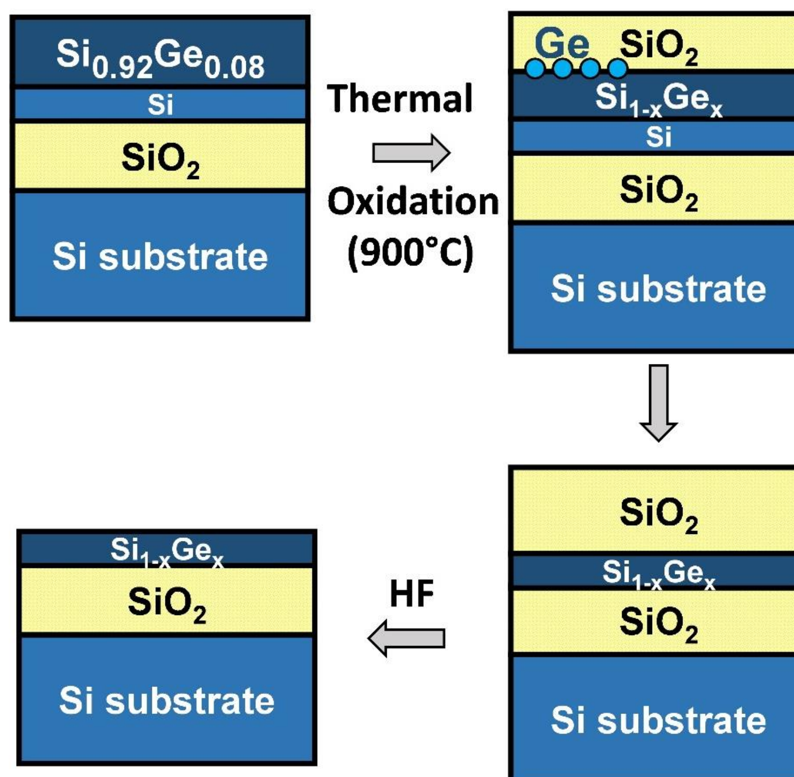

Figure 5.1: Simplified sketch of Ge condensation procedure used to obtain a Ge-rich layer from a starting $Si_{(1-x)}Ge_x$ MBE-grown layer.

X-ray measurements were performed in selected samples using coplanar, anomalous and grazing incidence XRD by Prof. Dr. Ângelo Malachias. XRD and XRR were carried out at the ID01 beamline of the European Synchrotron Light Source, with fixed energies of 11.005 keV (λ = 1.1266 Å) and 11.103 keV (λ = 1.1167 Å). The latter energy was used in XRD to extract the Ge content by anomalous diffraction contrast evaluation [see, e.g., Magalhães-Paniago *et al*. Ref. [123]]. The average Ge content and thickness of SiGe layers during the oxidation were determined using the *X-ray utilities package* [124] to simulate XRD. XRR fits used the Parratt [125] formalism and the algorithm available at Ref. [126].

Finally, ultra-low energy ULE-SIMS data was performed in order to monitor the Ge concentration in SiGe oxidized layers. In this work Cs^+ primary ions with energy in the range of 500-900 eV are used to measure chemical profiles with a 0.2 nm depth resolution. The measurements were performed by Dr. Francesca Cavallo.

The strain profile in the fabricated SGOI layers was also investigated using the rolled-up nanotech. For this purpose, rolled-up tubes were produced using the methods described in Cavallo *et al.* [122]. Briefly linear trenches were obtained by mechanical scratching along the [010] direction to provide access of an etching solution to the buried SiO_2 layer. Next, an HF (49%): H_2O (1:1) solution was used to selectively remove the SiO_2, allowing the upper SiGe layers to roll or wrinkle according to their built-in strain [122]. The morphologies of released and hinged layers were confirmed by optical microscopy. Tube radii at exposed openings were measured for a minimum of 15 tubes for each sample by off-axis SEM.

5.3. Results

5.3.1. Ultra-low Energy Secondary Ion Mass spectroscopy

The depth profiles extracted by ULE-SIMS from the as-grown sample, as well as for samples oxidized for 6, 7, 8 and 10 h are shown in Fig. 5.2(a). In the oxidized samples, a rapidly increase of Ge fraction compared to initial values from the as-grown SiGe layer was observed. The Ge content is higher at the thermally grown oxide/SiGe interface and

decreases monotonically toward the SiGe/buried oxide interface. The Ge concentration gradient becomes smaller as the oxidation time increases from 6 h to 8 h, and a more uniform (less graded) profile is obtained after a 10 h-long oxidation process. This behavior is expected in Ge condensation phenomena, that comprises an initial enrichment of Ge atoms under the surface topmost SiO_2 layer, followed by bulk diffusion of Ge toward the buried oxide layer [105, 118].

Figure 5.2(b) shows the thickness of SiGe layer obtained from ULE-SIMS profile as a function of oxidation time. At this point, the onset of oxygen concentration is used to define the insulator-substrate interface position as well as the out-of-plane position of the oxidized upper layer interface. As observed, a systematic thinning of the SGOI layer occurs as the oxidation time increases.

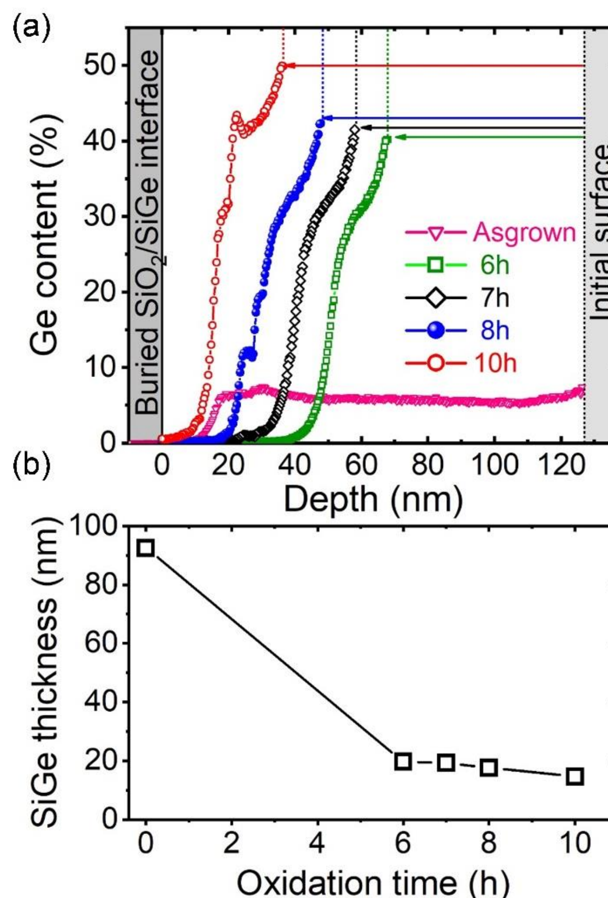

Figure 5.2: (a) Measured Ge concentration using ULE-SIMS for the as-grown MBE layer and samples retrieved after 6h, 7h, 8h and 10h of thermal oxidation. (b) Layer thickness of the SiGe thin film extracted from ULE-SIMS measurements, exhibiting different values as a function of oxidation time.

In figure 5.3, the total amount of Ge atoms in SiGe layer obtained by integrating the ULE-SIMS profile and normalized by the initial Ge volume prior to the oxidation is represented as a function of oxidation time. As observed, the total amount is constant for all oxidation times (error bars are proportional to dot size in this graph). This result confirms that the thermal growth oxide as well as the buried oxide acts as barriers for Ge oxidation (or diffusion towards the oxide layer), preventing the loss of Ge during the oxidation process [105, 118, 122].

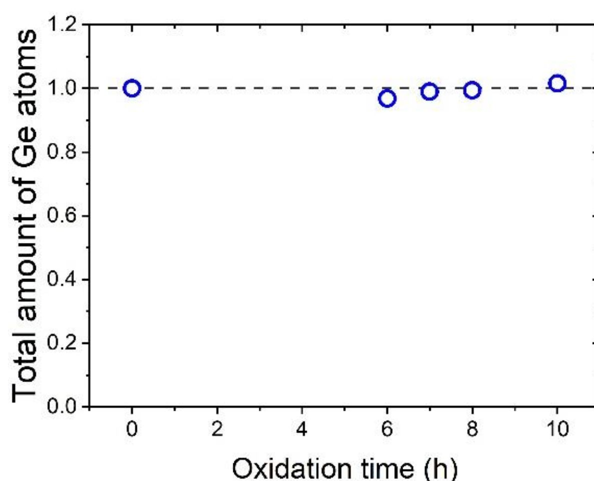

Figure 5.3: Calculated Ge content using the ULE- SIMS profile as reference for computing the total Ge volume and the ULE-SIMS layer thickness from the depth of 0 nm (SiO_2 interface) up to the last detectable ULE-SIMS point of panel (b) as total layer thickness for each oxidation time.

5.3.2. X-ray diffraction

Figure 5.4 shows a specular (θ-2θ) XRD scan in the vicinity of the Si (004) reflection for the oxidized layer. The result is expressed as a function of the longitudinal momentum transfer vector in the out-of-plane direction $q_z = 4\pi/\lambda \sin(2\theta/2)$, where λ is the wavelength and 2θ the scattering angle. For all samples, the Si-substrate peak was suppressed from measurements (blue dots) by a very small tilt (~0.01°) along the surface parallel to the momentum transfer direction (q_y), improving the visibility of the diffuse diffraction from the SiGe film above the SiO_2 layer.

The substrate and the SiGe layers give rise to peaks at 4.631 $Å^{-1}$ and between 4.539 and 4.528 $Å^{-1}$, respectively. The slight shift of the SiGe reflection with respect to the Si substrate reflection is attributed to out-of-plane strain in the SiGe layer. The effect of Ge-

enrichment is evidenced from the gradual shift of the (004) SiGe peak relative to Si substrate. For the sample oxidized during 10 h the SiGe layer peak shifts towards lower values of q_z (away from the Si peak position). This peak shifting reflects the fact that the SiGe lattice parameter increases systematically with this oxidation time and consequently the resulting Ge composition. On the other hand, for samples oxidized between 6h and 8h, although a progressive increase of the Ge content is observed, the (004) SiGe peak shifts towards large q_z values, indicating an existence of non-monotonic lattice strain. Additionally, interference fringes can be observed for all samples indicating a good crystal quality of the layers even after oxidation.

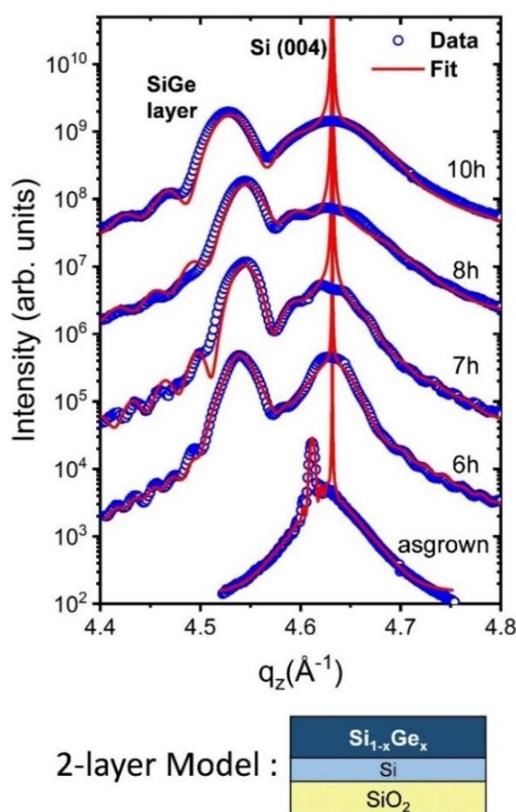

Figure 5.4: (a) X-ray diffraction measurements in the vicinity of the Si (004) reflection for all measured samples. The very sharp Si substrate peak was suppressed from measurements (blue dots) by a very small tilt (~0.01°) along the surface parallel momentum transfer direction, improving the visibility of the diffuse diffraction form the SiGe film above the SiO_2 layer. Semikinematical simulations (red solid lines) using a simplified 2-layer stack, shown schematically in the inset, with a Ge-rich region and a Si-pure region were used to extract the average Ge.

In figure 5.4, the red solid lines represent semi-kinematical simulations obtained assuming a model of 2-layer stack with a Ge-rich region and a Si-pure region, schematically

illustrated in the inset. The 2-layer model was preferred here since a model based on the full Ge concentration profile would require an estimation of the unknown in-depth strain profile, bringing additional complexity to the fitting procedure. The thickness oscillations observed for low-q_z values in the vicinity of the SiGe layer peaks for all samples indicate that only a mild lattice parameter gradient is expected within these layer (coexistence among different lattice parameters would suppress these oscillations). The SiGe/Si bilayer model used to fit the XRD data provided Ge concentrations of 7%, 29%, 30%, 31% and 35% at 0 h, 6 h, 7 h, 8 h and 10 h oxidation time, respectively. Error bars for these concentrations were found to be of the order of 2% for oxidized samples and 1% for the non-oxidized (0 h) SiGe layer.

A direct evidence of the high Ge content in the SiGe layer is provided in Fig. 5.5, where the diffraction intensity at 11.005 keV is compared to the diffraction retrieved at the Ge-K edge (11.103keV) for the sample with 8 h oxidation time. A Ge-content of 0.38 ± 0.04 is extracted from this result following the procedure outlined in Magalhães-Paniago *et al*. Ref. [123]. Such amount of Ge is in agreement with the Ge content of the SiGe layer obtained by ULE-SIMS, indicating that possible deviations between both techniques would be of the order of 5 %.

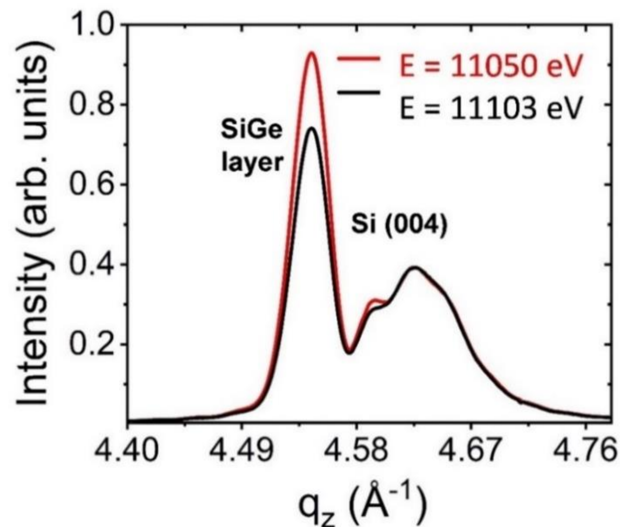

Figure 5.5: Anomalous (resonant) x-ray diffraction carried out at the 8h oxidation layer, showing a contrast at the SiGe peak due to the large amount of Ge atoms present in this layer. A small contrast is also observed at the diffuse diffraction near the Si (004) peak position, indicating that a limited amount of Ge atoms can diffuse into the Si layer without the appearance of considerable strain.

The oxidized samples were also measured in grazing incident diffraction geometry (GID) with a fixed photon energy of 11.005 keV, as depicted in Fig. 5.6. Since layer thickness varies and penetration depth is maximized at the upper SiGe layer signal the Si substrate diffraction peak (buried by the SiO_2 layer) shows up with variable intensity, sometimes not distinguishable from the SiGe peak. Based on this fact, peak positions were evaluated by Lorentzian fits in order to distinguish the scattering contribution from the SiGe layer and Si substrate.

Figure 5.6 shows a longitudinal (radial) scan in the vicinity of the in-plane Si (400) reflection for samples oxidized for 6, 8 and 10 h. The red solid line shows the sum of the Lorentzian profiles, in good agreement with the measured data. Increasing the oxidation time shifts the SiGe diffraction peaks towards lower $q_{//}$ values, meaning larger in-plane lattice parameters. This behavior is more remarkable in the sample oxidized for 10 h where a clear separation of SiGe layer peak and Si peak is retrieved. These results suggest an in-plane lattice expansion into the SiGe layers as the oxidation time and consequently Ge concentration increases.

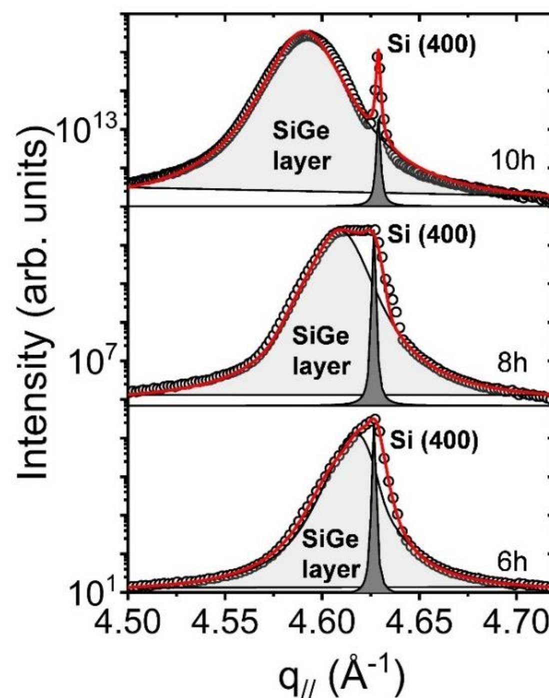

Figure 5.6: Grazing incidence x-ray diffraction in the vicinity of Si (400) substrate for different oxidation times. Two Lorentzian curves were fitted in order to extract the SiGe layer and Si substrate peak positions. Individual fits for each layer are shown with the superimposed resultant fit (red curve) indicating a good agreement with experimental data.

From the (400) diffraction peak positions we were able to extract the in-plane lattice parameter of SiGe layers and consequently calculate the in-plane and out-of-plane strain of the SiGe layers, reported in Table 5.1. As seen in this table, the largest in-plane strains (-0.70%) are measured at the samples oxidized for 6 hours, while the out-of-plane strain remains roughly at the same value between 0.5-0.9%. One notices for all samples a compressive in-plane strain (Ge-rich layer biaxially strained to the Si lattice parameter) with a tensile out-of-plane strain due to pseudomorphic relaxation. Grazing-incidence measurements were not carried out at the 7 h sample, where an average Ge concentration value between the 6h and 8h samples was assumed in order to retrieve the out-of-plane strain.

Table 5.1: Average in-plane and out-of-plane strain status for all measured layers, extracted from the peak position of the SiGe layer retrieved from XRD measurements of the (004) reflection [Fig. 5.4] and the (400) reflection [Fig. 5.6].

Oxidation time	In plane strain (%)	Out-of-plane strain (%)
As grown	-0.25(3)	0.10(3)
6 hours	-0.70(4)	0.79(3)
7 hours	--	0.67(3)
8 hours	-0.58(4)	0.65(3)
10 hours	- 0.53(4)	0.90(3)

Source: Elaborated by the author.

5.3.3. X-ray reflectivity

Although out-of-plane diffraction results provide a clear overview of the Ge content in the SiGe layers, which remains crystalline, the question remains whether amorphous material is generated by the Ge condensation process. In order to answer this question, XRR were carried out, providing an electronic density profile throughout simulations. Contrarily to the XRD measurements, where a lattice parameter (and consequently strain) profile is expected to have an interplay with the Ge distribution along the layer, XRR measurements can be interpreted using the ULE-SIMS data as starting conditions. In order to introduce the ULE-SIMS profile, we depict it as a series of stacked layers with 1 nm thickness, each one with the retrieved Ge concentration. For the fits of Fig.

5.7 a simple but sensitive correction was applied to the ULE-SIMS profile in the form of a multiplicative constant. The value of 1.15, was used for the whole sample series, showing that a variation of 10% Ge concentration was retrieved. Ge average concentrations (in the Ge-rich layer) of 8%, 27%, 30%, 36% and 48% were retrieved from XRR analysis for the non-oxidized (as grown), 6 h, 7 h, 8 h and 10 h oxidation time, respectively.

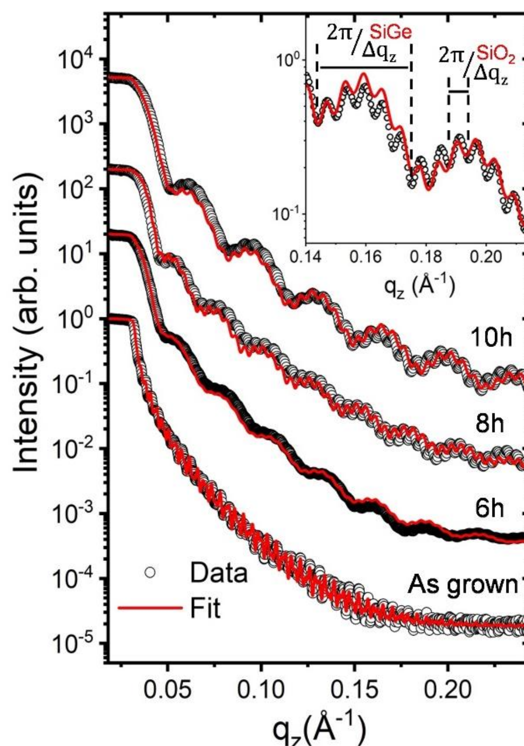

Figure 5.7. X-ray reflectivity measurements (black dots) in the as-grown, 6h, 8h and 10h oxidation time samples. Simulations using the Parratt model are depicted by red solid lines for all curves. In these simulations the short-period oscillations arise from the SiO_2 layer underneath the SiGe film. Long-period oscillations arise due to the presence of the Ge-rich layer, which becomes thinner as the oxidation time varies from 6h to 10h (larger oscillation periods are observed as oxidation time increases). The larger Ge content is qualitatively observed from the increase of oscillation contrast (more pronounced maxima and minima) as well as from the increase of critical q-value for total external reflection (flat portion at the top of the curves). The inset shows a detailed view of XRR curve for the sample with 10h oxidation evidencing the long and short-period oscillations that arises from the SiO_2 and Ge-rich layer, respectively. The thickness of each layer can be obtained from $2\pi/\Delta q_z$.

5.4. Discussion

A comparison between ULE-SIMS, XRD and XRR results is provided in table 5.2. We observe that the SiGe layer thickness extracted from ULE-SIMS data is larger than from other methods, while the thickness obtained from XRD is the lowest one. Such difference

can be ascribed to the fact that XRD is only sensitive to the crystalline layer volume, while ULE-SIMS and XRR probe atomic concentration and electron density variations, respectively. Particularly, the difference of XRR and XRD can be ascribed to the formation of an amorphous oxide layer with large Ge content, indicating that after a given concentration threshold a fraction of the Ge atoms in the topmost layers oxidize with Si, forming an $Si_{(1-x)}Ge_xO_2$ oxide.

Table 5.2: Comparison between the thickness of SiGe layer obtained from ULE-SIMS, XRR and XRD techniques.

Oxidation time	Thickness SIMS (nm)	Thickness XRR (nm)	Thickness XRD (nm)
As grown	110(2)	103(10)	92(2)
6 hours	28(2)	26(3)	20(1)
7 hours	26(2)	24(3)	19(1)
8 hours	17(2)	20(2)	17(1)
10 hours	16(2)	19(2)	14(1)

Source: Elaborated by the author.

The Ge concentration retrieved by each method is depicted in Fig. 5.8. In this figure the upper limit represented by the solid black line is calculated by assuming the nominal (growth) 8% Ge concentration in the SiGe layer and a complete diffusion of Ge towards the SiGe layer (ruling out completely the possible formation of oxides with Ge atoms). The total Ge-volume is then ascribed to the SiGe layer formed after the oxidation process with the thickness obtained by XRD.

We find from Fig. 5.8 that for the initial SiGe film as well as for the shortest oxidation time the values extracted from all techniques exhibit a similar trend, indicating that Ge is being pushed towards the SiGe layer, which remains crystalline. For 7 h oxidation and above the relative amount of crystalline material seems to decrease (red XRD curve), as part of the material becomes amorphous. It is worth noticing that the Ge concentration from ULE-SIMS follows the trend of the XRR, misplaced by a factor of 0.25 (25%), reinforcing the distinction between XRD and XRR results. The XRR difference to the estimated upper limit of Ge-concentration also increases for 8 h and 10 h, indicating that a small fraction of Ge may either oxidize, forming a low-Ge content $Si_{(1-x)}Ge_xO_2$, or become amorphous. These results

suggest, indirectly, that the interface between the remaining SiGe layer and the pure SiO_2 oxide topmost layer formed along the Ge condensation process may be amorphous or partially amorphous, with a considerable Ge-content. The formation of an amorphized or oxidized SiGe layer is thoroughly discussed in references [127-129]. It is shown that amorphization is more likely to occur for temperatures near 950°C, while oxidation of a SiGe alloy is more likely to take place near 1050°C. Here we cannot directly distinguish between both possibilities due to the reduced thickness of such interface (references mentioned above use a much shorter oxidation time, restricting diffusion/oxidation). From ULE-SIMS measurements we estimate that Ge atoms do not enter the oxide layer deeper than few nm.

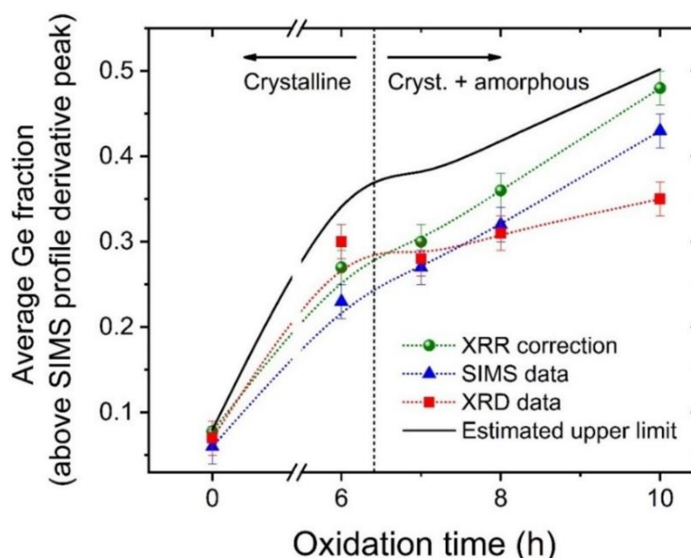

Figure 5.8: Comparison of the average Ge fraction obtained by each experimental method used in this work for all measured samples. The black solid line represents the upper limit estimation of the Ge concentration. The dotted lines serve as a guide to the eyes for the results of each technique, showing how the information extracted from them is related.

The results of Fig. 5.8 point out to the existence of ~ 3 nm interface with SiGe oxide/amorphous layer with a Ge concentration that ranges from the XRR concentration (upper limit) to the XRD concentration (lower limit).

A final evidence of the correct Ge-concentration and strain status retrieved for the crystalline regions of the layers can be outlined by rolling them up as explored in Cavallo *et al* [122]. The strain model from Refs. [130- 132] was used here assuming only 2 layers (as in the XRD analysis), one with pure Si and other with $Si_{(1-x)}Ge_x$ concentration, the elastic

constants of SiGe were determined according to the equation (3.4) shown in section 3.1.2. SEM images of selected tubes formed from the samples oxidized along 6 h and 8 h are depicted in Fig. 5.9 (a) and (b), respectively. The experimental inner radii of these tubes (averaged over 15 tubes for each sample) is then compared calculated radii using Ge concentration, strain and layer thicknesses from ULE-SIMS, XRD, and XRR. Since ULE-SIMS and XRD are able to directly identify Si layer thickness we have used their values to calculate tube radii shown in Figs. 5.9(c) and 5.9(d), respectively.

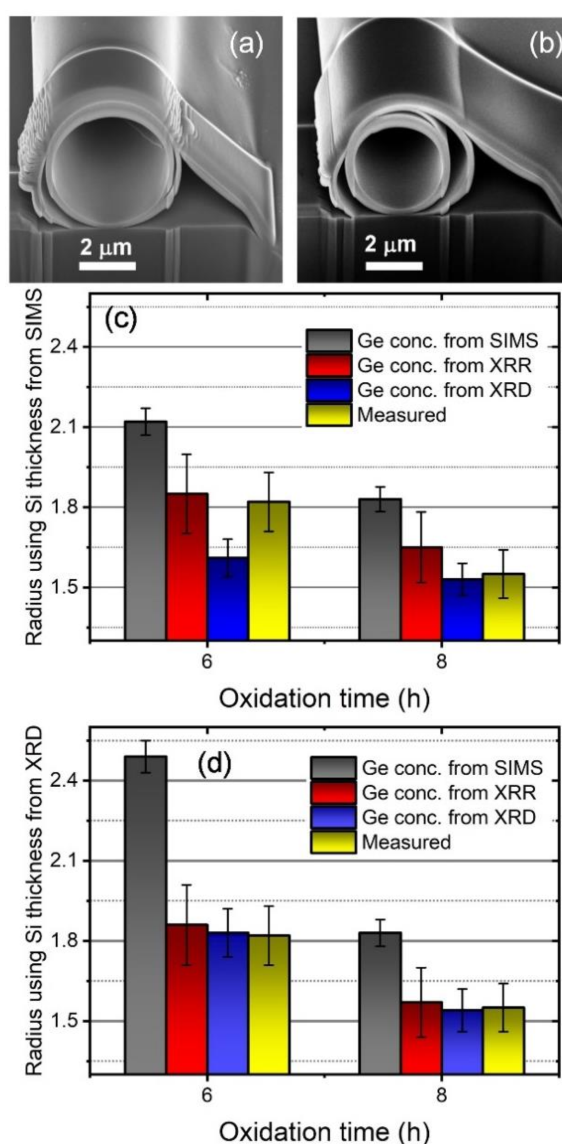

Figure 5.9: (a) SEM image of a SiGe tube obtained from the 6h oxidized layers. The tube was cut by focused ion beam. (b) Similar SEM image from a tube rolled up using 8 h oxidized layer. (c) Measured and simulated tube radii using the Si layer thickness obtained by ULE-SIMS and Ge concentration from the methods depicted in the color legend. (d) Measured and simulated tube radii using the Si layer thickness retrieved from XRD and Ge concentration from the techniques listed in the color legend.

In Fig. 5.9(c) the Si thickness from ULE-SIMS analysis was used, leading to values of radii that differ significantly from the measured SEM results independently from the Ge concentration used. If the Si thickness from XRD is used to simulate the tube radii the retrieved simulated values exhibit a fine agreement with the measured tube radius with the exception of ULE-SIMS Ge concentration data (see Figure 5.9(d)). Hence, XRD Ge-concentration and thickness are the most suitable results for a strain-dependent process such as rolling, that strongly lies on the precise determination of parameters for the crystalline thin film volume. This is expected if the system is compared to InGaAs/GaAs rolled-up bilayer tubes grown by MBE [130, 133, 134], where strain is deterministically defined by Indium (In) concentration in one of the layers (both fully crystalline).

It is worth mentioning here that tubes cannot be obtained from the sample with 10 h annealing time. In this sample, the Si rich layer becomes too thin to induce rolling, while a more uniform Ge-concentration is retrieved.

5.5. Conclusions

We have shown here a complete analysis of strain and Ge-concentration on a SiGe sample series annealed to induce controlled Ge-condensation. By comparing the Si and $Si_{(1-x)}$ $Ge_{(x)}$ layer thickness and concentration retrieved by XRD, XRR and ULE-SIMS we were able to determine the conditions that lead to the appearance of in-plane and out-of-plane strain as well as the existence of a thin SiGe amorphous oxide interface between the SiO_2 layer and the crystalline volume. The strain analysis was corroborated by rolling-up tubes and predicting their radii from selected parameters. In particular, the XRD thickness and concentration were crucial to figure out the conditions of the crystalline SiGe layer. Our results are a relevant step on the understanding of phenomena that takes place after long oxidation times (e. g. appearance of a SiGe oxide and possible amorphization of the interface) or in very thin films that may be of choice in semiconductor processes that are needed for device design.

6. Structural and electronic properties of Bi_2Te_3 grown on HOPG graphite

6.1. Introduction

Topological insulators are an emerging class of materials that has been on the focus of basic and applied research interests in the past decade [135-139]. In particular, binary bismuth chalcogenides have become reference materials, where a Dirac cone-like band structure for surface states is observed at the Γ point of the Brillouin zone [19, 140, 141], with robustness with respect to composition changes (ternary and quaternary alloys can be grown) [17,142], as well as to point defects [143, 144]. Chalcogenides of this material class (Bi_2Se_3, Bi_2Te_3, Sb_2Te_3) are usually composed of stacked two-dimensional foils, each foil possessing a single atomic specimen. They are also known to exfoliate in quintuple layers (QLs), which cleave at the van der Waals gaps between Te:Te (or Se:Se) bondings [145-147]. Although many studies have used exfoliated materials obtained from Bridgmann growth [148- 153], the growth of some binary compounds such as Bi_2Te_3 by chemical vapor deposition (CVD) [153-155] and molecular beam epitaxy (MBE) [156, 157] has been successfully achieved on top of distinct substrates [158- 162]. These techniques allow for the nucleation of limited amounts of material, ranging from the sub-quintuple layer regime (MBE) up to few microns in the CVD case [163]. Efforts have been made in the direction of keeping the desirable atomic composition or addressing a composition of interest (e.g. Bi_4Te_5, Bi_3Se_4), as well as verifying the possibility of coherent (fully epitaxial) growth on a plethora of substrate systems.

In this chapter we carried out MBE growth of Bi_2Te_3 on highly oriented pyrolitic graphite (HOPG). X-ray diffraction (XRD) results show that the grown layers, which form flat islands up to a limit of coalescence, are subjected to an in-plane strain of the order of 1% at the Bi_2Te_3/HOPG interface, with a consequent pseudomorphic strain in the out-of-plane direction. This effect is more pronounced for few-layer deposits, as probed by Bragg and

Laue-type synchrotron XRD measurements and corroborated with Raman scattering. The observed pseudomorphic strain relaxation allowed us to establish a scenario for the expected relaxation between Bi_2 bilayers and Bi_2Te_3 quintuple-layers which coexist in the Bi_xTe_y topological insulator series. From such approach the elastic constants of Bi_2 bilayers were calculated, allowing a better understanding of the strain interplay in the bulk Bi_xTe_y series. We also show here that the band structure of strained Bi_2Te_3 remains unchanged at the center of the Brillouin zone, but is affected at the M and K zone edges. The observed strain affects the underlying graphite layers, which exhibit corresponding Raman shifts. A coexistence of Bi_2Te_3 with other related phases is observed after the coalescence of flat islands, as a result of modified surface diffusion of adatoms. Our results may impact on the use of heteroepitaxial two-dimensional systems on devices and sensors, where the overall electronic band structure may be concerned.

6.2. Methods

6.2.1. Sample growth

Our samples were grown on a RIBER 32P MBE chamber located at the National Institute for Space Research (INPE) with the collaboration of researchers Dr. Eduardo Abramof and Paulo Rappl. HOPG substrates were fixed on a molyblock with a liquid Ga: In alloy. Prior to growth, the HOPG surface was degassed to remove adsorbed molecules at 300 °C for 10 min. The growth temperature was optimized at 170 °C after growth trials that ranged from 240 °C to 140 °C. The sample surface was monitored by reflection high-energy electron diffraction (RHEED). One effusion cell was filled with nominal Bi_2Te_3, while two other cells charged with pure tellurium were used to keep the desired Te_2/Bi_2Te_3 beam equivalent pressure (BEP) ratio of 2. For this purpose, Bi_2Te_3 effusion cell temperature was maintained at 497 °C, while the two Te cells were kept at 304 °C and 315 °C, corresponding to BEP values of $2x10^{-7}$ Torr for Bi_2Te_3 and $1x10^{-7}$ Torr for each Te cell. These parameters led to the deposition of Bi_2Te_3 with a rate of 0.14 QLs/min. After growth the cells shutters were closed and the substrate temperature quenched to room temperature. After removing the

samples from the MBE chamber, they were immediately characterized by atomic force microscopy. The X-ray diffraction and Raman spectroscopy measurements were performed one week and one month after growth, respectively. The set of samples used here had deposition times of 10, 20, 40, 60, 100 and 180 min that led to nominal coverages of 1.4, 2.8, 5.6, 8.4, 14 and 25.2 QLs, respectively. The nominal coverages were determined using 20 Atomic Force Microscopy images of 10 x 10 μm^2 range, in which the volume of Bi_2Te_3 deposits was evaluated for each deposition time. Measured volumes were then scaled with respect to the volume of a single, complete QL coverage (1 nm height).

6.2.2. Structural characterization

XRD measurements were carried out at the XRD2 beamline of the Brazilian Synchrotron Light Laboratory (LNLS). This experimental station has a 6+2 circle Huber X-ray diffractometer and uses the beam provided by a bending magnet source, yielding a flux of approximately 10^{11} photons/s at the sample position. A fixed energy of 10 keV was used with a X-ray spot size of 3 mm x 1 mm (Horizontal x Vertical). The used energy allowed for excellent transmission through the 300 µm thick HOPG substrate, which was firstly aligned in a Laue-type geometry used to measure the in-plane lattice parameter. Coplanar Bragg XRD was also measured using the same setup and energy. In this case measurements were performed along the (00L) direction, providing a direct measurement of the out-of-plane lattice. For each case a momentum transfer vector was defined, with $Q_\perp$ standing for the Bragg/out-of-plane measurement condition and $Q_{||}$ standing for the Laue/in-plane measurements. Their values were calculated for each geometry as $Q = (4\pi/\lambda)\sin(2\theta/2)$, where 2θ is the scattering angle and $\lambda = 1.2399$ Å.

AFM measurements were carried out in a Naio Nanosurf AFM microscope, operating in tapping (semi-contact) mode. The surface topography revealed flat deposits of Bi_2Te_3 with steps of 1 QL height (1 nm) for the initial Bi_2Te_3 growth stages, discussed in detail along the following sections.

Finally, Raman measurements were performed at room temperature using a ReniShaw InVia confocal micro-Raman spectrometer operating in backscattering geometry.

As excitation source, 632.8 nm HeNe laser line was used, yielding 4.5 mW power at the sample position. Focusing was provided by an optical microscope equipped with a 50x and 0.75 N. A. objective lens, generating laser spot size around 1 µm at the sample.

6.2.3. Band structure simulation

In order to investigate the effects of the strain induced by the graphite substrate in the band structure of few layers Bi_2Te_3, we carried out DFT calculations for different numbers of QLs, as implemented in the OpenMX package [164] by Dr. Guilherme Almeida Silva Ribeiro. A linear combination of localized pseudoatomic orbitals [165, 166] and the generalized gradient approximation [167] were used. The basis for Bi and Te atoms were Bi8.0-s2p2d2f1 and Te7.0-s2p2d3, respectively. Full-relativistic pseudopotentials [168] were used to treat relativistic effects. An energy cutoff of 160 Ry was employed for calculating the energy and wave functions and an 8x8x1 Monkhorst-Pack K-point mesh was used to sample the Brillouin Zone.

For each calculation, the lattice parameters were set to the extrapolated values obtained by our XRD analysis. Then, the interlayer distances were optimized with the constraint that the lattice parameters *a* and c (measured) remain unchanged. We employed the slab method to construct our surfaces considering at least a 10 Å vacuum between periodic images to ensure that they are not interacting.

6.3. Results

Figure 6.1 shows an overview of AFM images for samples grown with nominal coverages of 1.4, 2.8 and 5.6 QLs. At panels (a), (b) and (c) of Fig. 6.1 one observes flat Bi_2Te_3 islands with hexagonal/circular shape, grown on top of the flat HOPG substrate. Graphite steps are observed in these panels as elongated lines. For low coverages such as 1.4 and 2.8 QLs, the islands are well separated and formed by spiral domains with steps of 1 nm height, which correspond to one QL of Bi_2Te_3. Pure Bi layers, not observed in our measurements, would show heights of 0.4 nm [169]. As the coverage increases to 5.6 QLs some islands are near the onset of coalescence, but remain distinguishable. The typical Bi_2Te_3 1 nm step was

the only step height retrieved inside islands along the coverage range between 1.4 and 8.4 QLs [170]. This result indicates the absence of Te deficit in these samples, which would lead to the formation of additional $Bi_2Te_{3-\delta}$ phases (δ is the Te deficit) such as Bi_4Te_5 (δ = 0.5), BiTe (δ = 1) or Bi_4Te_3 (δ = 1.5) [160, 162]. The side length and height distributions of the islands were evaluated using 20 images of 10µm x 10µm for each sample. The lateral size and height histograms, shown respectively in Fig. 6.1(d) and 6.1(e), were obtained for approximately 400 islands of each sample.

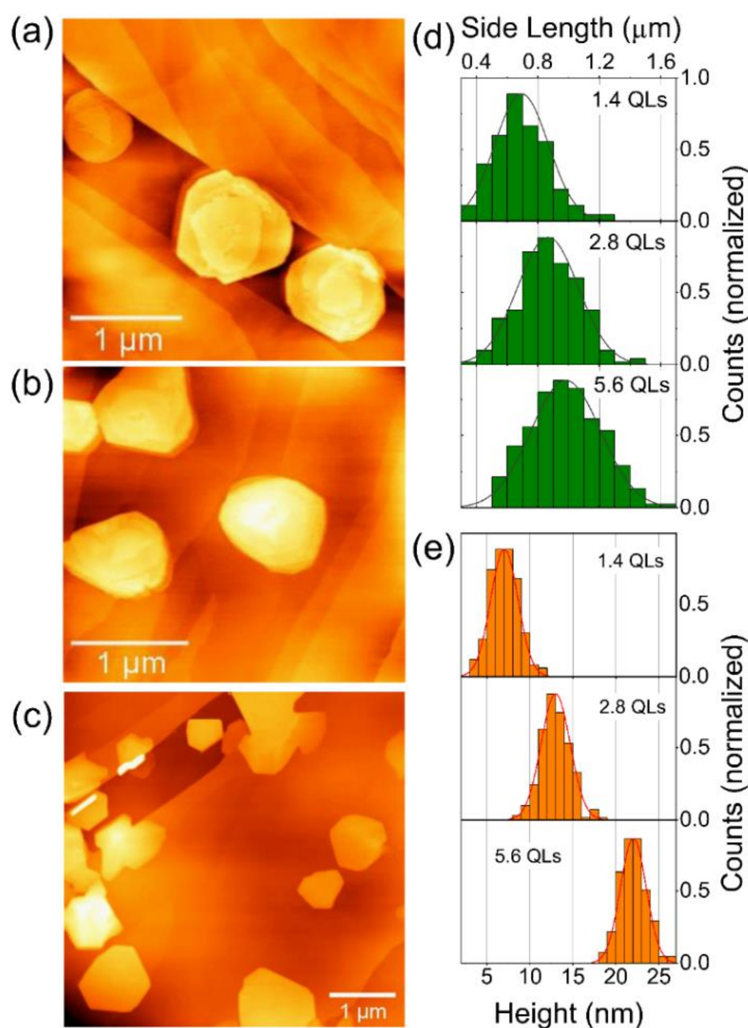

Figure 6.1: AFM topographic images of the HOPG surface after deposition of Bi_2Te_3 with nominal coverages of (a) 1.4 QLs, (b) 2.8 QLs and (c) 5.6 QLs. For these panels (a-c) the maximum height in color scale was set to 20 nm. (d) Histogram of lateral size distribution for Bi_2Te_3 islands in the three samples depicted in panels (a-c). (e) Height distribution histogram of Bi_2Te_3 islands for the three samples of panels (a-c). Approximately 400 islands of each sample were evaluated for the histogram composition.

One observes that while the lateral size remains near the 1 µm range, probably due to the graphite step distance, average island height increases linearly from 7 nm at 1.4 QLs to 22 nm at 5.6 QLs. This behavior suggests a large diffusion length of Bi and Te adatoms at the HOPG surface, with a step-flow nucleation at the islands top and side.

As the coverage is increased above the threshold of approximately 8 QLs, flat Bi_2Te_3 islands begin to coalesce. The result is noticed in AFM images by the appearance of higher regions, which are brighter in Fig. 6.2(a) and indicate the onset of coalescence. This image carried out on the 8.4 QLs sample shows that, although most of the deposited material remains in the Bi_2Te_3 flat deposits, a small volume of Bi/Te atoms starts to nucleate in another type of cluster configuration. Changes in surface morphology become more pronounced in the sample with 14 QLs of coverage, where the three-dimensional deposits are dominant for the resulting surface condition. The average lateral size and height of flat islands (up to 8.4 QLs) and coalesced islands (coverage larger than 8 QLs) is depicted in panels (c) and (d) of Fig. 6.2, respectively. In Fig. 6.2(c) we compare AFM results and X-ray measurements (discussed in the following paragraphs), evidencing that before coalescence the coherent crystalline domain size measured by XRD matches the average island height observed by AFM. This indicates that the piling up of successive QLs keeps the full crystallographic registry initiated at the HOPG / island interface. Such linear growth in the out-of-plane direction is interrupted by the coalescence of islands, which leads to a faster growth at the contact points between islands [brighter/higher regions in Fig. 6.2(a)]. After this point (coverage larger than ~ 8 QLs) one can only follow the average height using AFM, comparing local height with regions where HOPG is still observed. The three-dimensional deposits that take place on top of the original epitaxial flat objects are incoherent at such coverages. As a consequence, the evaluation of crystalline domain from XRD [right side of panel (c)] shows a reduction of the out-of-plane crystalline size, which is related to the appearance of other Bi_xTe_y phases that destroy the registry of Bi_2Te_3 crystals (see following paragraphs).

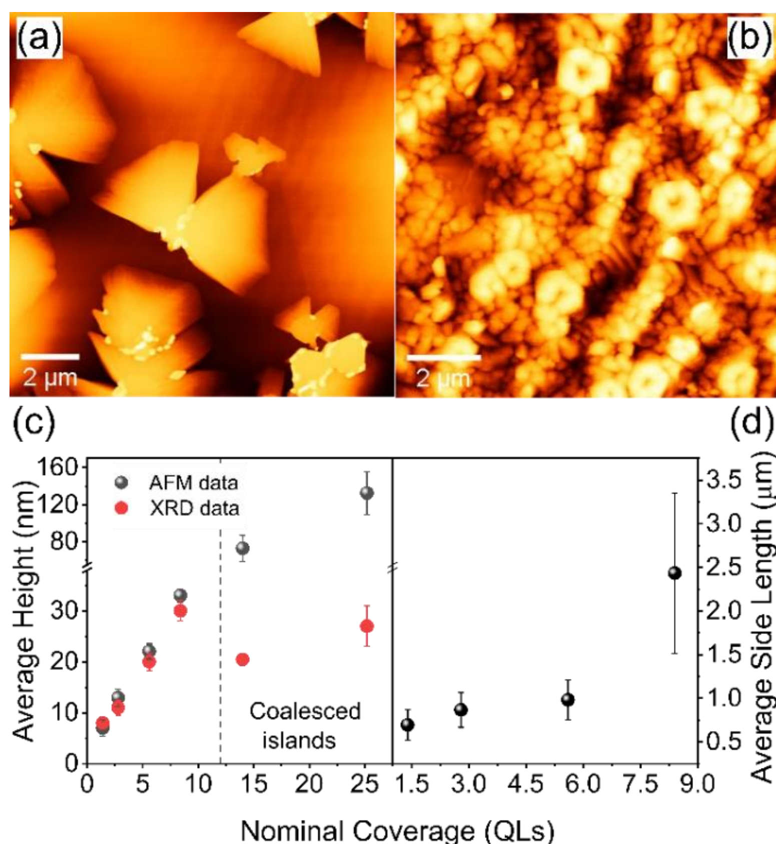

Figure 6.2: (a) AFM topographic image carried out at the sample with 8.4 QLs of Bi_2Te_3 coverage on graphite HOPG. One observes the onset of coalescence, denoted by the higher regions (brighter spots). Maximum height value for the used color scale is 70 nm. (b) Similar image measured at the sample with 14 QLs of coverage. Maximum height value for the used color scale is 120 nm. (c) Average Bi_2Te_3 island height, measured by AFM and extracted from the XRD measurements of Fig. 6.3. The threshold for coalescence is sketched by the vertical dashed line. (d) Average side length obtained by AFM for Bi_2Te_3 islands within the coverage range below the coalescence threshold.

Concerning the average side length of flat islands, one observes that lateral growth rate is reduced if compared to the out-of-plane growth rate. While an increase of a factor 3 is observed at the island height from 1.4 QLs up to 5.6 QLs, their side length only increases 50% along this interval. This is an indication that adatoms have high in-plane mobility at the HOPG substrate and can diffuse in the out-of-plane direction at a Bi_2Te_3 platelet border, causing the step-flow growth, which is responsible to complete layers leaving few incomplete steps at the island top. Once the coalescence begins, out-of-plane and in-plane growth rates are modified and the island side length starts to increase rapidly, as indicated by the higher coverage point (8.4 QLs) of Fig. 6.2 (d). After this coverage the

coalescence renders the AFM measurement of island side length [Fig. 6.2(d)] unfeasible (one cannot tell where one island ends and its adjacent island begins).

Synchrotron XRD measurements allow to follow up the evolution of crystalline domain size, strain/epitaxial relation and crystallographic phases of our MBE-grown films. We begin our discussion with the Bragg XRD data retrieved along the (00L) HOPG crystal truncation, obtained using a coplanar geometry, as depicted in Fig. 6.3(a). It is useful here to start with the 14 QLs sample, where a complete set of features is observed. Besides the very intense graphite peaks labelled in the graph of Fig. 6.3(b), one observes diffraction intensity from distinct phases of Bi_xTe_y alloys. The XRD peaks of the Bi_2Te_3, BiTe and Bi_4Te_3 phases are indicated in this panel according to reference crystallographic data [146, 171]. One observes that for this coverage Bi_2Te_3 is still the dominant phase, however the contributions of other phases cannot be neglected. In fact, these other phases are responsible for the formation of three-dimensional islands observed in Fig. 6.2(b). Measurements for this sample also exhibit peaks with non-zero reciprocal space indexes H and K, indicating that the (00L) registry with the substrate is lost for part of the deposited material volume.

On the other hand, lower coverages in our sample set exhibit only Bi_2Te_3 diffraction peaks along the (00L) direction. The absence of peaks with non-zero (H, K) reciprocal space indexes is an indicator of epitaxial relation with respect to the HOPG registry. For this coverage range (1.4 QLs up to 8.4 QLs) the full out-of-plane XRD scans are shown in Fig. 6.3(c). One observes that the Bi_2Te_3 peak widths decrease as the nominal coverage increases. Such effect is ascribed to the raise of the coherent epitaxial domain size along the out-of-plane direction, already depicted in the graph of Fig. 6.2(c). For the data shown in this graph, the XRD height is extracted from the relation $H = (2\pi/\Delta Q_\perp)$, where $\Delta Q_\perp$ is considered to be the (006) peak width. The intensity of the Bi_2Te_3 peaks at the sample with 8.4 QLs is reduced with respect to its 5.6 QLs counterpart, probably due to the introduction of defects and mosaic spread in the borders of coalesced domains. A careful look to these peaks also reveals a shift towards larger values of $Q_\perp$, indicating an increase of out-of-plane lattice parameter for lower coverages (see discussion section).

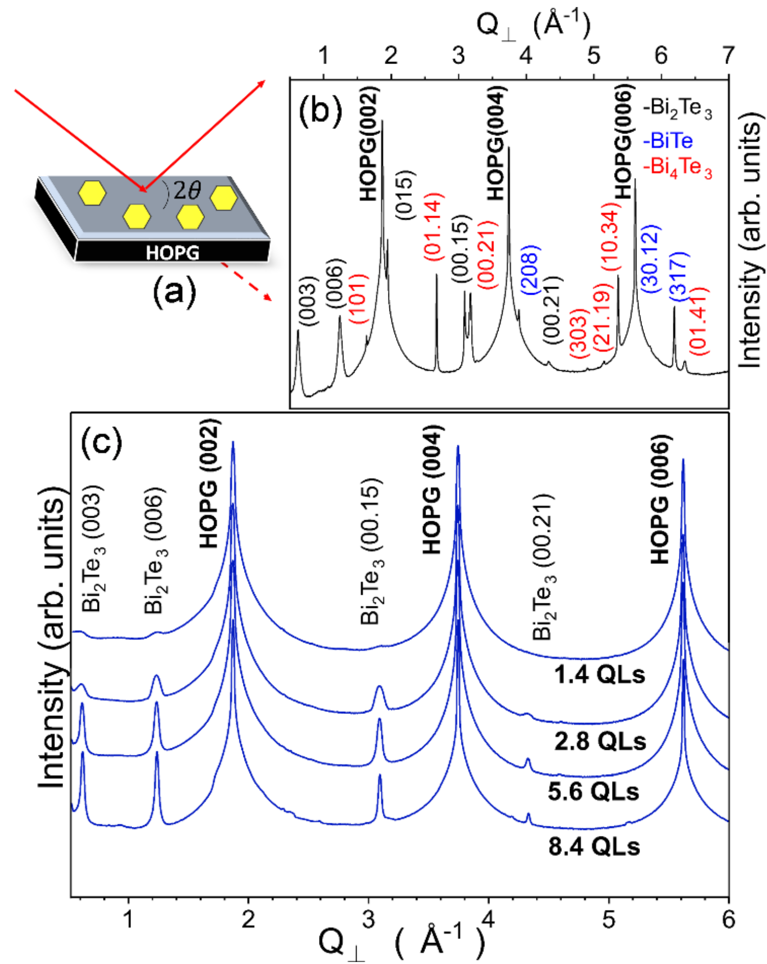

Figure 6.3: (a) Geometry used for synchrotron coplanar Bragg XRD. (b) Longitudinal scan along the (00L) direction for the 14 QLs sample, showing strong HOPG graphite peaks and the coexistence of epitaxial Bi_2Te_3 and other Bi_xTe_y phases (labelled in the figure) that appear after island coalescence. (c) Longitudinal scans along the (00L) direction for samples with only Bi_2Te_3 epitaxial growth, corresponding to the coverage interval between 1.4 and 8.4 QLs.

The expected in-plane registry between Bi_2Te_3 and graphite is sketched in Fig. 6.4 (a) [172, 173]. If the registry observed along the out-of-plane direction for samples between 1.4 and 8.4 QLs is fully epitaxial, one expects to observe coherent in-plane lattice matching. Since the HOPG substrates (300 µm thick) are relatively transparent to 10 keV photons (a transmission of 22.5% is expected), we were able to perform Laue-type diffraction measurements. The sample was then positioned at the diffractometer in the Laue geometry shown in Fig. 6.4(b) and the HOPG graphite (100) peak was aligned. A longitudinal scan spanning from few degrees below the HOPG (100) peak up to the (110) peak is shown in Fig. 6.4(c). We observe here that Bi_2Te_3 peaks with non-zero (H, K) reciprocal space indexes and L

= 0 are retrieved besides the HOPG peaks. Such finding corroborates the epitaxial relation between substrate and MBE deposited layers. A shift of the Bi_2Te_3 (110) peak towards larger values of $Q_{||}$ is observed for the smaller coverages, as shown in the inset of Fig. 6.4(c).

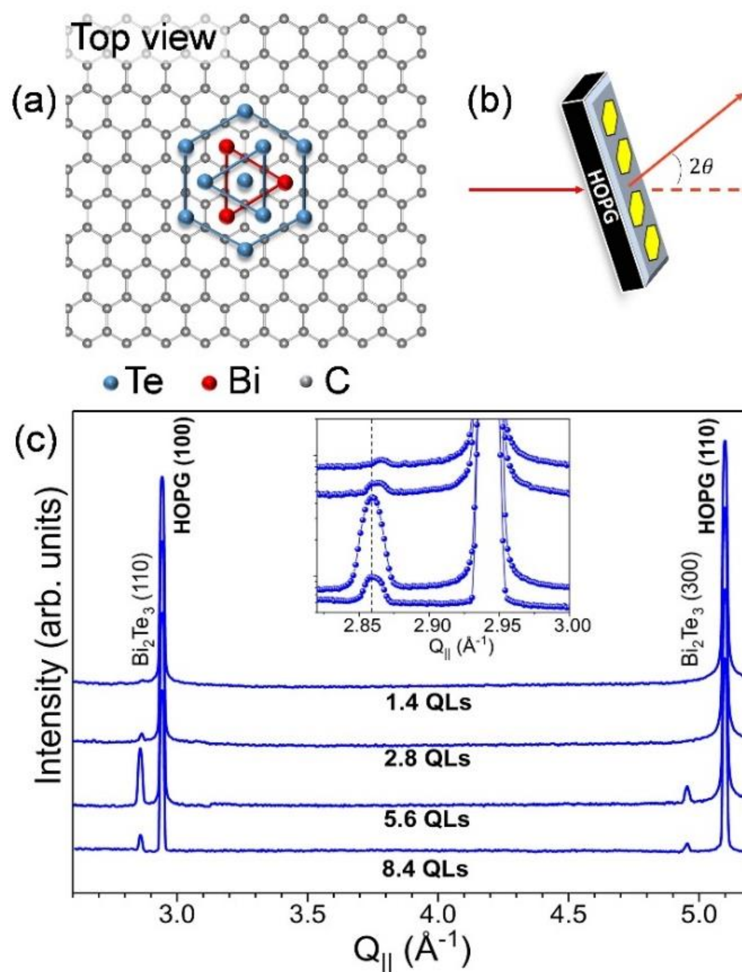

Figure 6.4: (a) Expected epitaxial relation between HOPG graphite and Bi_2Te_3, according to refs. [172, 173]. (b) Scattering geometry for Laue XRD measurements. (c) Longitudinal scans along the in-plane direction, showing HOPG and Bi_2Te_3 peaks. The inset shows in detail the evolution of the Bi_2Te_3 (110) peak, with a shift towards larger $Q_{||}$ values (smaller lattice parameter) for the lower coverage samples.

Such in-plane lattice contraction observed at the 1.4 and 2.8 QLs samples is compatible with a pseudomorphically strained layer (with out-of-plane expansion), as observed in the results of Fig. 6.3(c). The origins and consequence of such pseudomorphic strain in a system with van der Waals interactions are discussed in Section 6.4. Finally, one observes again that the peak intensities reduce for the 8.4 QLs sample with respect to the

5.6 QLs sample, as an indication of the onset of nucleation of non-epitaxial phases after island coalescence.

The retrieved strain at the Bi_2Te_3/HOPG interface must be corroborated with an independent technique. We then carried out Raman spectroscopy measurements for the whole set of samples. The main lattice coupling modes that are active in Raman effect are depicted in Fig. 6.5(a) with the corresponding spectra for the region where Bi_2Te_3 peaks are found.

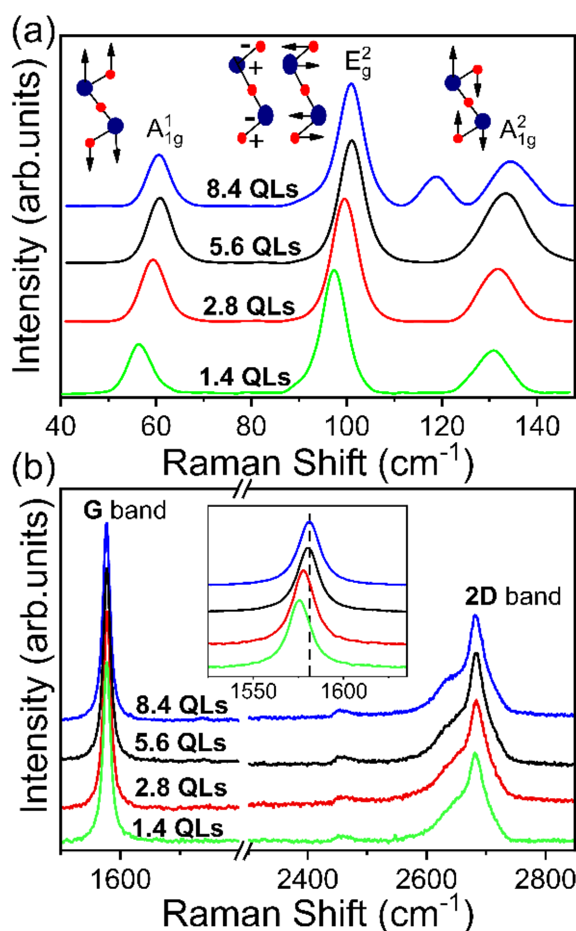

Figure 6.5: Raman spectra measured for the Bi_2Te_3 / HOPG samples set with coverage ranging from 1.4 to 8.4 QLs: (a) in the energy interval of Bi_2Te_3 A^1_{1g}, E^2_g and A^2_{1g} peaks showing a shift of the Raman modes for the 1.4 QLs and 2.8 QLs samples with respect to other coverages; (b) in the energy interval of graphite G and 2D bands, exhibiting a gradual shift of the G band position to lower energies as the coverage reduces. The inset presents a zoom in the G band, where a maximum shift of 6 cm^{-1} can be observed for our sample with lowest coverage.

One observes again a shift of the Raman modes for the 1.4 QLs and 2.8 QLs samples with respect to other coverages. This gradual shift of the characteristic vibration

modes can provide an evidence of interlayer interaction between Bi_2Te_3 and HOPG. The additional peak at ~117 cm^{-1} measured for the 8.4 QLs sample also corroborates the presence of structural defects in our system for such coverage. Since 632.8 nm wavelength photons have a limited penetration on the HOPG when compared with hard X-rays, we could verify whether the substrate lattice is strained by the presence of a Bi_2Te_3 island. The G and 2D bands of graphite are well separated from the Bi_2Te_3 Raman peaks, and we were able to observe a systematic shift of the graphite G band, shown in Fig. 6.5(b) and detailed on its inset. The corresponding graphite in-plane strain estimated for a shift of ~ 6 cm^{-1} of this band is equivalent to ~ 0.3 % compressive strain.

6.4. Discussion

We start our discussion with the evaluation of the observed Raman shifts for the non-coalesced island samples. Fig. 6.6 shows the behavior of the Bi_2Te_3 peaks, as well as the HOPG G band. The redshift in the out-of-plane A^1_{1g} mode has already been observed in few quintuple layer topological insulator (TI) samples [174, 175], which is a result of phonon softening effect due to the reduction of interlayer interactions when the island thickness decreases. It is interesting to note that the second out-of-plane vibration mode A^2_{1g} also exhibits a slightly redshift for low coverage samples; this fact differs from that obtained from other TI samples, which show an upward shift for the frequency of A^2_{1g} mode for thinner samples [176, 177]. These results demonstrate that a tensile strain in out-of-plane direction does exist and corroborates with our XRD analysis. The observed shift at the E^2_g peak, which usually remains at a fixed position and is roughly non-sensitive to strain [173], may be due to the small lateral size of our islands at the lowest coverage sample (1.4 QLs). At this condition domains with average lateral dimensions of 650 nm are retrieved by AFM, while previous works report analysis on islands with 1.5 µm ~2.0 µm lateral size. We speculate that the larger surface/volume ratio at our samples is responsible for this result.

The compressive in-plane strain of Bi_2Te_3 island observed in XRD measurements might give rise to a tensile strain in topmost HOPG layers. Indeed, it is possible to observe in Fig. 6.6 a clear redshift of HOPG G band for lower coverage. The redshift of G band indicates

a (locally) tensile strain in the HOPG substrate and, although no specific model was retrieved at the literature to direct analyze the shifts of Bi_2Te_3 and ascribe an estimated strain, the HOPG strain could be evaluated. The estimated strain according to Ferralis [177] is 0.3 %. In our case, since the red laser screens through approximately 100 nm substrate depth, this value represents an average for the graphite layers below our Bi_2Te_3 deposits. Such observed Raman shift of the graphite G band is not followed by any change on the peak width, which points out to a strain origin, instead of a charge transfer phenomenon [178].

It is worth to note that a new vibration mode is observed for the 8.4 QLs sample around 117 cm^{-1}. According to group theory, this peak represents the phonon mode A^2_{1u}, which is not Raman active, but infrared-active (IR-active) [174]. The appearance of this additional IR-active mode, which has already been observed in other TI nanostructured samples [153, 179, 180], is a consequence of the breakdown of inversion symmetry in the layered structure of Bi_2Te_3 that relax the selection rule of Raman tensors. Here, we infer that the presence of such IR-active mode is a result of stacking defects introduced on Bi_2Te_3 island during the coalescence process, which agrees with the reduced peak intensity in Laue-type XRD results and the observed change in the resulting AFM surface morphology.

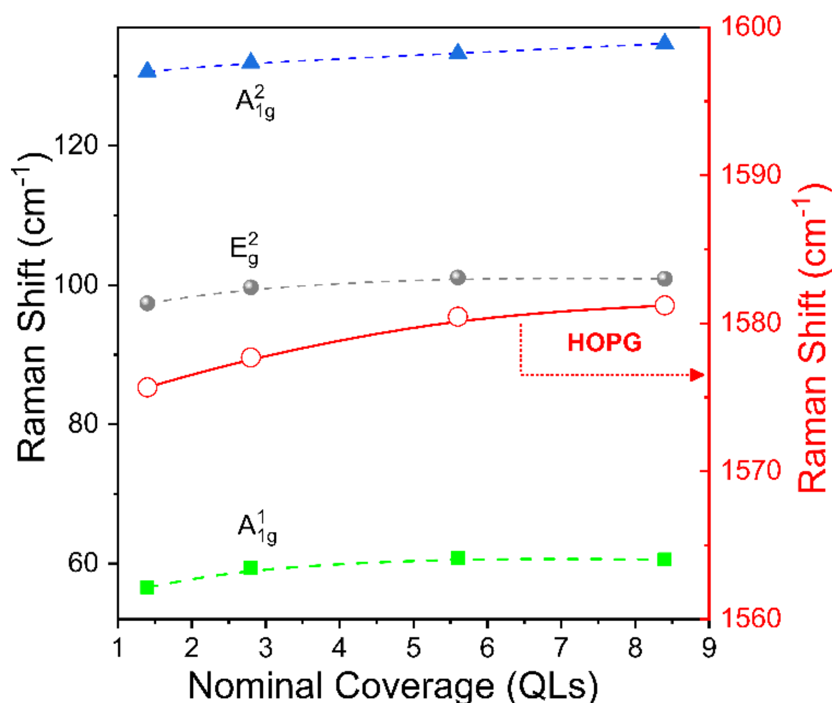

Figure 6.6: Energy shifts of the Raman peak positions as a function of nominal coverage for the Bi_2Te_3 / HOPG samples, extracted from the Raman spectra displayed in figs. 6.5(a) and 6.5(b).

In order to proceed with the discussion on the measured X-ray datasets previously described we must change of sample coverage labeling, providing a reliable indication of island height. Hereafter we refer to the samples as a function of their average island thickness determined by AFM measurements. This choice was made due to the existence of large areas uncovered by Bi_2Te_3, as well as the concentration of material in vertical stacks on top of each island (nominal coverages can be misleading with respect to actual island height). Therefore, the sample labels, initially set to their nominal coverage, are replaced by the AFM data of Fig. 6.2(c). In this sense, the samples with coverage of 1.4, 2.8, 5.6, 8.4, 14 and 25.2 QLs are now referred as 7.0, 12.9, 22.0, 33.0, 72.0 and 133 nm of height, respectively. With the empirical relations extracted from Fig. 6.7 (see next paragraphs) we are able to extrapolate the lattice parameter behavior for the range of island height between 1 nm and 6 nm Bi_2Te_3 thickness.

The relation between the out-of-plane lattice parameter as well as the in-plane lattice parameter as a function of the Bi_2Te_3 island height is shown in figures 6.7(a) and 6.7(b), respectively. In these graphs actual sample data was represented by solid blue dots. A fit with an exponential function is obtained and then used to extrapolate the observed behavior to the first or few-QLs that are closer to the HOPG surface. The additional points generated for 1 nm to 6 nm Bi_2Te_3 thickness (meaning the first QLs of the system) are shown by black dots for each panel. In this sense, although our sample with lowest coverage exhibits an out-of-plane tensile strain of 0.7% and an in-plane bi-axial compressive strain of 0.3 %, these values correspond to an average over 7 nm thickness. The maximum estimated strain value for out-of-plane and in-plane lattices would then take place at 1 nm thickness, which corresponds to the first QL in contact with HOPG. Extrapolated values point out to 1.3 % tensile strain in the out-of-plane direction and 1.2% biaxial compressive along the in-plane direction.

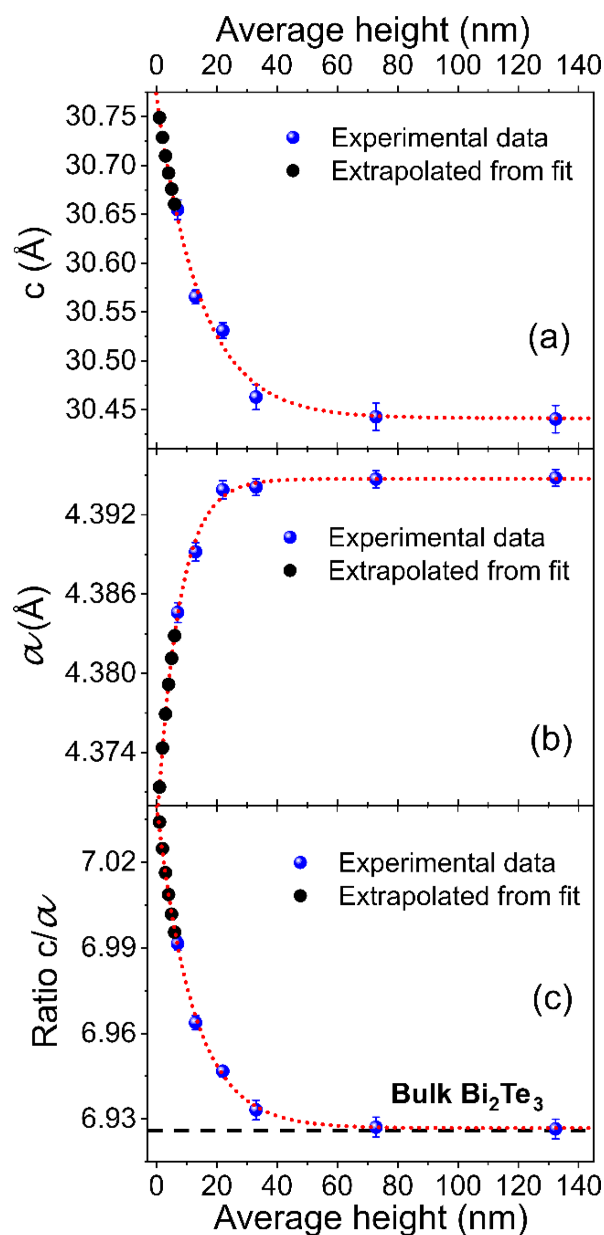

Figure 6.7: Measured (blue dots) and extrapolated (black dots) lattice parameters from our XRD results. (a) Out-of-plane and (b) In-plane lattice parameter as a function of island average height. (c) The behavior of the c/a ratio showing the complete relaxation to the bulk Bi_2Te_3 lattice parameters for high coverage samples. In all panels, the red short dotted lines represent the exponential fit. The bottom dashed line shows the bulk c/a ratio.

Such extrapolated values are considerably large for a van der Waals system, but are still within the range of expected fully epitaxial conditions. The succession of piled QLs leads to a strain relaxation along the first 15 ~ 18 QLs, in a monotonic way. The ratio *c/a* clearly changes along the distinct coverages, as shown in Fig. 6.7(c), indicating that the strain

accommodation along the QL steps results from small changes inside each QL, followed by larger changes along the van der Waals gaps, where the increase of electronic density due to the compressive strain may cause an electrostatic repulsion between adjacent QLs, producing a larger relative shift in the *c* lattice parameter if compared to a.

The strain relaxation gradient obtained here from the epitaxial relation of few-layers of Bi_2Te_3 on graphite can be used as a starting point for a deeper analysis on the conformation of Bi_2Te_3 and Bi_2 layers that are intercalated in the Bi_xTe_y series of compounds. As noted in Refs. [181, 182] Bi_2Te_3 is a compound formed of stacked QLs, while other compounds such as Bi_4Te_5, Bi_6Te_7, Bi_8Te_9, BiTe, Bi_4Te_3, Bi_2Te and Bi_7Te_3 are formed of intercalated Bi_2Te_3 and Bi_2 layers (also referred as Bi-bilayers or BLs). As shown in Fig. 6.8(a) these compounds are formed by a respective QL/BL ratio of 5:1, 7:2, 2:1, 3:3, 1:2 and 6:15, respectively, yielding total Bi fractions of 0.44, 0.46, 0.47, 0.50, 0.57, 0.67, 0.70, respectively [181, 182]. In this series of compounds, the in-plane lattice parameter varies in between 4.395 Å, for Bi_2Te_3 and 4.545 Å for pure Bi_2, which represents a lattice parameter difference of 3.3% considering the extreme compositions.

It is remarkable that for the series of compounds some elastic properties such as Poisson's ratio and Young modulus can be retrieved in the literature, while for Bi_2 layers (commonly referred as Bi-bilayers or BLs) no elastic information is provided besides the bulk values. From our experiment we found that the initial strain imposed by the graphite substrate on Bi_2Te_3 layers relaxes at a rate of 0.2 ~ 0.1% for each QL in the range of 1 to 6 QLs. Such value can be used to establish reasonable local strain relaxation between QLs and BLs in the Bi_xTe_y series and infer the elastic properties of Bi_2 BLs in these systems.

For coherent biaxially strained hexagonal films on top of hexagonal substrates, the strain energy for a film with thickness *h* can be calculated by equation 6.1 [33 ,183]:

$$U_{coh-hex} = \frac{h\varepsilon_{//}^2}{s_{11}+s_{12}} = E_{11}\frac{h\varepsilon_{//}^2}{1-\nu_{21}}. \tag{6.1}$$

Where s_{11} and s_{12} are the matrix terms of the compliance tensor, with $s_{11} = (E_{11})^{-1}$ and $s_{12} = -\nu_{21}(E_{11})^{-1}$. E_{11} and ν_{21} are the in-plane Young modulus and Poisson's ratio, respectively, for a hexagonal lattice as discussed in the section 2.1.3. $\varepsilon_{//}$ is the in-plane strain, given by equation 6.2:

$$\varepsilon_{//} = \frac{2(a_{interf,//} - a_{film,//})}{(a_{interf,//} + a_{film,//})}; \tag{6.2}$$

where $a_{interf,//}$ is the in-plane lattice parameter at the film interface and $a_{film,//}$ is the in-plane lattice parameter of Bi_2 BLs or Bi_2Te_3 QLs, depending on the configuration of the compound. We use equation 6.1 and minimize the strain energy by approaching the measured lattice parameters for the Bi_xTe_y series and minimizing both strain energy and in-plane interface lattice parameter for a stack of epitaxial BLs and QLs according to the ratios exposed above.

Figure 6.8 summarizes our results. In panel (b) we show the measured in-plane lattice parameters for the series of compounds (white dashed bars), and compare them with two distinct calculations. In both cases we assume the Bi_2Te_3 elastic constants E_{11} = 52.5 GPa and ν_{21} = 0.3, according to Ref. [184]. If one uses the bulk Bi values (E = 32 GPa and ν = 0.35) on the Bi_2 BLs and minimizes the elastic energy (eq. 6.1) for the stacking sequence of each Bi_xTe_y compound, the in-plane lattice parameters retrieved are those shown by narrow orange bars in Fig. 6.8(b). These values are considerably different from the measured ones and imply in the in-plane lattice differences depicted in orange bars in Fig. 6.8(c), extracted from the measured lattice of Bi_xTe_y compounds and the calculated values. A second calculation is then carried out, minimizing the differences of in-plane lattice parameter and in-plane strain energy for the series as a whole by varying the in-plane Young modulus and Poisson's ratio (E_{11} and ν_{21}) for Bi and equations (6.1) and (6.2). Such calculation leads to the results represented by the green bars in figs. 6.8(b) and (c). In this case the lattice difference of each layer stack to the respective Bi_xTe_y measured value is reduced, resulting in strains of the order of 0.1 ~ 0.2%. These values are within in the range of strain relaxation observed experimentally here for each van der Waals gap, keeping the epitaxial film. The retrieved values for the in-plane Young modulus of Bi_2 BLs was E_{11} = 96 $\pm$ 7 GPa with an in-plane Poisson's ratio ν_{21} = 0.25 $\pm$ 0.05. Such large E_{11} value, in comparison to the bulk Bi and Bi_2Te_3 Young modulus, explains why the addition of few Bi_2 BLs is able to increase the lattice parameter for increasing Bi_2 content in the range of total Bi content from 0.44 to 0.50 of the Bi_xTe_y series.

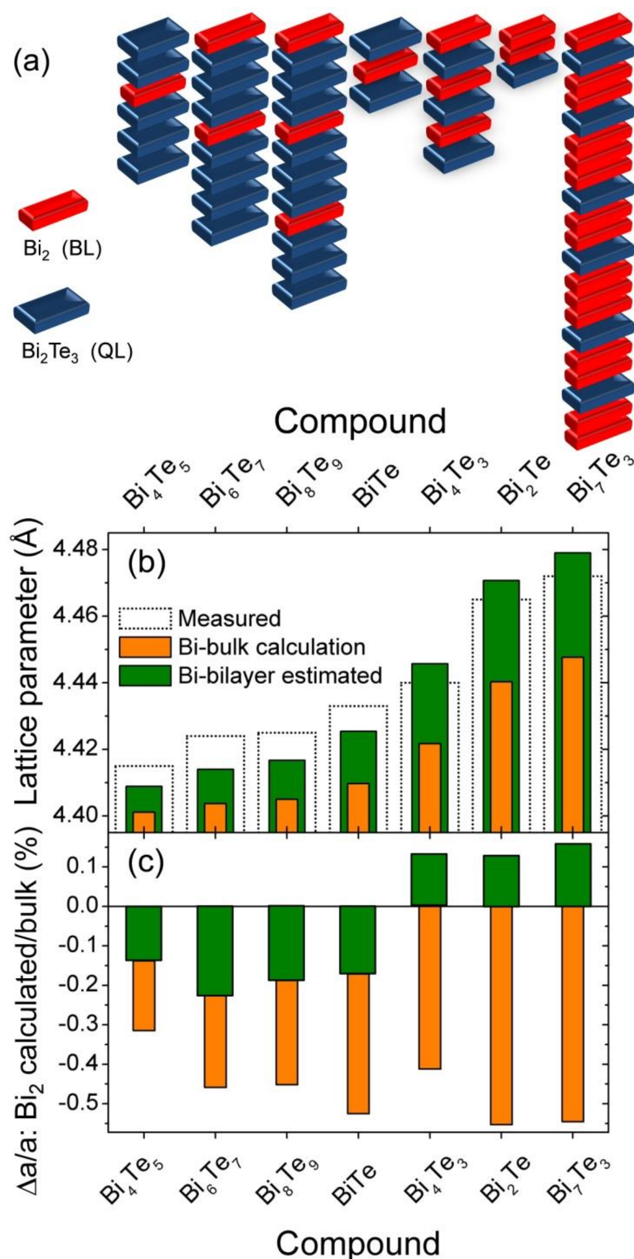

Figure 6.8: (a) Schematic representation of the stacked layers that form the crystal structures of the Bi_xTe_y series of compounds, made from Bi_2Te_3 QLs (blue) and Bi_2 BLs (red) building blocks. (b) Comparison of in-plane lattice parameter for the Bi_xTe_y series for measured values (white/dashed bars), values calculated from elastically strained Bi_2 and Bi_2Te_3 layers using the bulk Bi elastic constants (narrow orange bars) and the stack of Bi_2/Bi_2Te_3 layers with the optimized E_{11} and ν_{21} elastic constants for Bi_2 layers that minimize strain and elastic energy for the compound layer stack. (c) Lattice parameter difference of Bi_2 layers with respect to the measured values using the Bi bulk parameters (orange bars) and the retrieved Bi_2 BL elastic constants E_{11} and ν_{21} (green bars).

Finally, the impact of the experimentally retrieved strains on the electronic band structure of Bi_2Te_3 must be addressed. As known in the literature [185, 186], the energy gap

at the Γ point decreases as the number of QLs increases. The material starts as a semiconductor, becomes a metal, and then, converges to the topological insulating phase. Hence, one can observe the existence of the Dirac cone at Γ point, signature of a three-dimensional topological insulator of the Bi_2Te_3 family. The four panels of Fig. 6.9 show the evolution of the band structure by varying the number of QLs. Red lines represent the band dispersion obtained using the lattice constants found by our XRD measurements whereas black lines denote the ones obtained considering bulk values for *a* and *c*.

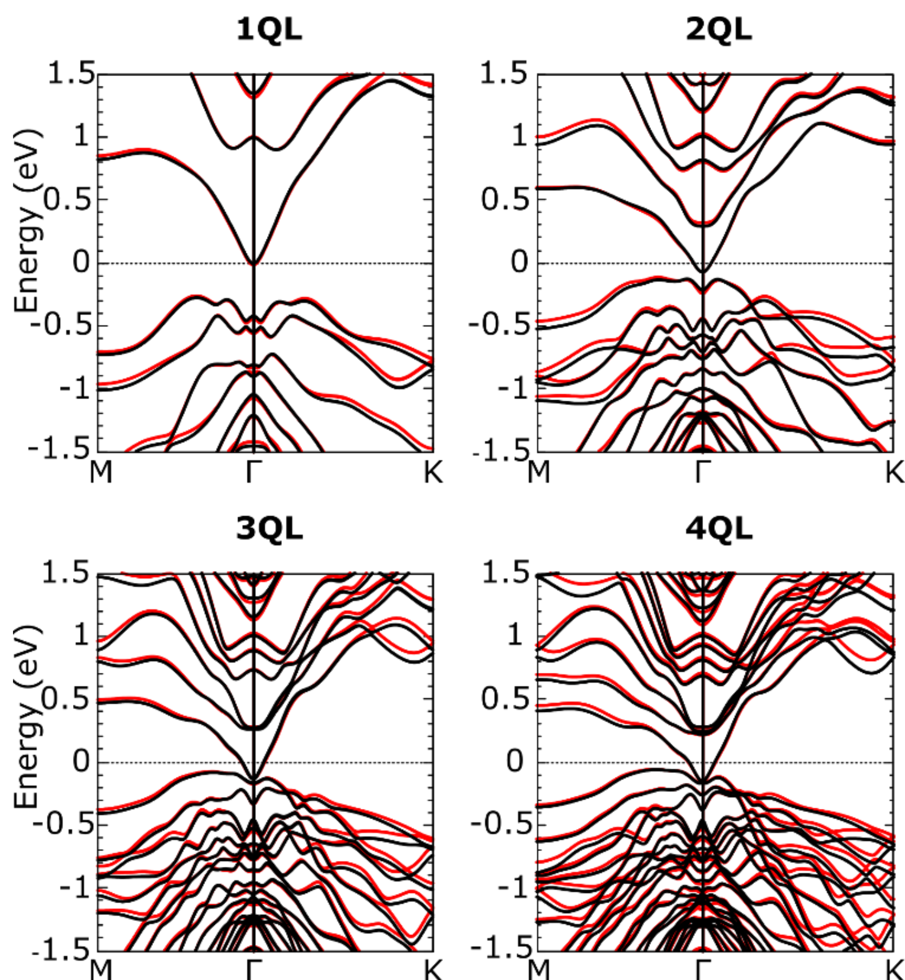

Figure 6.9: Calculated band structure of Bi_2Te_3 for different values of thickness in quintuple layers. Red lines represent the band dispersion obtained using the lattice constants found by our XRD measurements whereas black lines denote the ones obtained considering bulk values for a and c.

The effect of the strain manifests itself mostly in high symmetry points near the Brillouin Zone border, where the dispersion curves present a shift in energy. Although this

shift does not impact at the opening of a gap at the Γ point they represent an additional degree of freedom for valleytronics. The value of the gap at each high symmetry point (M and K) is found to shift by an energy difference of 100 meV for the investigated values of *a* and *c*. The shape of the bands remains mostly unchanged since the ratio between the bulk and the extrapolated lattice constants values are of the order of 1%. Larger changes would be observed by applying much larger strains [187].

The calculated energy shift due to strain at the edges of the Brillouin Zone would be hardly observed due to the energy resolution of a technique such as angle-resolved photoemission spectroscopy (ARPES). At the low coverage regime most of the surface still consists of exposed HOPG, which is polycrystalline in the in-plane direction, restricting the possibility of a well-determined orientation in reciprocal space and masking the Bi_2Te_3 signal within common energy resolution and intensity from most of the known experimental setups.

Nevertheless, our results suggest that the physical contact of Bi_2Te_3 deposits with a semimetal (HOPG) can induce new conduction channels, which may be tuned with the observed interfacial strain. We propose here that future trials modifying the chemical composition with controlled deposition procedures could be employed within the Bi: Sb: Te: Se system, keeping the topological insulator characteristics but modifying the interfacial strain. Such changes could be employed to modify band valleys along the band structure, allowing for the tuning of electronic properties.

6.5. Conclusions

We have shown here that Bi_2Te_3 flat islands grow coherently on HOPG substrates up to a nominal coverage of ~ 8 QLs, which is shown to be a limit for island coalescence at our growth conditions. The MBE samples studied here provide a suitable set for exploring interfacial strain, which is unfeasible for growth procedures based in Chemical Vapor Deposition (CVD), that usually yields thicker layers (above 10 QLs [172]).

Synchrotron X-ray diffraction analysis of our Bi_2Te_3 islands indicate that these structures exhibit a large in-plane compressive strain at the Bi_2Te_3/HOPG interface

accompanied by a consequential out-of-plane pseudomorphic expansion. The measured in-plane strain for our sample with the lowest coverage was found to be of the order of 0.7% (compressive), which is a large value for a system with van der Waals bonds. Extrapolated values for the first quintuple layers range up to 1.2%. Strain is often probed in this system by Raman measurements, repeated here for corroboration despite of lacking specificity and resolution of XRD methods. The redshift of Bi_2Te_3 Raman peaks with reducing coverage observed here demonstrate that a tensile strain in out-of-plane direction does exist, supporting the XRD analysis. Also, a locally tensile strain in the HOPG substrate close to the interface is evidenced by a redshift of the graphite Raman G band.

Our results allow us to estimate the elastic constants of Bi_2 bilayers in the Bi_xTe_y series, assuming that a strain relaxation takes place along successive van der Waals gaps of Bi_2Te_3 in our Bi_2Te_3: HOPG films. The observed lattice gradient above the Bi_2Te_3/HOPG interface was used as a suitable limit for lattice relaxation in similar layered systems.

Finally, the electronic structure of Bi_2Te_3 subjected to strain values compatible with experimental results was calculated by DFT methods. Although the in-plane strain values used in our simulations do not affect the electronic structure at the center of Brillouin zone (evidencing the robustness of the topological state), they can play a major role at the M and K edges. Such changes can potentially be used to tune valley properties (valleytronics) of topological materials that may be induced by both structural or chemical constraints).

7. Local electronic response of Bi_2Te_3 topological insulator upon magnetic doping

7.1. Introduction

The influence of magnetic dopants on materials with topological insulating (TI) properties is still an open question for the scientific community. From the theoretical point of view, a magnetic impurity distributed in the crystalline lattice of a TI material acts like a locally applied magnetic field, breaking the time reversal symmetry (TRS). Consequently, the Kramer's degeneracy at Γ point will be lift giving rise to massive fermions subject to backscattering processes.

An understanding of how magnetic impurities influence the topological surface states can provide a prototypical scenario which is useful for understanding future possibilities such as the realization of anomalous quantum hall effect [44] and development of spintronic devices with well-defined spin channels [45]. However, as discussed in section 2.2.3.1, some efforts have been made aiming to test the robustness of surface states experimentally or to investigate the manifestation of ferromagnetic properties, as observed in crystals of Bi_2Te_3 and Bi_2Se_3 doped with Cr and Fe, respectively [45, 46].

In this chapter, we studied the effect of Europium (Eu) doping on MBE-grown Bi_2Te_3 thin films. For films with different Eu concentration, morphological and electronic characterizations were carried out using AFM, STM and STS techniques. Since Europium is a rare earth metal with large magnetic moment (~ 8.8 μ_B) [47] its influence on Bi_2Te_3 topological surface states can be studied locally by the STS technique, differing from experiments that study large surface area effects such as ARPES.

7.2. Methods

In this work, all bismuth telluride (Bi_2Te_3) thin films were grown by the Molecular Beam Epitaxy on Barium fluoride (BaF_2) substrates oriented along the (111) crystallographic

direction with the collaboration of researchers Dr. Eduardo Abramof and Paulo Rappl, following the same growth parameters established in reference [47]. In summary, BaF_2 substrates were kept at a temperature of 270°C and three effusion cells were used: the first filled with nominal stoichiometric Bi_2Te_3, the second charged with Te in order to compensate the tellurium (Te) loss during deposition and a third cell charged with Europium (Eu) solid solution used for doping the Bi_2Te_3 film. A series of samples with nominal Eu concentration ranging from 0% (pure Bi_2Te_3) to 11% and 50 nm Bi_2Te_3: Eu film thickness were grown.

In order to protect the surface of these films from oxidation, an amorphous Te cap layer was deposited on Bi_2Te_3 after growth and subsequently removed in vacuum for STM/STS measurements. A complete description of the surface protection of Bi_2Te_3 films with amorphous Te layers is found in reference [188].

Scanning Tunneling microscopy (STM) and Scanning Tunneling spectroscopy (STS) measurements were performed under ultra-high vacuum conditions in an Omicron-VT STM system operating at room temperature, with a base pressure of 10^{-10} mbar. All STM images were acquired in constant current mode and for STS measurements a lock-in amplifier was used to obtain differential conductance (dI/dV) curves directly. Atomic Force Microscopy (AFM) measurements were carried out in a FlexAFM Nanosurf microscope, operating in tapping (semi-contact) mode within an environment with controlled humidity, always kept below 30%.

Finally, Raman measurements were performed at room temperature using a ReniShaw InVia confocal micro-Raman spectrometer operating in backscattering geometry. As excitation source, a 632.8 nm HeNe laser line was used, the laser power was carefully adjusted to 0.07 mW in order to avoid heating at the sample position. Focusing was provided by an optical microscope equipped with a 50x and 0.75 N. A. objective lens, generating laser spot diameter around 1 µm at the sample.

7.3. Results

7.3.1. Morphological characterization

In order to analize the Europium incorporation in Bi_2Te_3 thin films a series of AFM and STM topographic images were measured. The left panels of Fig. 7.1 show large area (> 1 μm) AFM images for Bi_2Te_3 samples with different Eu concentrations.

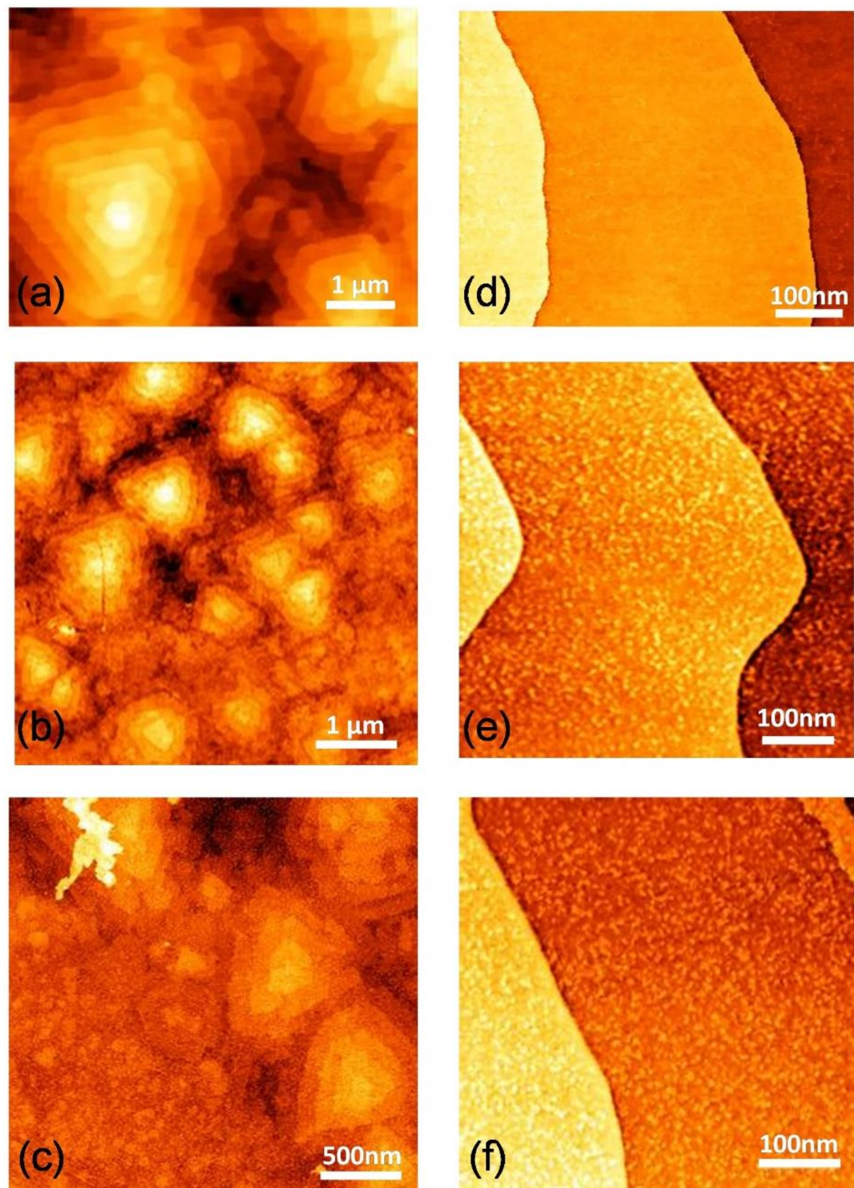

Figure 7.1: (left panels) large scale AFM topographic images for Bi_2Te_3 samples with different Eu concentrations, (a) Pure Bi_2Te_3, (b) 2% Eu-doped sample and (c) 11% Eu-doped sample. (Right panels) small scale STM topographic image on the surface of pure Bi_2Te_3 (d), 2% Eu-doped Bi_2Te_3 (e) and 11% Eu-doped Bi_2Te_3 (f). Eu-doped sample shows small protrusions distributed along the QL terraces. STM images were acquired using I = 400 pA and V= 1 V.

As observed, the surface morphology of films grown with 2% Eu (figure 7.1(b)) and 11% Eu (figure 7.1(c)) presents spiral-shaped triangular pyramids domains with terraces of approximate one QL height that are characteristic of the Bi_2Te_3 undoped phase (figure 7.1(a)) [160]. However, in the sample with 11% Eu it is possible to observe traces of segregation that may indicate an incomplete Eu incorporation in substitutional sites of the Bi_2Te_3 matrix for some regions along the surface.

A detailed view of these domains is provided by STM images presented in the right panels of figure 7.1. In these panels, the layered structure of pure Bi_2Te_3 (figure 7.1(d)) remains intact regardless of the presence of Eu in the films. However, for films grown with 2% (figure 7.1(e)) and 11% Eu (figure 7.1(f)) small protrusions distributed along the QL terraces can be observed. This fact, associated with the segregation region seen in the AFM images for the sample with 11% Eu, indicates that during the epitaxial growth process, Eu atoms are not completely inserted into the Bi_2Te_3 crystal structure, clustering at the surface.

The presence of protrusions or possible clusters associated with the Europium deposition process was investigated by performing several AFM measurements along different regions of the surface of the Eu-doped films. Some of these measures are shown in figure 7.2, for 2% Eu doped films (left panel) and for 11% Eu films (right panel). Differently from what was observed in previous studies where clusters start to appears at a threshold of Eu concentration above 4% [47], the AFM images represented in figure 7.2(a) indicate the presence of clusters in the sample grown with 2% Eu. In addition, small clusters are observed located on the terrace of the QL, as observed in figure 7.2(b). In the sample with 11% Eu, the presence of clusters and regions of possible Europium segregation is more evident (figure 7.2(c)). Furthermore, for this concentration of Eu it is possible to find regions along the sample surface whose morphology changes drastically as shown in figure 7.2(d), where the pyramidal domains appear to be completely covered with Eu atoms or other crystalline phases such as EuTe.

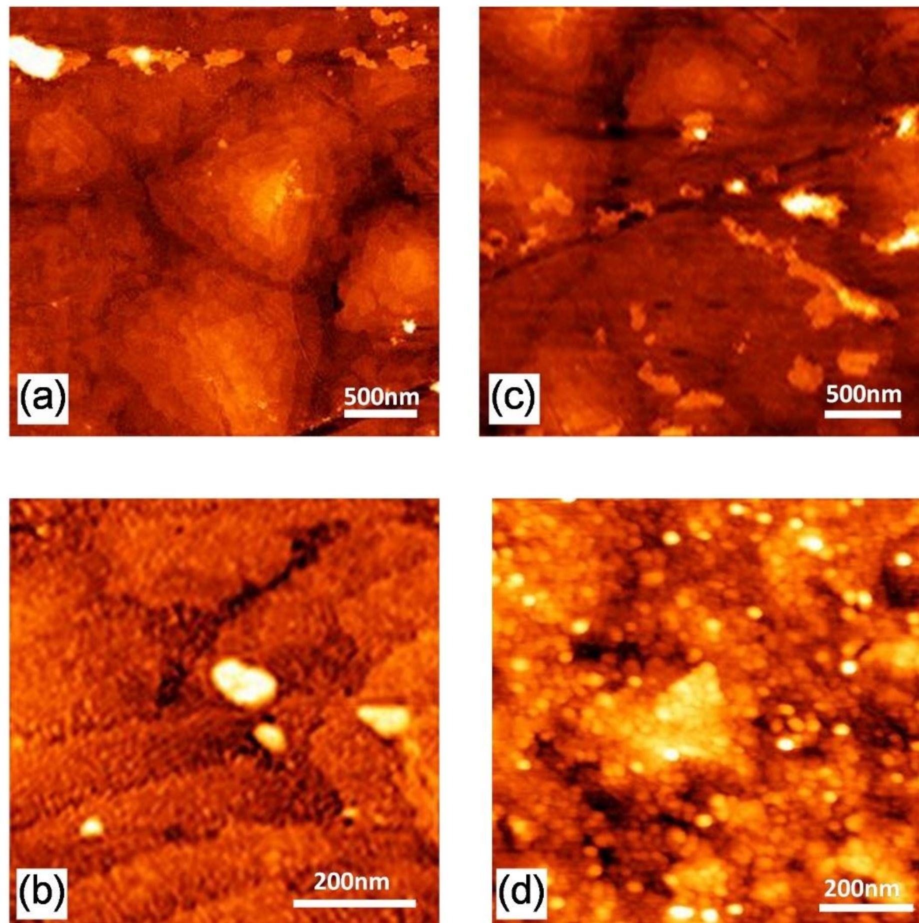

Figure 7.2: AFM topographic image showing protrusions or possible clusters associated with the Europium deposition process distributed along the Bi_2Te_3 surface for the sample grown with 2% Eu (a) and for the sample grown with 11% Eu (b). Figs (c) and (d). An extreme case where the region is characterized by an all-covered surface is shown in (d).

7.3.2. Raman characterization

The possibility of formation of other phases during the Europium doping process was investigated by Raman spectroscopy. As described in the Methods section, the excitation laser probes an area of 1x1 μm^2 at the sample region, which makes it possible to study the areas where some clusters are present. Figure 7.3(a) shows the Raman spectra obtained for Bi_2Te_3 films grown with different Eu concentrations ranging from 0% (undoped sample), 2% and 11%. In addition to the three expected phonon modes for the Bi_2Te_3 phase A_{1g}^1, E_g^2 and A_{1g}^2, for samples with 2% and 11% Eu there are additional peaks located at positions 110 cm^{-1}, 246 cm^{-1} and 287 cm^{-1}.

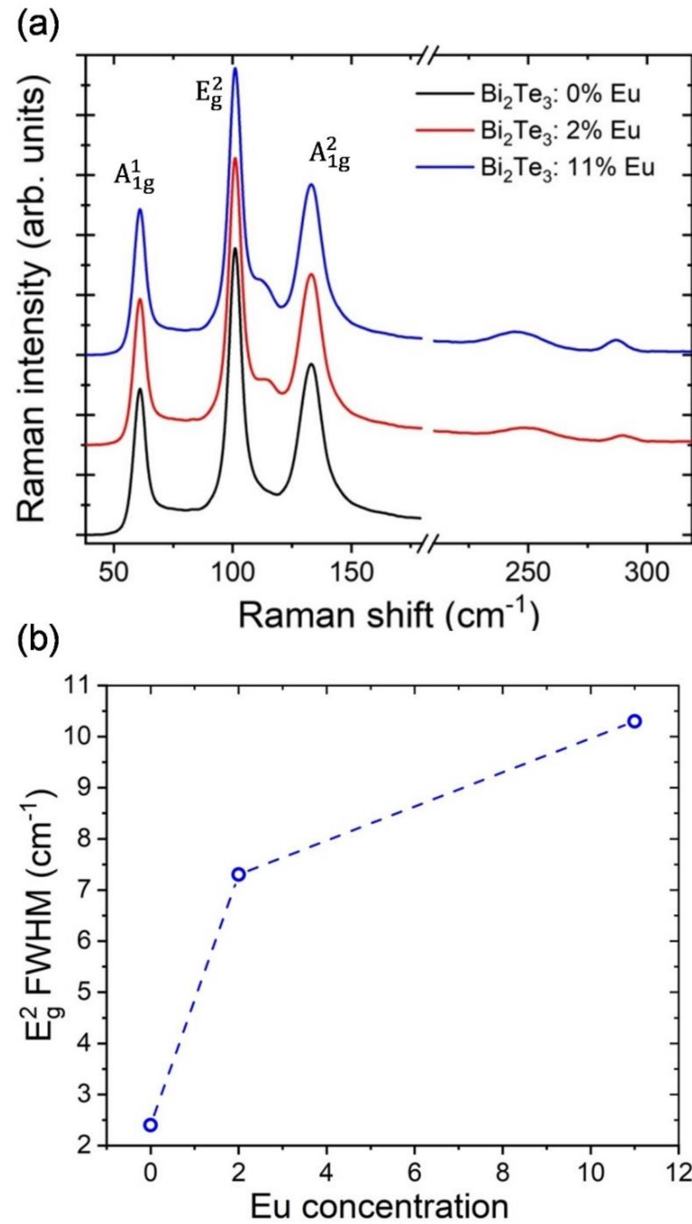

Figure 7.3: (a) Bi_2Te_3 Raman spectra as a function of Europium concentration. In addition to the three characteristic peaks of the Bi_2Te_3 phase (A_{1g}^1, E_g^2 and A_{1g}^2), it is possible to observe three additional peaks in the doped samples that matched with the EuTe phase indicating the coexistence of a secondary phase for some regions of the doped samples. (b) The Full Width at Height Maximum (FWHM) of the E_g^2 mode as a function of Eu concentration.

These three additional peaks are close to positions expected for the EuTe phase [189, 190], which indicates that the presence of Eu atoms on the surface of Bi_2Te_3 may favor the formation of a second phase where atomic planes of Eu and Te are stacked along the growth direction according to ref. [47] or are forming clusters of cubic EuTe (rock-salt

structure). Based on this evidence and on previous X-ray diffraction studies, the clusters observed in the AFM images for the Eu-doped samples can be associated with the EuTe phase and this secondary phase forms already in the low Europium concentration regime (2% Eu-doped samples).

Additionally, it is important to notice that some Raman spectra (depending on sample region) show a broadening of the peak associated with the in-plane vibration mode E_g^2 as the concentration of Eu in the films increases, as evaluated in figure 7.3(b). This broadening, which is more evident for Bi_2Te_3 samples with 11% Eu, can be attributed to disorder and inhomogeneity effects and a stronger eletron-phonon interactions which result in a reduction of phonon lifetime in the presence of magnetic impurities [71, 72].

7.3.3. Electronic characterization

After analyzing the impact of Eu atoms on the morphology of bismuth telluride thin films, in this section we will address the effects of the incorporation of Eu on the electronic properties of Bi_2Te_3. A series of STS measurements (single point and area spectroscopy) were performed at several points on the surface of Bi_2Te_3 films, basically considering three regions: far from any cluster, in the vicinity of clusters and at top clusters. A measurement of the local density of states (LDOS) on Bi_2Te_3 sample surface with different Eu concentrations provides important information of the topological surface states behavior.

The STS spectrum shown in figure 7.4(a) was measured in the undoped sample and is taken as a reference for the analysis of the spectra referring to the Eu-doped samples. In this spectrum the curve inflection points named E_{BCB} and E_{BVB} (grey dashed vertical lines) determine the bottom of the bulk conduction band (BCB) and the top of the bulk valence band (BVB), respectively. The linear conductance region located in the bulk band gap represents the topological surface states, with the Dirac point energy (E_D) obtained through the intersection of the red dashed line with the zero-conductance line. This procedure was discussed in section 3.2.2.2. In bismuth telluride the Dirac point is situated below the top of the BVB and cannot be obtained directly through STS measurements [172]. In all STS curves the zero energy (Bias voltage) marks the Fermi level (E_F).

STS curves in regions away from any detectable EuTe cluster are shown in figures 7.4(b) and (c) for samples with 2% and 11% Eu, respectively. Although in some of these regions small Eu protrusions are observed (see left panels of figure 7.1), this is not enough to destroy the topological surface states since the linear conductance region is still visible in these curves, being comparable to the spectrum before the Europium deposition. However, the presence of Eu atoms on the Bi_2Te_3 surface shifts the Dirac point to more negative energies (E_D= -260 meV for 2% Eu and E_D= -398 meV for 11% Eu) when compared to the undoped sample value (E_D= -215 meV), indicating a possible n-type surface doping. In addition, the spectra are broader and a shift in the BCB minimum and BVB maximum is also observed, increasing the value of the bulk energy gap (E_g) in these regions, this effect is more evident for the sample with 11% Eu. The energy gap for Bi_2Te_3 was experimentally determined by resistivity measurements and ARPES technique. Values of ~ 0.17 eV were retrieved [191-193].

On the other hand, the STS spectra change severely when measurements are performed in regions with higher concentration of protrusions and clusters. For samples with 2% Eu, the STS spectra (figure 7.4(d)) show a plateau region with zero conductance that resembles the STS expected for semiconductor materials. This suggests that there are regions along the Bi_2Te_3 surface where the signature of the surface states disappears, opening a gap in the Dirac cone. In addition, there is a variation in the value of the energy gap (see dashed horizontal lines) possibly associated with the non-uniform incorporation of Eu atoms in the crystalline structure of Bi_2Te_3 thin films during the epitaxial growth. For samples with 11% Eu these features are more pronounced, exhibiting higher gap values, as shown in figure 7.4(e).

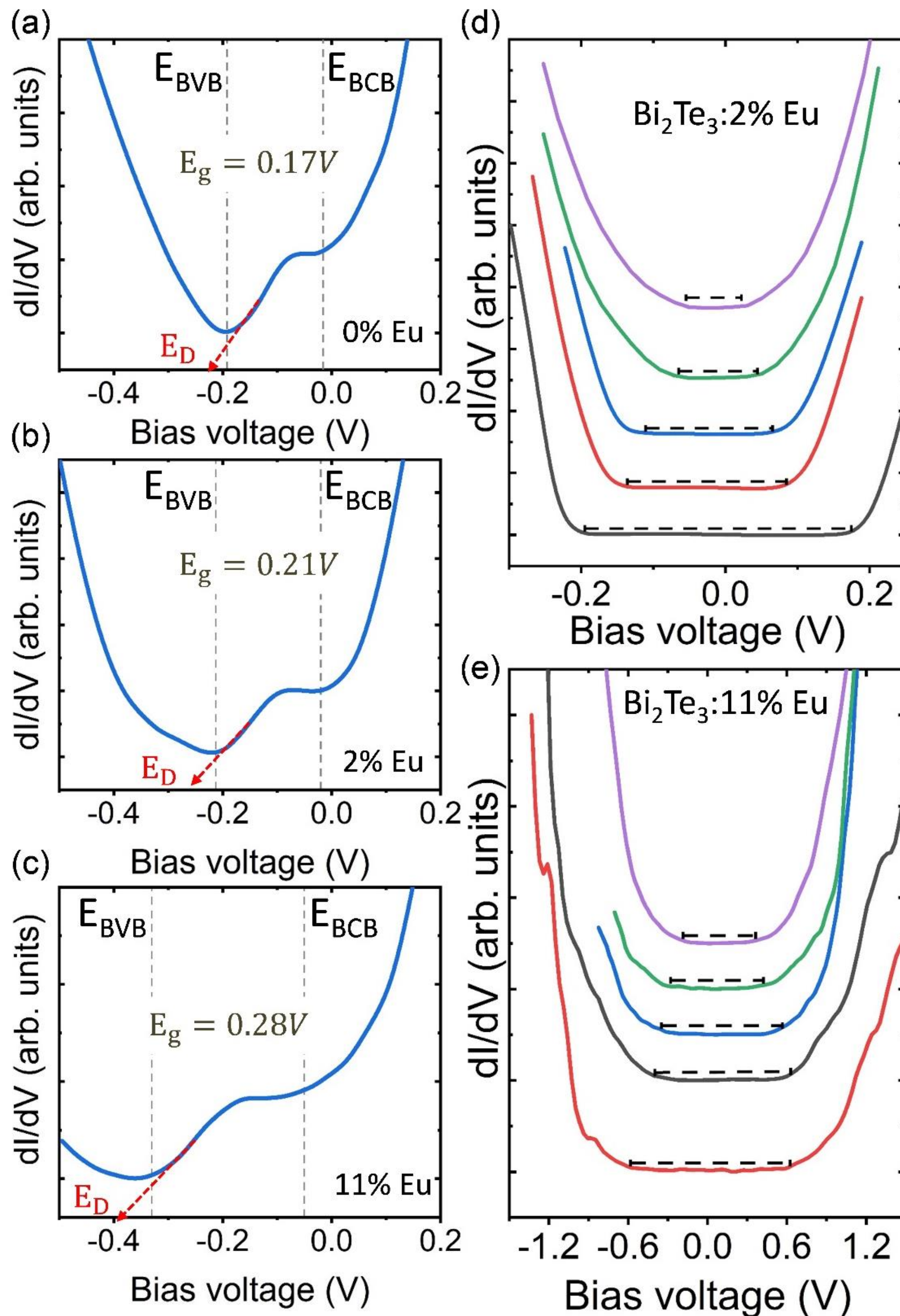

Figure 7.4: (left panels) A serie of representative STS spectra taken at points along the sample surface where the signature of the surface states appears as a function of Europium concentrations. (a) pure Bi_2Te_3, (b) 2% Eu-doped and (c) 11% Eu-doped. The Dirac point energy (E_D) is represented by the red dashed line and obtained by extrapolating the region of the curve in which the differential conductance (dI/dV) is linear. The edges of BVB and BCB determining the bandgap are marked with grey dashed vertical line. (Right panels) A series of representative STS spectra taken at points along the sample surface where the signature of the surface states disappears exhibiting a variable energy gap (region of zero differential conductance) for (d) 2% Eu-doped sample and (f) 11% Eu-doped sample. It is important to note that the graphs are not represented with the x-axis on the same scale for better visualization.

7.4. Discussion

The behavior of both Dirac point and bandgap observed in STS measurements for Bi_2Te_3 samples with different Eu concentrations can be quantified analyzing the histograms shown in figures 7.5 and 7.6. The first set of histograms (figure 7.5) were obtained from a minimum of 100 STS curves for each sample, measured across regions of the sample surface without visible clusters, whereas the second set of histograms (figure 7.6) was built from a minimum of 40 STS spectra for each sample with non-zero Eu concentration, measured in regions characterized by the presence of small protrusions and clusters. It is important to highlight that along the AFM/STM measurements these regions (protusions) are less common, showing that, regardless of the concentration of Eu, films are mostly similar to pristine Bi_2Te_3.

In the histograms shown in figure 7.5, the Dirac point energy (E_D) was determined by extrapolating the linear region of the STS spectra that characterizes the existence of surface states as described in the previous section. Starting with the undoped sample (0% Eu), a set of STS measurements along the film surface resulted in an average Dirac point energy of E_D = -230 ± 8 meV, which is in agreement with the values determined by ARPES [66]. In contrast, the retrieved mean E_D values for different Eu concentration are -280 ± 10 meV for 2% Eu and -385 ± 12 meV for 11% Eu, indicating that E_D shifts to less negative energies with respect to its Fermi energy when Eu concentration increases.

Since STS is a surface-sensitive technique, this E_D displacement may be related to disorder and inhomogeneity in the topmost QL due to the presence of non-incorporated Eu atoms in the Bi_2Te_3 crystal lattice. It is important to mention that previous studies have shown that there is a tendency for Europium to occupy Bismuth sites at low Europium concentration regime (< 4% Eu) and to favor the formation of the EuTe phase at samples with higher Europium concentration (> 4% Eu). Here we speculate that there is a competition between these two effects in the samples with 2% and 11% Eu. The formation of the EuTe phase is more probable for the sample with 11% Eu, which is characterized by a larger occurrence of Tellurium vacancies. Such effect may explain the fact that the Dirac

point of this sample is shifted towards more negative bias (larger n-type doping) than in the 2% Eu-doped sample in the regions where the topological surface states appear.

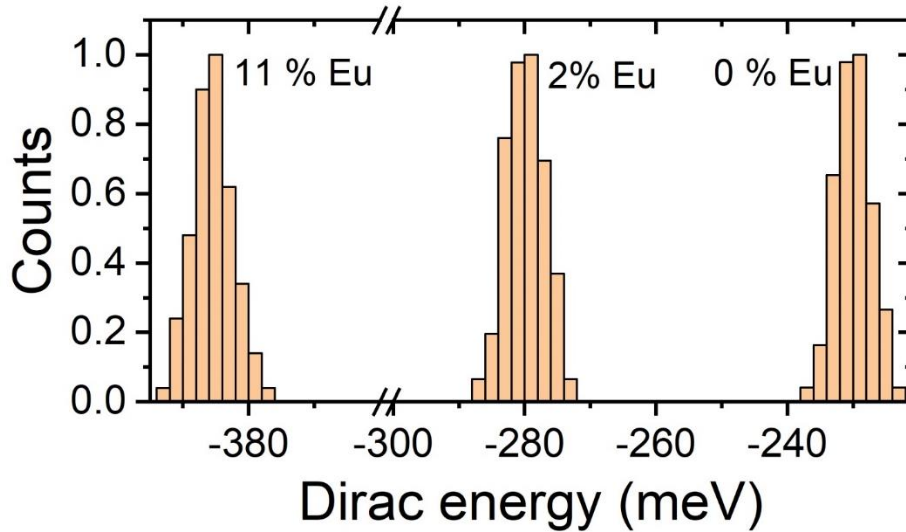

Figure 7.5: Histogram of Dirac energy (E_D) obtained from STS results on undoped (pristine Bi_2Te_3), 2% Eu-doped sample and 11% Eu-doped sample. A Gaussian function has been fitted to each histogram to quantify the mean Dirac energy value.

Another important issue is observed through the spectra that indicate the existence of a gap-like structure in some regions of the Bi_2Te_3 samples doped with Europium. The histograms in figure 7.6 show that the sample with 2% Eu has an average energy gap value of E_g = 0.22 ± 0.05 V while for the sample with 11% Eu this value increases to about E_g= 0.8 ± 0.2 V, this behavior may indicate a local suppression of the topological protection due to Eu doping. Indeed, for 2% Eu-doped Bi_2Te_3 films an energy gap of the order of 0.2 V is consistent with the expected gap value for the pure Bi_2Te_3 semiconductor material. Furthermore, the histogram indicates that in this sample the measured energy gap fluctuation is reduced around the mean value when compared to the values obtained in the sample with 11% Eu, suggesting that the substitutional incorporation of Europium atoms into the Bi_2Te_3 matrix is more effective in a low concentration regime.

Considering the sample with 11% Eu, the high values of energy gap found and the larger variation with respect to the mean value may indicate a possible local coexistence between Bi_2Te_3, Eu_x ($Bi_{2-x}Te_3$) and EuTe phases due to the enhanced availability of Eu atoms on the surface and non-uniform incorporation into the Bi_2Te_3 crystalline structure. The

energy gap values obtained in regions very close to the clusters can better elucidate this scenario.

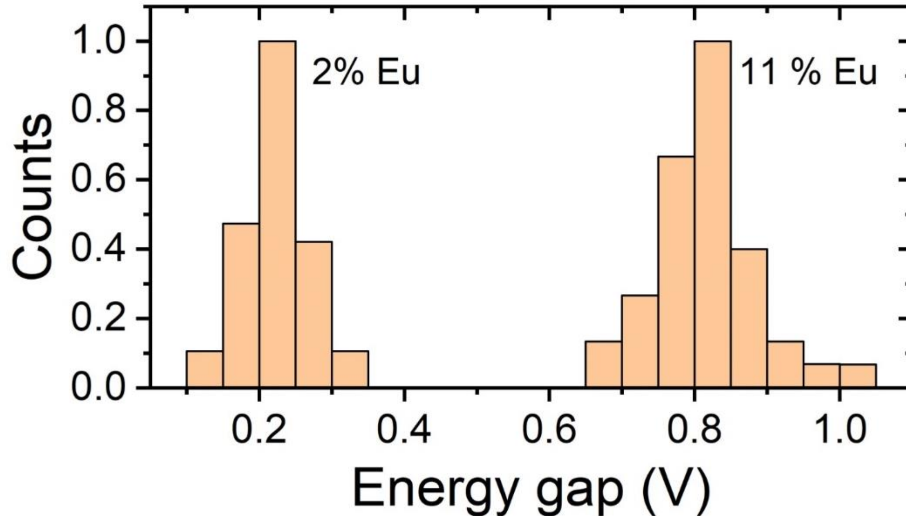

Figure 7.6: Histogram of Energy gap (E_g) obtained from STS results on 2% Eu-doped sample and 11% Eu-doped sample. A Gaussian fitting was employed to each histogram to quantify the mean Energy gap value.

Finally, figure 7.7 shows a STM image (left side) in a region very close to a cluster in the sample with 11% Eu. In the vicinity of the cluster, the film surface appears to be rough with no apparent step indicating poor crystalline quality. Furthermore, a series of STS shows the behavior of LDOS as a function of the distance to the cluster. The STS measured at each colored dot is shown in the right side of the figure 7.7 and allows to observe a monotonic increase in the gap value as the distance to the cluster decreases. Over the cluster, a set of STS spectra (histogram shown in inset) shows an average energy gap value of approximately 2.0 ± 0.3 eV which is consistent with the expected value for EuTe crystals (E_g ~ 2.4 eV) [194]. This corroborates the fact that a second phase is formed during the epitaxial growth process, as also observed in the Raman measurements. Furthermore, the presence of such EuTe clusters on the surface modifies the Bi_2Te_3 electronic properties in such a way that the signature of the topologically protected surface states disappears on its vicinity.

In order to clarify the main mechanisms associated with the gap opening process, ab initio calculations are necessary. Here, we can argue that as the gap opening in these samples was not observed in ARPES measurements. However, the typical beam size in ARPES system does not allow probing areas with a spatial resolution comparable to

cluster/protrusion sizes, providing an average result (closer to pure Bi_2Te_3) while STM/STS results are able to probe purely local phenomena.

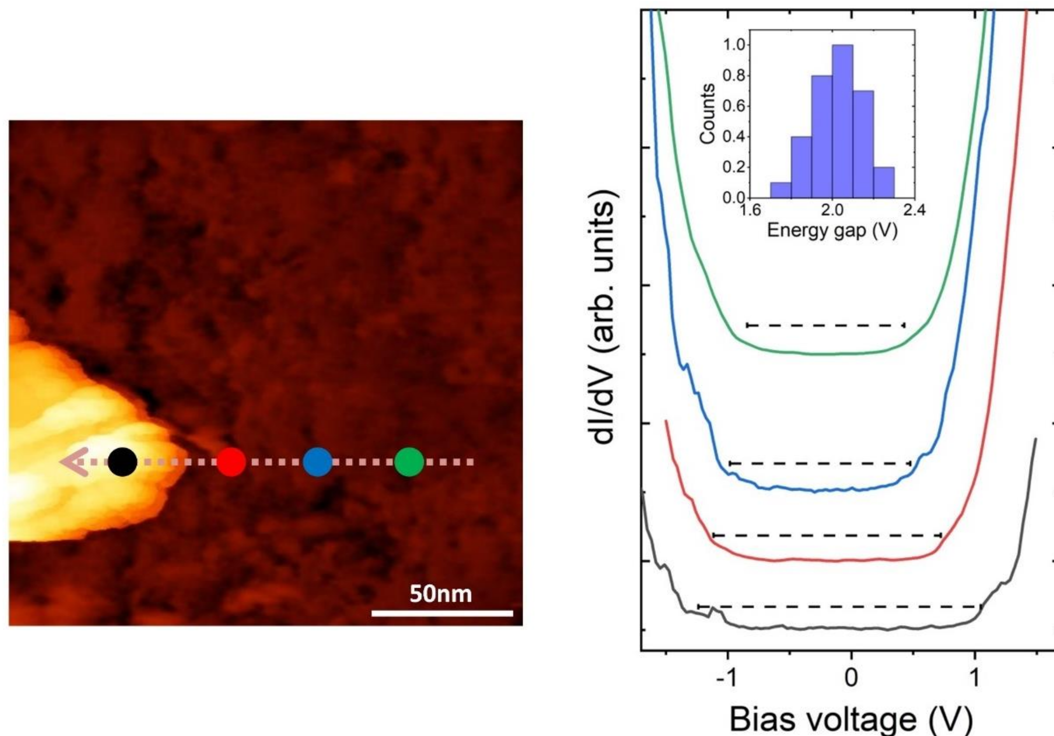

Figure 7.7: Detailed constant-current STM image (left side) in the vicinity of a cluster and Local Density of States (LDOS) as a function of cluster distance (right side) measured by STS at the points indicated by colored dots. Inset shows the histogram that accounts the energy gap values over the cluster. Image acquired at I = 500 pA and V= 1 V.

7.4. Conclusion

In this chapter, we study the effect of the incorporation of Europium atoms in Bi_2Te_3 films grown by the MBE technique. A set of samples with different Europium concentrations were grown (pure Bi_2Te_3, 2% and 11% Eu) and show different morphological and electronic characteristics.

AFM and STM measurements show that, regardless of the Europium concentration in the films, the samples presented topography similar to that expected for pristine Bi_2Te_3 with pyramidal triangular domains distributed along the substrate surface. However, some AFM/STM measurements also indicate the presence of cluster-type defects that are associated with the presence of Europium in Bi_2Te_3 films. Furthermore, Raman

spectroscopy measurements indicate an increase in disorders in the films as well as the formation of the EuTe phase for both Europium concentrations (2% and 11%).

Although ARPES measurements on Europium-doped Bi_2Te_3 samples showed the presence of an intact Dirac cone indicating that surface states exist even in the presence of magnetic impurities, our STS measurements points out that considerable gaps appear already in the low Eu concentration regime. This fact indicates that along the sample surface there are regions in which the presence of magnetic disorders acts locally on the surface states due to the incomplete incorporation of Eu atoms in the crystalline matrix of the Bismuth telluride. An extreme case is the formation of a second EuTe phase that has insulating properties.

8. General conclusions

Throughout this thesis a set of experimental techniques was used in order to study the structural and electronic properties of silicon-germanium and bismuth telluride samples grown by molecular beam epitaxy (MBE) technique.

On the SiGe samples, the germanium (Ge) concentration, thickness and strain in the epitaxial layers were systematically studied through the techniques of x-ray diffraction, x-ray reflectivity and ULE-SIMS as a function of the oxidation time, during the Ge condensation process. The results presented here indicate the existence of a non-monotonic strain in the SiGe layers as the Ge concentration increases in the layers. Furthermore, a comparison between the results obtained by x-ray diffraction and x-ray reflectivity/ SIMS indicates an oxidation time threshold at which the formation of an amorphous layer occurs. After the evaluation of Ge content, the strain sensitive process of rolling-up tubes from the flat layers is used and combined with X-ray diffraction to provide a concise scenario of the strain evolution along an in-growth oxidation series, pointing out the conditions that maximize strain, as well as its fading as the Ge content rises.

Regarding Bi_2Te_3 samples grown on HOPG graphite, a series of samples were analyzed as a function of growth time. The samples were characterized by the techniques of atomic force microscopy, X-ray diffraction and Raman spectroscopy. The analysis of AFM images showed isolated islands of hexagonal shape, characteristic of the Bi_2Te_3 phase. Furthermore, after a critical coverage (about 8 QL), changes in the stoichiometry of the deposited material and, therefore, the emergence of new phases were observed. Through diffraction measurements and Raman spectroscopy, it was possible to observe the existence of in-plane and out-of-plane strain in the first layers of deposited material, an uncommon fact in this type of epitaxy. The experimental results found here were used to calculate elastic constants of bismuth bilayers (Bi_2), which are crucial building blocks for the formation of other Bi_xTe_y topological insulator compounds. Futhermore, the impact of such strain in Bi_2Te_3 electronic structure was investigated by DFT calculations. The results show that band structure of this strained material remains unchanged at the center of Brillouin zone

confirming the robustness of surface states, but it is consistently affected at the M and K zone edges.

Finally, Europium-doped Bi_2Te_3 thin films were grown in order to analyze the effect of atoms with magnetic properties on topologically protected surface states. Our results indicated that during the epitaxial growth process, Eu atoms are not fully incorporated into the Bi_2Te_3 matrix. Through the AFM/STM techniques, the morphology of the films as a function of the Europium concentration was analyzed. The results showed that regardless of the Eu concentration, the layered structure characteristic of the Bi_2Te_3 phase was mostly maintained. However, protrusions and clusters on the surface of the films were also observed. The STS measurements indicate gap spectra for some regions of the sample, which may be associated with the destruction of surface states due to the presence of Eu atoms. Furthermore, on top of the clusters, the STS results indicate spectra with a gap of the order of 2.0 eV, a characteristic value of the EuTe phase.

References

[1] Bardeen, J., & Brattain, W. H. (1948). The transistor, a semi-conductor triode. *Physical Review*, *74*(2), 230.

[2] Mollick, E. (2006). Establishing Moore's law. *IEEE Annals of the History of Computing*, *28*(3), 62-75.

[3] Semond, F., Cordier, Y., Grandjean, N., Natali, F., Damilano, B., Vézian, S., & Massies, J. (2001). Molecular Beam Epitaxy of Group-III Nitrides on Silicon Substrates: Growth, Properties and Device Applications. *physica status solidi (a)*, *188*(2), 501-510.

[4] Kolodzey, J., O'neil, P. A., Zhang, S., Orner, B. A., Roe, K., Unruh, K. M., ... & Shah, S. I. (1995). Growth of germanium-carbon alloys on silicon substrates by molecular beam epitaxy. *Applied physics letters*, *67*(13), 1865-1867.

[5] Zhang, Y., Aagesen, M., Holm, J. V., Jørgensen, H. I., Wu, J., & Liu, H. (2013). Self-catalyzed GaAsP nanowires grown on silicon substrates by solid-source molecular beam epitaxy. *Nano letters*, *13*(8), 3897-3902.

[6] Souriau, L. (2012). Fabrication of (Silicon)-Germanium on insulator substrates by the germanium condensation technique (PhD thesis).

[7] Sun, Y., Thompson, S. E., & Nishida, T. (2007). Physics of strain effects in semiconductors and metal-oxide-semiconductor field-effect transistors. *Journal of Applied Physics*, *101*(10), 104503.

[8] Fischetti, M. V., Ren, Z., Solomon, P. M., Yang, M., & Rim, K. (2003). Six-band k· p calculation of the hole mobility in silicon inversion layers: Dependence on surface orientation, strain, and silicon thickness. *Journal of Applied Physics*, *94*(2), 1079-1095.

[9] Grundmann, M., Stier, O., & Bimberg, D. (1995). InAs/GaAs pyramidal quantum dots: Strain distribution, optical phonons, and electronic structure. *Physical Review B*, *52*(16), 11969.

[10] Schäffler, F. (1997). High-mobility Si and Ge structures. *Semiconductor Science and Technology*, *12*(12), 1515.

[11] Sun, Y., Thompson, S. E., & Nishida, T. (2009). *Strain effect in semiconductors: theory and device applications*. Springer Science & Business Media.

[12] Nieto, J. M., & Comas, F. (2007). Polar optical phonons in a semiconductor quantum-well: The complete matching problem. *Physica B: Condensed Matter*, *388*(1-2), 153-158.

[13] Liu, F., Wu, F., & Lagally, M. G. (1997). Effect of strain on structure and morphology of ultrathin Ge films on Si (001). *Chemical reviews*, *97*(4), 1045-1062.

[14] Analytis, J. G., Chu, J. H., Chen, Y., Corredor, F., McDonald, R. D., Shen, Z. X., & Fisher, I. R. (2010). Bulk Fermi surface coexistence with Dirac surface state in Bi_2Se_3: A comparison of photoemission and Shubnikov–de Haas measurements. *Physical Review B*, *81*(20), 205407.

[15] Lawson, B. J., Corbae, P., Li, G., Yu, F., Asaba, T., Tinsman, C., ... & Li, L. (2016). Multiple Fermi surfaces in superconducting Nb-doped Bi_2Se_3. *Physical Review B*, *94*(4), 041114.

[16] Tarasenko, R., Vališka, M., Vondráček, M., Horáková, K., Tkáč, V., Carva, K., ... & Honolka, J. (2016). Magnetic and structural properties of Mn-doped Bi2Se3 topological insulators. *Physica B: Condensed Matter*, *481*, 262-267.

[17] Hasan, M. Z., & Moore, J. E. (2011). Three-dimensional topological insulators. *Annu. Rev. Condens. Matter Phys.*, *2*(1), 55-78.

[18] Ashcroft, N. W., & Mermin, N. D. (1993). Solid State Physics (Brooks Cole, 1976). *Cited on*, *26*.

[19] Zhang, H., Liu, C. X., Qi, X. L., Dai, X., Fang, Z., & Zhang, S. C. (2009). Topological insulators in Bi_2Se_3, Bi_2Te_3 and Sb_2Te_3 with a single Dirac cone on the surface. *Nature physics*, *5*(6), 438-442.

[20] Walsh, L. A., & Hinkle, C. L. (2017). van der Waals epitaxy: 2D materials and topological insulators. *Applied Materials Today*, *9*, 504-515.

[21] Xiu, F., He, L., Wang, Y., Cheng, L., Chang, L. T., Lang, M., ... & Wang, K. L. (2011). Manipulating surface states in topological insulator nanoribbons. *Nature nanotechnology*, *6*(4), 216-221.

[22] Zyuzin, A. A., & Burkov, A. A. (2011). Thin topological insulator film in a perpendicular magnetic field. *Physical Review B*, *83*(19), 195413.

[23] Zyuzin, A. A., Hook, M. D., & Burkov, A. A. (2011). Parallel magnetic field driven quantum phase transition in a thin topological insulator film. *Physical Review B*, *83*(24), 245428.

[24] Chang, C. Z., Zhang, J., Feng, X., Shen, J., Zhang, Z., Guo, M., ... & Xue, Q. K. (2013). Experimental observation of the quantum anomalous Hall effect in a magnetic topological insulator. *Science*, *340*(6129), 167-170.

[25] Cho, A. Y., & Arthur, J. R. (1975). Molecular beam epitaxy. *Progress in solid state chemistry*, *10*, 157-191.

[26] Herman, M. A., Richter, W., & Sitter, H. (2013). *Epitaxy: physical principles and technical implementation* (Vol. 62). Springer Science & Business Media.

[27] Barabasi, A. L. (1997). Self-assembled island formation in heteroepitaxial growth. *Applied physics letters*, *70*(19), 2565-2567.

[28] Cunningham, B., Chu, J. O., & Akbar, S. (1991). Heteroepitaxial growth of Ge on (100) Si by ultrahigh vacuum, chemical vapor deposition. *Applied physics letters*, *59*(27), 3574-3576.

[29] Utama, M. I. B., Zhang, Q., Zhang, J., Yuan, Y., Belarre, F. J., Arbiol, J., & Xiong, Q. (2013). Recent developments and future directions in the growth of nanostructures by van der Waals epitaxy. *Nanoscale*, *5*(9), 3570-3588.

[30] Koma, A. (1999). Van der Waals epitaxy for highly lattice-mismatched systems. *Journal of crystal growth*, *201*, 236-241.

[31] Tsao, J. Y. (2012). *Materials fundamentals of molecular beam epitaxy*. Academic Press.

[32] Agostini, G., & Lamberti, C. (Eds.). (2011). *Characterization of semiconductor heterostructures and nanostructures*. Elsevier.

[33] Shen, J., Johnston, S., Shang, S., & Anderson, T. (2002). Calculated strain energy of hexagonal epitaxial thin films. *Journal of crystal growth*, *240*(1-2), 6-13.

[34] Mendelson, B. (1990). *Introduction to topology*. Courier Corporation.

[35] Qi, X. L., & Zhang, S. C. (2011). Topological insulators and superconductors. *Reviews of Modern Physics*, *83*(4), 1057.

[36] Fu, L., & Kane, C. L. (2007). Topological insulators with inversion symmetry. *Physical Review B*, *76*(4), 045302.

[37] Fu, L., Kane, C. L., & Mele, E. J. (2007). Topological insulators in three dimensions. *Physical review letters*, *98*(10), 106803.

[38] Ando, Y. (2013). Topological insulator materials. *Journal of the Physical Society of Japan*, *82*(10), 102001.

[39] Kane, C. L., & Mele, E. J. (2006). A new spin on the insulating state. *Science*, *314*(5806), 1692-1693.

[40] Kane, C. L., & Mele, E. J. (2005). Z 2 topological order and the quantum spin Hall effect. *Physical review letters*, *95*(14), 146802.

[41] Qi, X. L., & Zhang, S. C. (2010). The quantum spin Hall effect and topological insulators. arXiv preprint arXiv:1001.1602.

[42] Zhang, W., Yu, R., Zhang, H. J., Dai, X., & Fang, Z. (2010). First-principles studies of the three-dimensional strong topological insulators Bi_2Te_3, Bi_2Se_3 and Sb2Te3. *New Journal of Physics*, *12*(6), 065013.

[43] Konig, M., Wiedmann, S., Brune, C., Roth, A., Buhmann, H., Molenkamp, L. W., Qi, X. L. & Zhang, S. C. (2007). Quantum spin Hall insulator state in HgTe quantum wells. *Science*, *318*(5851), 766-770.

[44] Chen, Y. L., Chu, J. H., Analytis, J. G., Liu, Z. K., Igarashi, K., Kuo, H. H., Qi, X. L., Mo, S. K., Moore, R. G., Lu, D. H., Hashimoto, M., Sasagawa, T., Zhang, S. C., Fisher, I. R., Hussain, Z. & Shen, Z. X. (2010). Massive Dirac fermion on the surface of a magnetically doped topological insulator. *Science*, *329*(5992), 659-662.

[45] Kou, X., Fan, Y., Lang, M., Upadhyaya, P., & Wang, K. L. (2015). Magnetic topological insulators and quantum anomalous hall effect. *Solid State Communications*, *215*, 34-53.

[46] Scholz, M. R., Sánchez-Barriga, J., Marchenko, D., Varykhalov, A., Volykhov, A., Yashina, L. V., & Rader, O. (2012). Tolerance of topological surface states towards magnetic moments: Fe on Bi_2Se_3. *Physical Review Letters*, *108*(25), 256810.

[47] Fornari, C. I., Bentmann, H., Morelhão, S. L., Peixoto, T. R., Rappl, P. H., Tcakaev, A. V., ... & Abramof, E. (2020). Incorporation of Europium in Bi_2Te_3 Topological Insulator Epitaxial Films. *The Journal of Physical Chemistry C*, *124*(29), 16048-16057.

[48] Nakaharai, S., Tezuka, T., Sugiyama, N., Moriyama, Y., & Takagi, S. I. (2003). Characterization of 7-nm-thick strained Ge-on-insulator layer fabricated by Ge-condensation technique. *Applied Physics Letters*, *83*(17), 3516-3518.

[49] Abstreiter, G., Brugger, H., Wolf, T., Jorke, H., & Herzog, H. J. (1985). Strain-induced two-dimensional electron gas in selectively doped Si/Si_xGe_{1-x} superlattices. *Physical review letters*, *54*(22), 2441.

[50] Paul, D. J. (1999). Silicon-Germanium strained layer materials in microelectronics. *Advanced Materials*, *11*(3), 191-204.

[51] Maiti, C. K., Chakrabarti, N. B., & Ray, S. K. (Eds.). (2001). *Strained silicon heterostructures: materials and devices* (No. 12). IET.

[52] Kasper, E., & Lyutovich, K. (2004). Strain adjustment with thin virtual substrates. *Solid-State Electronics*, *48*(8), 1257-1263.

[53] Kasper, E., & Herzog, H. J. (2011). Structural properties of silicon–germanium (SiGe) nanostructures. In *Silicon–Germanium (SiGe) Nanostructures* (pp. 3-25). Woodhead Publishing.

[54] Thurmond, C. D. (1953). Equilibrium thermochemistry of solid and liquid alloys of germanium and of silicon. I. The solubility of Ge and Si in elements of groups III, IV and V. *The Journal of Physical Chemistry*, *57*(8), 827-830.

[55] Hassion, F. X., Goss, A. J., & Trumbore, F. A. (1955). On the Germanium-Silicon phase diagram. *The Journal of Physical Chemistry*, *59*(10), 1118-1119.

[56] Salm, C. (1997). Advanced germanium-silicon for advanced CMOS Technologies (PhD thesis).

[57] Harame, D. L., Koester, S. J., Freeman, G., Cottrel, P., Rim, K., Dehlinger, G., ... & Subbanna, S. (2004). The revolution in SiGe: Impact on device electronics. *Applied Surface Science*, *224*(1-4), 9-17.

[58] Geppert, L. (1999). Solid state [semiconductors. 1999 technology analysis and forecast]. *IEEE Spectrum*, *36*(1), 52-56.

[59] Van de Walle, C. G., & Martin, R. M. (1986). Theoretical calculations of heterojunction discontinuities in the Si/Ge system. *Physical Review B*, *34*(8), 5621.

[60] Cavallo, F. (2009). Strain driven architecture of Si-based nanomembranes (PhD thesis).

[61] Peranio, N., Eibl, O., & Nurnus, J. (2006). Structural and thermoelectric properties of epitaxially grown Bi_2Te_3 thin films and superlattices. *Journal of Applied Physics*, *100*(11), 114306.

[62] Hicks, L. D., & Dresselhaus, M. S. (1993). Effect of quantum-well structures on the thermoelectric figure of merit. *Physical Review B*, *47*(19), 12727.

[63] Mishra, S. K., Satpathy, S., & Jepsen, O. (1997). Electronic structure and thermoelectric properties of bismuth telluride and bismuth selenide. *Journal of Physics: Condensed Matter*, *9*(2), 461.

[64] Bos, J. W. G., Zandbergen, H. W., Lee, M. H., Ong, N. P., & Cava, R. J. (2007). Structures and thermoelectric properties of the infinitely adaptive series $(Bi_2)_m(Bi_2Te_3)_n$. *Physical Review B*, *75*(19), 195203.

[65] Thakur, V., Upadhyay, K., Kaur, R., Goyal, N., & Gautam, S. (2020). Investigating phase transition and morphology of Bi-Te thermoelectric system. *Materials Today Advances*, 8, 100082.

[66] Fornari, C. I. (2017). Propriedades de filmes finos do isolante topológico telureto de bismuto crescidos por epitaxia de feixe molecular (tese de doutorado), INPE, São José dos Campos.

[67] Urazhdin, S., Bilc, D., Mahanti, S. D., Tessmer, S. H., Kyratsi, T., & Kanatzidis, M. G. (2004). Surface effects in layered semiconductors Bi_2Se_3 and Bi_2Te_3. *Physical Review B*, *69*(8), 085313.

[68] Larson, P., Mahanti, S. D., & Kanatzidis, M. G. (2000). Electronic structure and transport of Bi_2Te_3 and $BaBiTe_3$. *Physical Review B*, *61*(12), 8162.

[69] Alpichshev, Z., Analytis, J. G., Chu, J. H., Fisher, I. R., Chen, Y. L., Shen, Z. X., ... & Kapitulnik, A. (2010). STM imaging of electronic waves on the surface of Bi_2Te_3: topologically protected surface states and hexagonal warping effects. *Physical review letters*, *104*(1), 016401.

[70] Li, Y. Y., Wang, G., Zhu, X. G., Liu, M. H., Ye, C., Chen, X., ... & Xue, Q. K. (2010). Intrinsic topological insulator Bi_2Te_3 thin films on Si and their thickness limit. *Advanced materials*, *22*(36), 4002-4007.

[71] Wang, C., Zhu, X., Nilsson, L., Wen, J., Wang, G., Shan, X., ... & Xue, Q. (2013). In situ Raman spectroscopy of topological insulator Bi_2Te_3 films with varying thickness. *Nano Research*, *6*(9), 688-692.

[72] Richter, W., & Becker, C. R. (1977). A Raman and far-infrared investigation of phonons in the rhombohedral V_2–VI_3 compounds Bi_2Te_3, Bi_2Se_3, Sb_2Te_3 and $Bi_2(Te_{1-x}Se_x)_3$ (0< x< 1), $(Bi_{1-y}Sb_y)_2Te_3$ (0< y< 1). *physica status solidi (b)*, *84*(2), 619-628.

[73] Shahil, K. M. F., Hossain, M. Z., Goyal, V., & Balandin, A. A. (2012). Micro-Raman spectroscopy of mechanically exfoliated few-quintuple layers of Bi2Te3, Bi2Se3, and Sb2Te3 materials. *Journal of Applied Physics*, *111*(5), 054305.

[74] Humlíček, J., Hemzal, D., Dubroka, A., Caha, O., Steiner, H., Bauer, G., & Springholz, G. (2014). Raman and interband optical spectra of epitaxial layers of the topological insulators Bi2Te3 and Bi2Se3 on BaF2 substrates. *Physica Scripta*, *2014*(T162), 014007.

[75] Hayashi, T., Tanaka, M., Nishinaga, T., Shimada, H., Tsuchiya, H., & Otuka, Y. (1997). (GaMn) As: GaAs-based III–V diluted magnetic semiconductors grown by molecular beam epitaxy. *Journal of crystal growth*, *175*, 1063-1068.

[76] Kunkel, R., Poelsema, B., Verheij, L. K., & Comsa, G. (1990). Reentrant layer-by-layer growth during molecular-beam epitaxy of metal-on-metal substrates. *Physical review letters*, *65*(6), 733.

[77] Nakahara, K. N. K., Tanabe, T. T. T., Takasu, H. T. H., Fons, P. F. P., Iwata, K. I. K., Yamada, A. Y. A., ... & Niki, S. N. S. (2001). Growth of undoped ZnO films with improved electrical properties by radical source molecular beam epitaxy. *Japanese Journal of Applied Physics*, *40*(1R), 250.

[78] Koma, A. (1995). Molecular beam epitaxial growth of organic thin films. *Progress in crystal growth and characterization of materials*, *30*(2-3), 129-152.

[79] Als-Nielsen, J., & McMorrow, D. (2011). *Elements of modern X-ray physics*. John Wiley & Sons.

[80] Stangl, J., Daniel, A., Holý, V., Roch, T., Bauer, G., Kegel, I., ... & Eberl, K. (2001). Strain and composition distribution in uncapped SiGe islands from x-ray diffraction. *Applied Physics Letters*, *79*(10), 1474-1476.

[81] Mocuta, C., Stangl, J., Mundboth, K., Metzger, T. H., Bauer, G., Vartanyants, I. A., ... & Boeck, T. (2008). Beyond the ensemble average: X-ray microdiffraction analysis of single SiGe islands. *Physical Review B*, *77*(24), 245425.

[82] Schülli, T. U., Stoffel, M., Hesse, A., Stangl, J., Lechner, R. T., Wintersberger, E., ... & Bauer, G. (2005). Influence of growth temperature on interdiffusion in uncapped SiGe-islands on Si (001) determined by anomalous x-ray diffraction and reciprocal space mapping. *Physical Review B*, *71*(3), 035326.

[83] Oksanen, E., Jaakola, V. P., Tolonen, T., Valkonen, K., Åkerström, B., Kalkkinen, N., ... & Goldman, A. (2006). Reindeer β-lactoglobulin crystal structure with pseudo-body-centred noncrystallographic symmetry. *Acta Crystallographica Section D: Biological Crystallography*, *62*(11), 1369-1374.

[84] Cullity, B. D. (1956). *Elements of X-ray Diffraction*. Addison-Wesley Publishing.

[85] Hammond, C. (2015). *The basics of crystallography and diffraction* (Vol. 21). International Union of Crystal.

[86] Caha, O., Dubroka, A., Humlicek, J., Holy, V., Steiner, H., Ul-Hassan, M., ... & Springholz, G. (2013). Growth, structure, and electronic properties of epitaxial bismuth telluride topological insulator films on BaF2 (111) substrates. *Crystal growth & design*, *13*(8), 3365-3373.

[87] Birkholz, M. (2006). *Thin film analysis by X-ray scattering*. John Wiley & Sons.

[88] Pietsch, U., Holy, V., & Baumbach, T. (2004). *High-resolution X-ray scattering: from thin films to lateral nanostructures*. Springer Science & Business Media.

[89] Giessibl, F. J. (2003). Advances in atomic force microscopy. *Reviews of modern physics*, *75*(3), 949.

[90] Eaton, P., & West, P. (2010). *Atomic force microscopy*. Oxford university press.

[91] Tersoff, J., & Hamann, D. R. (1985). Theory of the scanning tunneling microscope. *Physical Review B*, *31*(2), 805.

[92] Binnig, G., Rohrer, H., Gerber, C., & Weibel, E. (1982). Surface studies by scanning tunneling microscopy. *Physical review letters*, *49*(1), 57.

[93] Ballentine, L. E. (2014). *Quantum mechanics: a modern development*. World Scientific Publishing Company.

[94] Binnig, G., & Rohrer, H. (1985). The scanning tunneling microscope. *Scientific American*, *253*(2), 50-58.

[95] Chen, C. J. (2008). Introduction to Scanning Tunneling Microscopy, Oxford University Press.

[96] Lounis, S. (2014). Theory of scanning tunneling microscopy. *arXiv preprint arXiv:1404.0961*.

[97] Gottlieb, A. D., & Wesoloski, L. (2006). Bardeen's tunnelling theory as applied to scanning tunnelling microscopy: a technical guide to the traditional interpretation. *Nanotechnology*, *17*(8), R57.

[98] Meyer, E., Hug, H. J., & Bennewitz, R. (2003). *Scanning probe microscopy* (Vol. 4). New York: Springer.

[99] Morris, P. R., & Bowers, B. (1990). *A history of the world semiconductor industry* (No. 12). IET.

[100] Luan, S., & Neudeck, G. W. (1992). An experimental study of the source/drain parasitic resistance effects in amorphous silicon thin film transistors. *Journal of Applied Physics*, *72*(2), 766-772.

[101] Celler, G. K., & Cristoloveanu, S. (2003). Frontiers of silicon-on-insulator. *Journal of Applied Physics*, *93*(9), 4955-4978.

[102] Lee, M. L., Fitzgerald, E. A., Bulsara, M. T., Currie, M. T., & Lochtefeld, A. (2005). Strained Si, SiGe, and Ge channels for high-mobility metal-oxide-semiconductor field-effect transistors. *Journal of applied physics*, *97*(1), 1.

[103] Ishikawa, Y., Shibata, N., & Fukatsu, S. (1999). SiGe-on-insulator substrate using SiGe alloy grown Si (001). *Applied physics letters*, *75*(7), 983-985.

[104] Tezuka, T., Sugiyama, N., Mizuno, T., Suzuki, M., & Takagi, S. I. (2001). A novel fabrication technique of ultrathin and relaxed SiGe buffer layers with high Ge fraction

for sub-100 nm strained silicon-on-insulator MOSFETs. *Japanese Journal of Applied Physics*, *40*(4S), 2866.

[105] Tezuka, T., Sugiyama, N., & Takagi, S. (2001). Fabrication of strained Si on an ultrathin SiGe-on-insulator virtual substrate with a high-Ge fraction. *Applied Physics Letters*, *79*(12), 1798-1800.

[106] Bojarczuk, N. A., Copel, M., Guha, S., Narayanan, V., Preisler, E. J., Ross, F. M., & Shang, H. (2003). Epitaxial silicon and germanium on buried insulator heterostructures and devices. *Applied physics letters*, *83*(26), 5443-5445.

[107] Sugiyama, N., Tezuka, T., Mizuno, T., Suzuki, M., Ishikawa, Y., Shibata, N., & Takagi, S. (2004). Temperature effects on Ge condensation by thermal oxidation of SiGe-on-insulator structures. *Journal of Applied Physics*, *95*(8), 4007-4011.

[108] Sugii, N., Nakagawa, K., Yamaguchi, S., & Miyao, M. (1999). Role of $Si_{1-x}Ge_x$ buffer layer on mobility enhancement in a strained-Si n-channel metal–oxide–semiconductor field-effect transistor. *Applied physics letters*, *75*(19), 2948-2950.

[109] Mizuno, T., Takagi, S., Sugiyama, N., Satake, H., Kurobe, A., & Toriumi, A. (2000). Electron and hole mobility enhancement in strained-Si MOSFET's on SiGe-on-insulator substrates fabricated by SIMOX technology. *IEEE Electron Device Letters*, *21*(5), 230-232.

[110] Boztug, C., Sánchez-Pérez, J. R., Cavallo, F., Lagally, M. G., & Paiella, R. (2014). Strained-germanium nanostructures for infrared photonics. *ACS nano*, *8*(4), 3136-3151.

[111] Liu, C. S., Teng, Z. W., Ye, X. J., & Yan, X. H. (2017). Two-dimensional tetragonal AlP monolayer: strain-tunable direct–indirect band-gap and semiconductor–metal transitions. *Journal of Materials Chemistry C*, *5*(24), 5999-6004.

[112] Fischetti, M. V., & Laux, S. E. (1996). Band structure, deformation potentials, and carrier mobility in strained Si, Ge, and SiGe alloys. *Journal of Applied Physics*, *80*(4), 2234-2252.

[113] Irisawa, T., Tokumitsu, S., Hattori, T., Nakagawa, K., Koh, S., & Shiraki, Y. (2002). Ultrahigh room-temperature hole Hall and effective mobility in $Si_{0.3}Ge_{0.7}$/Ge/$Si_{0.3}Ge_{0.7}$ heterostructures. *Applied Physics Letters*, *81*(5), 847-849.

[114] Steen, S. (2003). Electrical characterization of germanium p-channel MOSFETs. *IEEE Electron Device Letters*, *24*(4).

[115] N. Rodrigues, L., Scolfaro, D., da Conceicao, L., Malachias, A., Couto Jr, O. D., Iikawa, F., & Deneke, C. (2021). Rolled-Up Quantum Wells Composed of Nanolayered

InGaAs/GaAs Heterostructures as Optical Materials for Quantum Information Technology. *ACS Applied Nano Materials*, *4*(3), 3140-3147.

[116] Wei, S. H., & Zunger, A. (1995). InAsSb/InAs: A type-I or a type-II band alignment. *Physical Review B*, *52*(16), 12039.

[117] Jo, K. W., Kim, W. K., Takenaka, M., & Takagi, S. (2019). Impact of SiGe layer thickness in starting substrates on strained Ge-on-insulator pMOSFETs fabricated by Ge condensation method. *Applied Physics Letters*, *114*(6), 062101.

[118] Schmidt, O. G., & Eberl, K. (2001). Thin solid films roll up into nanotubes. Nature, 410(6825), 168-168.

[119] Songmuang, R., Rastelli, A., Mendach, S., Deneke, C., & Schmidt, O. G. (2007). From rolled-up Si microtubes to SiO_x/Si optical ring resonators. *Microelectronic engineering*, *84*(5-8), 1427-1430.

[120] Xu, C., Wu, X., Huang, G., & Mei, Y. (2019). Rolled-up nanotechnology: materials issue and geometry capability. Advanced materials technologies, 4(1), 1800486.

[121] Cavallo, F., Songmuang, R., & Schmidt, O. G. (2008). Fabrication and electrical characterization of Si-based rolled-up microtubes. *Applied Physics Letters*, *93*(14), 143113.

[122] Magalhaes-Paniago, R., Medeiros-Ribeiro, G., Malachias, A., Kycia, S., Kamins, T. I., & Williams, R. S. (2002). Direct evaluation of composition profile, strain relaxation, and elastic energy of Ge: Si (001) self-assembled islands by anomalous x-ray scattering. *Physical Review B*, *66*(24), 245312.

[123] Kriegner, D., Wintersberger, E., & Stangl, J. (2013). X-rayutilities: a versatile tool for reciprocal space conversion of scattering data recorded with linear and area detectors. *Journal of Applied Crystallography*, *46*(4), 1162-1170.

[124] Parratt, L. G. (1954). Surface studies of solids by total reflection of X-rays. *Physical review*, *95*(2), 359.

[125] Als-Nielsen, J., & McMorrow, D. (2011). *Elements of modern X-ray physics*. John Wiley & Sons.

[126] Balakumar, S., Lo, G. Q., Tung, C. H., Kumar, R., Balasubramanian, N., Kwong, D. L., ... & Li, M. F. (2006). SiGe amorphization during Ge condensation in silicon germanium on insulator. *Applied physics letters*, *89*(4), 042115.

[127] Min, B. G., Pae, Y. H., Jun, K. S., Ko, D. H., Kim, H., Cho, M. H., & Lee, T. W. (2006). Formation of a Ge-rich layer during the oxidation of strained $Si_{1-x}Ge_x$. *Journal of Applied physics*, 100, 016102.

[128] Balakumar, S., Peng, S., Hoe, K. M., Agarwal, A., Lo, G. Q., Kumar, R., ... & Tripathy, S. (2007). SiGeO layer formation mechanism at the SiGe/oxide interfaces during Ge condensation. *Applied physics letters*, *90*(3), 032111.

[129] Malachias, A., Deneke, C., Krause, B., Mocuta, C., Kiravittaya, S., Metzger, T. H., & Schmidt, O. G. (2009). Direct strain and elastic energy evaluation in rolled-up semiconductor tubes by x-ray microdiffraction. *Physical Review B*, *79*(3), 035301.

[130] Songmuang, R., Deneke, C., & Schmidt, O. G. (2006). Rolled-up micro-and nanotubes from single-material thin films. *Applied physics letters*, *89*(22), 223109.

[131] Nikishkov, G. P. (2003). Curvature estimation for multilayer hinged structures with initial strains. *Journal of Applied Physics*, *94*(8), 5333-5336.

[132] Deneke, C., Müller, C., Jin-Phillipp, N. Y., & Schmidt, O. G. (2002). Diameter scalability of rolled-up In(Ga)As/GaAs nanotubes. *Semiconductor science and technology*, *17*(12), 1278.

[133] Schmidt, O. G., Schmarje, N., Deneke, C., Müller, C., & Jin-Phillipp, N. Y. (2001). Three-Dimensional Nano-objects evolving from a Two-Dimensional layer technology. *Advanced Materials*, *13*(10), 756-759.

[134] Nakaharai, S., Tezuka, T., Hirashita, N., Toyoda, E., Moriyama, Y., Sugiyama, N., & Takagi, S. (2009). Formation process of high-purity Ge-on-insulator layers by Ge-condensation technique. *Journal of Applied Physics*, *105*(2), 024515.

[135] Hasan, M. Z., & Kane, C. L. (2010). Colloquium: topological insulators. *Reviews of modern physics*, *82*(4), 3045.

[136] Fu, L. (2011). Topological crystalline insulators. *Physical Review Letters*, *106*(10), 106802.

[137] Zhang, H., Liu, C. X., Qi, X. L., Dai, X., Fang, Z., & Zhang, S. C. (2009). Topological insulators in Bi2Se3, Bi2Te3 and Sb2Te3 with a single Dirac cone on the surface. *Nature physics*, *5*(6), 438-442.Moore, J. E. (2010). The birth of topological insulators. *Nature*, *464*(7286), 194-198.

[138] Linder, J., Yokoyama, T., & Sudbø, A. (2009). Anomalous finite size effects on surface states in the topological insulator Bi_2Se_3. *Physical review B*, *80*(20), 205401.

[139] Moore, J. E. (2010). The birth of topological insulators. *Nature*, *464*(7286), 194-198.

[140] Chen, Y. L., Analytis, J. G., Chu, J. H., Liu, Z. K., Mo, S. K., Qi, X. L., ... & Shen, Z. X. (2009). Experimental realization of a three-dimensional topological insulator, Bi_2Te_3. *science*, *325*(5937), 178-181.

[141] Xia, Y., Qian, D., Hsieh, D., Wray, L., Pal, A., Lin, H., ... & Hasan, M. Z. (2009). Observation of a large-gap topological-insulator class with a single Dirac cone on the surface. *Nature physics*, *5*(6), 398-402.

[142] Fülöp, A., Song, Y., Charpentier, S., Shi, P., Ekström, M., Galletti, L., ... & Wang, S. (2014). Phase transition of bismuth telluride thin films grown by MBE. *Applied Physics Express*, *7*(4), 045503.

[143] Song, C. L., Wang, Y. L., Jiang, Y. P., Zhang, Y., Chang, C. Z., Wang, L., ... & Ma, X. (2010). Topological insulator Bi_2Se_3 thin films grown on double-layer graphene by molecular beam epitaxy. *Applied Physics Letters*, *97*(14), 143118.

[144] Dai, J., West, D., Wang, X., Wang, Y., Kwok, D., Cheong, S. W., ... & Wu, W. (2016). Toward the intrinsic limit of the topological insulator Bi_2Se_3. *Physical review letters*, *117*(10), 106401.

[145] Nakajima, S. (1963). The crystal structure of $Bi_2Te_{3-x}Se_x$. *Journal of Physics and Chemistry of Solids*, *24*(3), 479-485.

[146] Feutelais, Y., Legendre, B., Rodier, N., & Agafonov, V. (1993). A study of the phases in the bismuth-tellurium system. *Materials Research Bulletin*, *28*(6), 591-596.

[147] Anderson, T. L., & Krause, H. B. (1974). Refinement of the Sb_2Te_3 and Sb_2Te_2Se structures and their relationship to nonstoichiometric $Sb_2Te_{3-y}Se_y$ compounds. *Acta Crystallographica Section B: Structural Crystallography and Crystal Chemistry*, *30*(5), 1307-1310.

[148] Teweldebrhan, D., Goyal, V., & Balandin, A. A. (2010). Exfoliation and characterization of bismuth telluride atomic quintuples and quasi-two-dimensional crystals. Nano letters, 10(4), 1209-1218.

[149] Teweldebrhan, D., Goyal, V., Rahman, M., & Balandin, A. A. (2010). Atomically-thin crystalline films and ribbons of bismuth telluride. Applied Physics Letters, 96(5), 053107.

[150] Ambrosi, A., Sofer, Z., Luxa, J., & Pumera, M. (2016). Exfoliation of layered topological insulators Bi2Se3 and Bi2Te3 via electrochemistry. *ACS nano*, *10*(12), 11442-11448.

[151] Hong, S. S., Kundhikanjana, W., Cha, J. J., Lai, K., Kong, D., Meister, S., ... & Cui, Y. (2010). Ultrathin topological insulator Bi2Se3 nanoribbons exfoliated by atomic force microscopy. *Nano letters*, *10*(8), 3118-3122.

[152] Ding, Z., Viculis, L., Nakawatase, J., & Kaner, R. B. (2001). Intercalation and solution processing of bismuth telluride and bismuth selenide. *Advanced Materials*, *13*(11), 797-800.

[153] Ren, L., Qi, X., Liu, Y., Hao, G., Huang, Z., Zou, X., ... & Zhong, J. (2012). Large-scale production of ultrathin topological insulator bismuth telluride nanosheets by a hydrothermal intercalation and exfoliation route. *Journal of Materials Chemistry*, *22*(11), 4921-4926.

[154] Kong, D., Randel, J. C., Peng, H., Cha, J. J., Meister, S., Lai, K., ... & Cui, Y. (2010). Topological insulator nanowires and nanoribbons. *Nano letters*, *10*(1), 329-333.

[155] Peng, H., Lai, K., Kong, D., Meister, S., Chen, Y., Qi, X. L., ... & Cui, Y. (2010). Aharonov–Bohm interference in topological insulator nanoribbons. *Nature materials*, *9*(3), 225-229.

[156] Chen, X., Ma, X. C., He, K., Jia, J. F., & Xue, Q. K. (2011). Molecular beam epitaxial growth of topological insulators. *Advanced Materials*, *23*(9), 1162-1165.

[157] Krumrain, J., Mussler, G., Borisova, S., Stoica, T., Plucinski, L., Schneider, C. M., & Grützmacher, D. (2011). MBE growth optimization of topological insulator Bi_2Te_3 films. *Journal of Crystal Growth*, *324*(1), 115-118.

[158] Liu, H. W., Yuan, H. T., Fukui, N., Zhang, L., Jia, J. F., Iwasa, Y., ... & Xue, Q. K. (2010). Growth of topological insulator Bi_2Te_3 ultrathin films on Si (111) investigated by low-energy electron microscopy. *Crystal growth & design*, *10*(10), 4491-4493.

[159] Liu, X., Smith, D. J., Fan, J., Zhang, Y. H., Cao, H., Chen, Y. P., ... & Furdyna, J. K. (2011). Structural properties of Bi_2Te_3 and Bi_2Se_3 topological insulators grown by molecular beam epitaxy on GaAs (001) substrates. *Applied Physics Letters*, *99*(17), 171903.

[160] Fornari, C. I., Rappl, P. H., Morelhão, S. L., & Abramof, E. (2016). Structural properties of Bi_2Te_3 topological insulator thin films grown by molecular beam epitaxy on (111) BaF2 substrates. *Journal of Applied Physics*, *119*(16), 165303.

[161] Harrison, S. E., Li, S., Huo, Y., Zhou, B., Chen, Y. L., & Harris, J. S. (2013). Two-step growth of high quality Bi_2Te_3 thin films on Al_2O_3 (0001) by molecular beam epitaxy. *Applied Physics Letters*, *102*(17), 171906.

[162] Steiner, H., Volobuev, V., Caha, O., Bauer, G., Springholz, G., & Holý, V. (2014). Structure and composition of bismuth telluride topological insulators grown by molecular beam epitaxy. *Journal of Applied Crystallography*, *47*(6), 1889-1900.

[163] Guo, Y., Liu, Z., & Peng, H. (2015). A roadmap for controlled production of topological insulator nanostructures and thin films. *Small*, *11*(27), 3290-3305.

[164] Ozaki, T., Kino, H., Yu, J., Han, M. J., Kobayashi, N., Ohfuti, M., ... & Terakura, K. (2019). OpenMX: Open-source package for Material eXplorer. *URL: www. openmx-square. org*.

[165] Ozaki, T., & Kino, H. (2004). Numerical atomic basis orbitals from H to Kr. *Physical Review B*, *69*(19), 195113.

[166] Ozaki, T. (2003). Variationally optimized atomic orbitals for large-scale electronic structures. *Physical Review B*, *67*(15), 155108.

[167] Perdew, J. P., Burke, K., & Ernzerhof, M. (1996). Generalized gradient approximation made simple. *Physical review letters*, *77*(18), 3865.

[168] Troullier, N., & Martins, J. L. (1991). Efficient pseudopotentials for plane-wave calculations. *Physical review B*, *43*(3), 1993.

[169] Coelho, P. M., Ribeiro, G. A., Malachias, A., Pimentel, V. L., Silva, W. S., Reis, D. D., ... & Magalhães-Paniago, R. (2013). Temperature-induced coexistence of a conducting bilayer and the bulk-terminated surface of the topological insulator Bi_2Te_3. *Nano letters*, *13*(9), 4517-4521.

[170] Gonçalves, P. H. R., Chagas, T., Nascimento, V. B., Dos Reis, D. D., Parra, C., Mazzoni, M. S. C., ... & Magalhaes-Paniago, R. (2018). Formation of Bi_xSe_y Phases Upon Annealing of the Topological Insulator Bi_2Se_3: Stabilization of In-Depth Bismuth Bilayers. The Journal of Physical Chemistry Letters, 9(5), 954-960.

[171] Yamana, K. A. Z. U. O., Kihara, K. U. N. I. A. K. I., & Matsumoto, T. A. K. E. O. (1979). Bismuth tellurides: BiTe and Bi_4Te_3. *Acta Crystallographica Section B: Structural Crystallography and Crystal Chemistry*, *35*(1), 147-149.

[172] Parra, C., Rodrigues da Cunha, T. H., Contryman, A. W., Kong, D., Montero-Silva, F., Rezende Gonçalves, P. H., ... & Manoharan, H. C. (2017). Phase separation of Dirac electrons in topological insulators at the spatial limit. *Nano Letters*, *17*(1), 97-103.

[173] Dang, W., Peng, H., Li, H., Wang, P., & Liu, Z. (2010). Epitaxial heterostructures of ultrathin topological insulator nanoplate and graphene. *Nano letters*, *10*(8), 2870-2876.

[174] Zhang, J., Peng, Z., Soni, A., Zhao, Y., Xiong, Y., Peng, B., ... & Xiong, Q. (2011). Raman spectroscopy of few-quintuple layer topological insulator Bi_2Se_3 nanoplatelets. *Nano letters*, *11*(6), 2407-2414.

[175] Wang, C., Zhu, X., Nilsson, L., Wen, J., Wang, G., Shan, X., ... & Xue, Q. (2013). In situ Raman spectroscopy of topological insulator Bi_2Te_3 films with varying thickness. *Nano Research*, *6*(9), 688-692.

[176] Zhao, Y., Luo, X., Zhang, J., Wu, J., Bai, X., Wang, M., ... & Xiong, Q. (2014). Interlayer vibrational modes in few-quintuple-layer Bi_2Te_3 and Bi_2Se_3 two-dimensional crystals: Raman spectroscopy and first-principles studies. *Physical Review B*, *90*(24), 245428.

[177] Ferralis, N. (2010). Probing mechanical properties of graphene with Raman spectroscopy. *Journal of materials science*, *45*(19), 5135-5149.

[178] Das, A., Pisana, S., Chakraborty, B., Piscanec, S., Saha, S. K., Waghmare, U. V., ... & Sood, A. K. (2008). Monitoring dopants by Raman scattering in an electrochemically top-gated graphene transistor. *Nature nanotechnology*, *3*(4), 210-215.

[179] Shahil, K. M. F., Hossain, M. Z., Goyal, V., & Balandin, A. A. (2012). Micro-Raman spectroscopy of mechanically exfoliated few-quintuple layers of Bi_2Te_3, Bi_2Se_3, and Sb_2Te_3 materials. *Journal of Applied Physics*, *111*(5), 054305.

[180] He, R., Wang, Z., Qiu, R. L., Delaney, C., Beck, B., Kidd, T. E., ... & Gao, X. P. (2012). Observation of infrared-active modes in Raman scattering from topological insulator nanoplates. *Nanotechnology*, *23*(45), 455703.

[181] Bos, J. W. G., Zandbergen, H. W., Lee, M. H., Ong, N. P., & Cava, R. J. (2007). Structures and thermoelectric properties of the infinitely adaptive series $(Bi_2)_m$ $(Bi_2 Te_3)_n$. *Physical Review B*, *75*(19), 195203.

[182] Concepcion, O., Galvan-Arellano, M., Torres-Costa, V., Climent-Font, A., Bahena, D., Manso Silvan, M., ... & de Melo, O. (2018). Controlling the epitaxial growth of Bi_2Te_3, BiTe, and Bi_4Te_3 pure phases by physical vapor transport. *Inorganic Chemistry*, *57*(16), 10090-10099.

[183] Skrzypek, J. J., & Ganczarski, A. W. (Eds.). (2015). *Mechanics of anisotropic materials* (pp. 57-86). Cham, Switzerland: Springer International Publishing.

[184] Feng, S., Li, S., & Fu, H. (2014). First-principles calculation and quasi-harmonic Debye model prediction for elastic and thermodynamic properties of Bi_2Te_3. *Computational materials science*, *82*, 45-49.

[185] Yazyev, O. V., Moore, J. E., & Louie, S. G. (2010). Spin polarization and transport of surface states in the topological insulators Bi_2Se_3 and Bi_2Te_3 from first principles. *Physical review letters*, *105*(26), 266806.

[186] Li, Y. Y., Wang, G., Zhu, X. G., Liu, M. H., Ye, C., Chen, X., ... & Xue, Q. K. (2010). Intrinsic topological insulator Bi_2Te_3 thin films on Si and their thickness limit. *Advanced materials*, *22*(36), 4002-4007.

[187] Aramberri, H., & Muñoz, M. C. (2017). Strain effects in topological insulators: Topological order and the emergence of switchable topological interface states in Sb_2Te_3/Bi_2Te_3 heterojunctions. *Physical Review B*, *95*(20), 205422.

[188] Fornari, C. I., Rappl, P. H. O., Morelhão, S. L., Peixoto, T. R. F., Bentmann, H., Reinert, F., & Abramof, E. (2016). Preservation of pristine Bi_2Te_3 thin film topological insulator surface after ex situ mechanical removal of Te capping layer. *APL Materials*, 4(10), 106107.

[189] Ousaka, Y., Sakai, O., & Tachiki, M. (1977). Theory of Raman scattering in magnetically ordered phases of EuSe and EuTe. *Solid State Communications*, 23(8), 589-592.

[190] Güntherodt, G., & Zeyher, R. (1984). Spin-dependent Raman scattering in magnetic semiconductors. *Light Scattering in Solids IV*, 203-242.

[191] Li, C. Y., Ruoff, A. L., & Spencer, C. W. (1961). Effect of pressure on the energy gap of Bi_2Te_3. *Journal of Applied Physics*, 32(9), 1733-1735.

[192] Michiardi, M., Aguilera, I., Bianchi, M., de Carvalho, V. E., Ladeira, L. O., Teixeira, N. G., ... & Hofmann, P. (2014). Bulk band structure of Bi_2Te_3. *Physical Review B*, 90(7), 075105.

[193] Thomas, G. A., Rapkine, D. H., Van Dover, R. B., Mattheiss, L. F., Sunder, W. A., Schneemeyer, L. F., & Waszczak, J. V. (1992). Large electronic-density increase on cooling a layered metal: Doped Bi_2Te_3. *Physical Review B*, 46(3), 1553.

[194] Mauger, A., & Godart, C. (1986). The magnetic, optical, and transport properties of representatives of a class of magnetic semiconductors: The europium chalcogenides. *Physics Reports*, 141(2-3), 51-176.